DETERMINATION OF THE B^0 AND B_S^0 MIXING MATRIX ELEMENTS IN 2+1 LATTICE QCD

BY

RICHARD EVANS

B.A., Johns Hopkins University, 2002
M.S., University of Illinois at Urbana-Champaign, 2004

DISSERTATION

Submitted in partial fulfillment of the requirements
for the degree of Doctor of Philosophy in Physics
in the Graduate College of the
University of Illinois at Urbana-Champaign, 2008

Urbana, Illinois

Doctoral Committee:

Professor John Stack, Chair
Professor Aida X. El-Khadra
Professor Philip Phillips
Professor Kevin Pitts

Abstract

The determinations of many fundamental parameters of the Standard Model are hindered by the non-perturbative nature of QCD at low energies. The only known way to calculate quantities governed by QCD at these energies is the use of lattice field theory techniques. In particular, extremely precise measurements of ΔM_d, and recently of ΔM_s, exist. By combining these measurements with a comparably precise calculation of the hadronic matrix elements contributing to ΔM_d and ΔM_s, the Unitarity Triangle would be much more tightly constrained, giving insights into new physics. Current lattice calculations of these matrix elements suffer from uncontrolled uncertainties.

This report presents a calculation and results for the matrix elements relevant for the analysis of $B^0 - \bar{B}^0$ mixing using the Asqtad (light-quark) and Fermilab (heavy-quark) actions. The calculation is performed on the 2+1 MILC ensembles at three different lattice spacings, and uses staggered chiral perturbation theory to perform the extrapolations to the physical light quark masses as well as to the continuum. All known systematic errors are explored and estimated resulting in a value and uncertainty for ξ that can be used directly as input for Unitarity constraints.

To Richard and Janet Evans

Acknowledgements

I'd like to thank all members of the Fermilab Lattice and MILC collaborations for their invaluable advice and help with many parts of this calculation. It would not have been possible without them. I'd especially like to thank Aida El-Khadra for her constant guidance and support.

The numerical simulations for this work were carried out on the Fermilab lattice QCD clusters, which are a computing resource of the USQCD collaboration and are funded by the DOE. We are grateful to the Fermilab Computing Divisions for operating and maintaining the clusters.

Table of Contents

List of Tables . . . . . **vii**

List of Figures . . . . . **ix**

Chapter 1 Overview of the Standard Model and $B^0 - \bar{B}^0$ Mixing **1**
1.1 Overview of the Electroweak Sector: Glashow-Weinberg-Salam (GSW) Model 2
1.2 Flavour Physics, Lattice QCD, and the Search for New Physics . 6
1.3 $B_q^0 - \bar{B}_q^0$ System 8

Chapter 2 Lattice QCD **13**
2.1 Numerical Evaluation of the Path Integral 14
2.2 From the Continuum to the Lattice 16
2.2.1 Transcription of QCD Fields to the Lattice 17
2.2.2 Gauge Action 18
2.2.3 Naive and Wilson Fermion Actions 18
2.2.4 Staggered Fermion Action 20
2.3 Symanzik Improvement 21
2.3.1 Improvement of the Wilson Gauge Action: MILC Gauge Action 22
2.3.2 Improvement of the Wilson Action: Clover Action→Fermilab Interpretation 23
2.3.3 Improvement of the Staggered Action: a Squared Tadpole Improved (Asqtad) Action 26
2.4 Correlation Functions and Parameter Extraction 27
2.5 Heavy-Light Four-quark Operators: B Mixing 28
2.5.1 Doubler Modes' Effect on the Form of the Correlation Functions 29
2.5.2 The Wick Contractions→Open Propagators and Correlation Functions 31
2.5.3 Improving the Heavy-Light Four-Quark Operator 34
2.5.4 Naive Spinors 35
2.6 Code Development 35

Chapter 3 Correlator Fitting **37**
3.1 Fitting Method 38
3.2 Fits 41
3.2.1 Direct Fit Details 43
3.2.2 Correlator Fit Results and Example Plots 45
3.2.3 ISA Fits: Procedure 56
3.2.4 ISA Fits: Results 57

Chapter 4 Perturbative Matching 65
4.1 Determination of the Optimal Coupling: α_V 66
4.2 Operator Mixing and the Matching Relation 67
4.3 Calculation Procedure 68
4.4 Matching Coefficients 70

Chapter 5 Chiral Perturbation Theory 72
5.1 Continuum Chiral Perturbation Theory 73
5.1.1 Partially-Quenched Chiral Perturbation Theory 75
5.1.2 Heavy-Light Meson Chiral Perturbation Theory ($HM\chi PT$) 76
5.2 Rooted Staggered χral Perturbation Theory ($rS\chi PT$) 76
5.3 The Chiral Expression for $\langle \bar{B}_q^0 | Q_q^1 | B_q^0 \rangle$ 78

Chapter 6 Chiral Fits 81
6.1 Parametrization of the Chiral Expression 81
6.2 Chiral Fitting Procedure, Priors and Inputs 83
6.3 Chiral Fits and Extrapolations 86
6.3.1 Medium Coarse Data: Too Coarse? 86
6.3.2 Fits and Extrapolations: Choosing an Anszatz 87
6.4 Fiducial Point Method 97

Chapter 7 Systematic Error Analysis 98
7.1 Inputs into the Analysis 98
7.2 Higher Order Effects in the Perturbative Matching 99
7.3 Discretization Errors 100
7.4 Finite Volume Corrections 100
7.5 Final Error Budget 101

Chapter 8 Summary of Results and Outlook 103
8.1 Summary of Results 103
8.2 Outlook 104

Appendix A 105
A.1 Code 105
A.1.1 Correlator Construction Code 105
A.1.2 Correlator Fit Code 113

Appendix B 120
B.1 Chiral Expressions for $\langle \bar{B}_q | Q_q^1 | B_q \rangle$ and B_{B_q} 120

References 122

Author's Biography 125

List of Tables

3.1 Ensembles on which two and three-point functions were calculated. Three different lattice spacings were used, with 6 different light valence quark masses, m_q, on each ensemble. The sea quark masses are labeled as m_L for the 2 degenerate light sea quarks and m_h for strange sea quark. All correlators were calculated at four different time sources and averaged over them. 42

3.2 The priors with index 0 refer to the ground state. Higher energy state priors have indices i and j. The superscript p indicates the first opposite parity excited state. These priors are used for the β_q fits. O_{00} is set to 0.3 for the B_{B_q} fits. These priors are used for the two-point correlator fits in the ISA as well. The ISA is a plateau fit, and the prior value is unconstrained. 43

3.3 Number of states and time slices used for each correlator in the direct fits. 44

3.4 Correlator fit results for $f_{B_q}\sqrt{M_{B_q}B_{B_q}}$. 48

3.5 Correlator fit results for $f_{B_q}\sqrt{M_{B_q}B^S_{B_q}}$. 49

3.6 Correlator fit results for B_{B_q}. 50

3.7 ISA fit results for B_{B_q}. 58

4.1 The matching coefficients for Q^1. $IR = \frac{1}{4\pi}\log(\lambda^2)$, where λ is the gluon mass used as an infrared regulator [16]. 71

6.1 Ensembles on which two and three-point functions were calculated. Three different lattice spacings were used, with 6 different light valence quark masses on each. 83

6.2 Fit parameters' priors and input parameters. The parameters were determined in Refs. [5] and priors and prior widths by discussions with [39]. f_π is determined from experimental values. $s = \frac{1}{8\pi^2(f_\pi r_1)^2} = 0.285$ 85

6.3 Direct fit results, coarse and fine ensembles only. Errors in parentheses are 68% bootstrap confidence intervals. The fit Ansatz in red, where all NNLO terms have been include, is used as the central value fit. The NLO and $NLO + Q_3$ Ansatz give the most extreme values for the mixing parameters and are used to determined the chiral fit systematics. 89

6.4 Direct fit results, coarse and fine ensembles only for the bag parameters. 89

7.1 Latest determination of the "physical" light-quark masses used in the chiral extrapolations. These values were determined by the MILC collaboration [39]. The error in the first parentheses indicates statistical error, the second chiral extrapolation systematics, the third scale uncertainty. 99
7.2 The total systematic error budget for the B mixing matrix element calculation. The uncertainty due to κ_b is negligible in our preliminary estimates, and the uncertainty found in the Fermilab Lattice MILC collaborations' calculation of f_B and f_{B_s} is used as a conservative estimate. 102

8.1 Results for the B mixing parameters without matching coefficients. The results for the bag parameters are preliminary, all systematic errors have not been included. 103
8.2 The determination of $|V_{td}/V_{ts}|$ using this report's calculation of ξ. 103

List of Figures

1.1 $\pi^+(q) \to \bar{\nu}(p)\nu_\mu(k)$ 7
1.2 The two diagrams contributing to $B^0 - \bar{B}^0$ mixing. 8
1.3 The CKM Unitarity Triangle. 10

2.1 The set-up of the four-quark operator calculation is shown above. The operator Q is fixed at the origin, and the $\bar{B}$ and B interpolating fields varied over x and y. 29

3.1 An example fit in 2 dimensions. The red crosses are the data points and the blue points and lines are the fit. Statistical errors are not shown because of the 2 dimensional nature of the plot, but grow rapidly in time. 45
3.2 $f_B\sqrt{m_B B_B}$ for a variety of states. Fits are stable by $N_{states} = 4$. 46
3.3 B_B for a variety of states. Heavier valence mass data is stable by $N_{states} = 4$. The light valence mass data's central value is stable at $N_{states} = 4$, but the errors increase and stabilize at $N_{states} = 6$. 46
3.4 B_B for a variety of states. Same case as coarse B_B data. 47
3.5 $f_B\sqrt{m_B B_B}$: Example fit. All fits are 2 dimensional. The different t_1 timeslices are overlayed. 51
3.6 $f_B\sqrt{m_B B_B}$: Example fit. 51
3.7 $f_B\sqrt{m_B B_B}$: Example fit. 52
3.8 $f_B\sqrt{m_B B_B}$: Example fit. 52
3.9 $f_B\sqrt{m_B B_B}$: Example fit. 53
3.10 $\beta_q = f_{B_q}\sqrt{m_{B_q} B_{B_q}}$. Fit results are shown. The sea mass dependence is weak. r_1 is a scale dependent quantity used to convert data in lattice units to a common physical scale. It's precise definition and the definition of $m_{qq}^2 \sim m_q$ will be explained in Chapter 6. 54
3.11 $\beta_q^S = f_{B_q}^S\sqrt{m_{B_q} B_{B_q}^S}$. Fit results are shown. The light mass dependence of the data is nearly identical to that of β_q. 54
3.12 Fit results are shown for B_{B_q}. The sea mass dependence is weak in the data with small statistical errors. Some of the data is extremely noisy. 55
3.13 MA's effect: B_B. The oscillations along t_2 are significantly reduced. Green and blue data are the offset scaled correlators, $R(T)$ and $R(T+1)$, for timeslices $t_1 = 2, 3$, from which the MA's are constructed. Lines are for visualization only, NOT fits to the data. 59
3.14 SA's effect: B_B. The oscillations along t_1 are now also reduced. . 60
3.15 ISA_0's effect: B_B 60

3.16 ISA_1's effect: B_B. Oscillations are no longer discernible and a plateau is produced. 61
3.17 ISA procedure's effect on noiser data, in this case a lighter mass valence quark: B_B. The data by ISA_1 is too noisy to obtain a reliable plateau. 62
3.18 Plateau fit to ISA_1 data. The fit looks good for less noisy data. The upper and lower dashed lines are the error bars on the fit, and the central line is the fit. 63
3.19 Plateau fit to ISA_1 data. 64

4.1 The two possible Dirac structures of the matching diagrams for Q^1, where $S1 = (\bar{u}_Q \Gamma u_q)(\bar{v}_Q \Gamma v_q)$ and $S2 = (\bar{u}_Q \Gamma v_q)(\bar{v}_Q \Gamma u_q)$ . . . 68
4.2 The diagrams, without rotations, contributing to the Q^1 matching calculation. 69
4.3 Additional diagrams due to rotations. Diagrams $c - f'$ with a rotation are not shown. The diagrams, $a_1 - f_1'$ are calculated in the same way as $a - f'$ but with a derivative acting on the heavy quark/anti-quark propagator, indicated by the black dot. Diagrams $g_1 - g_4'$ have a gluon vertex attached to the heavy quark rotation, and the same diagrams exist with the gluon vertex attached to the heavy anti-quark rotation. 70

5.1 Diagrams contributing to the one-loop B mixing chiral expression. Dashed lines are pion propagators, solid lines B meson fields, and double lines B^* meson propagators. The operator is represented as a $\otimes$. (a) is the wave-function renormalization $\mathcal{W}$, (b) the tadpole contribution $\mathcal{T}$, and (c) the sunset diagram $\mathcal{Q}$ [12]. 78

6.1 . Fit to all ensembles and extrapolation using all NNLO analytic terms. The plots is presented in the sea mass plane, where data is plotted versus the pseudo-scalar pion mass composed of the light sea quarks, $m_\pi = \mu(m_L + m_L)$. The 3 different line and point colors correspond to the 3 lattice spacings used in the fit. The circles are full QCD points, where $m_q = m_L$, and the solid lines through them of the same color are the fit lines. An extrapolation in of the solid lines give β_d. The $\times$s are the data where $m_q = m_s$ at the same points as the full QCD points, where m_s is an ensembles s quark mass, and the dashed lines through them are the fits. An extrapolation in the dashed lines gives β_s. 88
6.2 NLO fit plotted in sea quark mass plane. The fit lines follow the data well. The data points in the upper right corner are for reference only and are not being fit to. 90
6.3 NLO fit, plotted in valence pion mass plane, defined the same as the sea pion mass in Fig. 6.1 but with $m_L \to m_q$. All mass points are shown. 90
6.4 NLO fit plotted in sea quark mass plane. The fit lines follow the data well. 91
6.5 NLO fit, plotted in valence mass plane. All mass points shown. . 91
6.6 $NNLO$ fit plotted in sea quark mass plane. The fit lines follow the data well. 92
6.7 $NNLO$ fit, plotted in valence mass plane. All mass points shown. 92
6.8 $NNLO$ fit plotted in sea quark mass plane. The fit lines follow the data well. 93
6.9 $NNLO$ fit, plotted in valence mass plane. All mass points shown. 93

6.10 $NLO+Q_3$ fit plotted in sea quark mass plane. The fit lines follow the data well. 94
6.11 $NLO + Q_3$ fit, plotted in valence mass plane. All mass points shown. 94
6.12 $NLO+Q_3$ fit plotted in sea quark mass plane. The fit lines follow the data well. 95
6.13 $NLO + Q_3$ fit, plotted in valence mass plane. All mass points shown. 95
6.14 $NNLO$ fit to B_{B_q}. 96

Chapter 1

Overview of the Standard Model and $B^0 - \bar{B}^0$ Mixing

The interactions of elementary particles are understood through a generally successful theory known as the Standard Model (SM). The SM is extremely well tested in certain sectors, but has conceptual problems related to the Higgs mechanism, the spontaneous symmetry-breaking process by which particles in the SM acquire mass, and blatant discrepancies with what is seen in nature, as in the case of neutrino oscillations and the overall matter-antimatter asymmetry in the universe. There is an ever expanding set of extensions to the SM which attempt to resolve these issues, but comparisons between precise experimental measurements and SM based theoretical predictions are required as input to distinguish which extensions are in fact a more accurate description of nature.

Flavour physics, the study of flavour changing processes, is an excellent and heavily pursued arena to explore what extensions to the SM are viable. These processes are dependent on the couplings between quarks of different flavours and the weak bosons which appear in the weak sector of the SM, and the parametrization of the couplings is directly derived from the Higgs mechanism. These couplings appear as a unitary matrix known as the Cabibo-Kobayashi-Maskawa (CKM) matrix, and the allowed presence of a complex parameter in it can give rise to combined charge-conjugation parity (CP) violating effects. If the couplings break the unitarity conditions, or the size of the CP violations differ between theoretical predictions and experiment, then some unknown process is contributing. Because any such violations have their origin in the Higgs mechanism they can be directly sensitive to new physics coming from this poorly tested sector.

Precise measurements of flavour changing processes exist with no correspondingly precise theoretical prediction. This is often due to the difficulty in dealing with hadronic matrix elements: the electroweak effects of an interaction can usually be dealt with in a straightforward and perturbative way, whereas the strong force, QCD, which governs the hadronic matrix elements, is non-perturbative at the energy scales of the measurements. The degrees of freedom in measurements are the hadrons, colorless combinations of quarks and gluons, while the degrees of freedom in the SM are the quarks and gluons.

B mixing is a flavour changing process where a neutral B or B_s meson fluctuates into its anti-particle. The SM predicts small amounts of CP violation in

this process, with a SM expression that is directly dependent on poorly known flavour changing couplings contained in the CKM matrix. The mixing occurs at one-loop in the weak interaction, which causes its SM contribution to be suppressed. As a result of this suppression contributions from new physics, such as heavy particles within the loop, are easier to detect. Recent precise measurements of the systems' mass eigenstates' mass difference, ΔM_s and existing measurements of ΔM_d, both with uncertainties of less than 1% [11][43], could be compared with theoretical predictions to test whether the CKM matrix is unitary. Theoretical calculations of this process suffer from hadronic matrix element uncertainties that must be dealt with non-perturbatively. This report presents a calculation of the $\bar{B}^0_q - B^0_q$, $q = d, s$, mixing matrix elements using Lattice QCD methods, where it is attempted to rigorously quantify all systematic errors.

The following Chapter attempts to motivate the necessity for the calculation, summarizing background material relevant to this calculation. In Section 1.1 we will describe the electroweak sector of the SM, how the flavour changing processes and CP violation appear, and why precise calculations of many physical quantities require a non-perturbative approach to QCD. In Section 1.3 we will review the B^0_q mixing system and how this system can be used to test the unitarity of the CKM matrix and detect CP violations.

1.1 Overview of the Electroweak Sector: Glashow-Weinberg-Salam (GSW) Model

The Standard Model is a $\mathrm{SU(3)}\times\mathrm{SU(2)}_L\times\mathrm{U(1)}$ gauge theory, where all particle interactions are governed by the gauge group symmetries. Because we know the weak bosons are massive we know the $SU(2)_L$ gauge symmetry is spontaneously broken. The simplest way to cause the symmetry breaking, and what is assumed by the SM, is the single particle Higgs mechanism. It simultaneously gives rise to the weak boson and fermion masses.

The particles start out massless in order to preserve the $SU(2)_L$ symmetry, which is clearly in contradiction to experimental information. As described in the following, within the SM this symmetry is assumed to be spontaneously broken by the Higgs mechanism.

The SU(3) gauge symmetry gives rise to interactions between quarks and gluons through their color charges. This sector, the QCD or strong sector, will be presented in more detail in Chapter 2 and is left out in the electroweak description for notational convenience. At this point it is sufficient to appreciate that perturbative techniques tend to fail in QCD dependent quantities at low energies.

The GSW model describes the electroweak sector. GSW is an $\mathrm{SU(2)}_L\times\mathrm{U(1)}$ gauge theory, where chiral fermions, $\mathrm{SU(2)}_L$ gauge bosons, and a U(1) gauge

bosons are the degrees of freedom. There are three generations of fermions, where the left handed fermions appear as SU(2) doublets

$$L_L = \begin{pmatrix} \nu_e \\ e \end{pmatrix}_L, \begin{pmatrix} \nu_\mu \\ \mu \end{pmatrix}_L, \begin{pmatrix} \nu_\tau \\ \tau \end{pmatrix}_L \text{ (leptons)}, \tag{1.1}$$
$$Q_L = \begin{pmatrix} u \\ d \end{pmatrix}_L, \begin{pmatrix} c \\ s \end{pmatrix}_L, \begin{pmatrix} t \\ b \end{pmatrix}_L \text{ (quarks)}$$

and the right handed fermions appear as SU(2) singlets

$$e_R,\, u_R,\, d_R. \tag{1.2}$$

The different generations are identical with respect to the gauge interactions.

Each fermion has a weak isospin T_w, where $T_w = 0$ for right handed fermions and $T_w = 1/2$ for left handed fermions. The SU(2) doublets also have $T_{w3} = 1/2$ for the upper components, or u-like fermions, and $T_{w3} = -1/2$ for the lower components, or d-like fermions. The weak hypercharges, Y, must obey certain conditions so as to ensure the cancelation of chiral anomalies that appear in the theory that would otherwise break gauge invariance. The electric charges, Q, of particles in the theory are linearly related to the weak isospin and hypercharge

$$Q = T_{w3} + \frac{1}{2}Y. \tag{1.3}$$

Once the weak isospin charges are assigned and the anomaly cancelation conditions are met a hypercharge is assigned to each particle so as to obtain the observed electric charge.

The fermionic sector of the GSW lagrangian can be written as

$$L_F = \sum_{\psi_L} \bar{\psi}_L i \not{D}_L \psi_L + \sum_{\psi_R} \bar{\psi}_R i \not{D}_R \psi_R \tag{1.4}$$

where the covariant derivatives are

$$D_{\mu,R} = \partial_\mu + i\frac{g_1}{2} Y B_\mu \tag{1.5}$$
$$D_{\mu,L} = \partial_\mu + i\frac{g_1}{2} Y B_\mu + i g_2 \frac{\tau}{2} \cdot W_\mu$$

and ψ_L, ψ_R are either the quark or lepton doublets or singlets. The B_μ gauge boson couples to the $U(1)$ hypercharge with the coupling $g_1 Y$, and the W^a_μ, $(a = 1, 2, 3)$ couple to the $SU(2)_L$ weak isospin charges with the coupling g_2. The gauge fields have their own kinetic terms as well

$$L_G = -\frac{1}{4} F_i^{\mu\nu} F^i_{\mu\nu} - \frac{1}{4} B^{\mu\nu} B_{\mu\nu}. \tag{1.6}$$

While the GSW theory is complete at this point, it is not phenomenologically

relevant because its particles are massless. From experiment it is known the physical degrees of freedom are massive fermions, two charged massive weak bosons, a neutral massive weak boson, and a massless photon. The masses and physical particles must somehow be derived from this theory.

The mechanism the GSW theory uses involves the introduction of an as yet experimentally undetected scalar field. Massive terms necessarily involve the coupling of left and right handed particles. A term containing just these two fields would however break the $SU(2)_L$ symmetry and cannot be directly introduced. Lorentz invariance of the theory could be maintained if terms coupling the right and left handed fermions with a scalar field were introduced, and the $SU(2)_L \times U(1)$ symmetries could be maintained if the scalar field was an $SU(2)_L$ doublet. The scalar field used is referred to as the Higgs field

$$\Phi = \begin{pmatrix} \phi^+ \\ \phi^0 \end{pmatrix} \tag{1.7}$$

where the + and 0 refer to the electric charge of the field component.

The Higgs-fermion coupling sector takes the form

$$L_{HG} = -f_u^{\alpha\beta} \bar{Q}_{L,\alpha} i\tau_2 \Phi^* u_{R,\beta} - f_d^{\alpha\beta} \bar{Q}_{L,\alpha} \Phi d_{R,\beta} - f_e^{\alpha\beta} \bar{L}_{L,\alpha} \Phi e_{R,\beta} + h.c. \tag{1.8}$$

where the charge conjugate of Φ is used in the u quark type sector, and $\alpha, \beta = 1-3$ run over the fermion generations. In general there is no symmetry preventing quarks of different generations from sharing a coupling. The Higgs field is believed to acquire a non-zero vacuum expectation value through some as yet unknown process referred to as spontaneous symmetry-breaking. After the spontaneous symmetry breaking of the Higgs field the fermion masses will take on the form

$$m_{u,d,e} = \frac{v}{\sqrt{2}} f_{u,d,e} \tag{1.9}$$

where $f_{u,d,e}$ is not diagonal. The mass basis can be derived from Eq. (1.8) by a unitary transformation of the quark fields

$$\begin{aligned} L_{HG} &= \bar{u}_L m_u u_R + \bar{d}_L m_d d_R + \bar{e}_L m_e e_R + h.c. \\ &= \bar{u}_L S_L^{u\dagger} S_L^u m_u S_R^{u\dagger} S_R^u u_R + \bar{d}_L S_L^{d\dagger} S_L^d m_d S_R^{d\dagger} S_R^d d_R + \bar{e}_L S_L^{e\dagger} S_L^e m_e S_R^{e\dagger} S_R^e e_R + h.c. \\ &= \bar{u}'_L m'_u u'_R + \bar{d}'_L m'_d d'_R + \bar{e}'_L m'_e e'_R + h.c. \\ &= \bar{u}' m'_u u' + \bar{d}' m'_d d' + \bar{e}' m'_e e' \end{aligned} \tag{1.10}$$

where the S matrices are chosen so as to diagonalize the mass matrices, converting the gauge basis fields to the mass basis (primed fields). The mass basis fields are thus a linear combination of the gauge basis fields, and this linear combination is what is seen in experimental measurements. To perform a calculation the fields in the rest of the lagrangian must be rotated in the same manner. This

has no effect on the electromagnetic and neutral Z^0 interaction terms in the theory: these terms only have quarks of the same u or d type and the transformation matrices employed will simply form the unit matrix. The charged weak currents involving leptons are also unchanged due to the additional freedom of basis resulting from no neutrino mass terms.

The charged weak currents have interactions between quarks of different weak isospin, and thus terms transform as (with the gauge boson in the mass basis)

$$-\frac{g_2}{\sqrt{8}}W_\mu^+ \bar{u}_{L\alpha}\gamma_\mu(1+\gamma_5)d_{L\alpha} \rightarrow -\frac{g_2}{\sqrt{8}}W_\mu^+ S_L^{u\dagger} S_L^d \bar{u}'\gamma_\mu(1+\gamma_5)d' \tag{1.11}$$

where the 3x3 unitary matrix $V \equiv S_L^{u\dagger} S_L^d$, is known as the Cabibbo-Kobayashi-Maskawa (CKM) mixing matrix. The CKM matrix contains the couplings between quarks in the mass basis of different flavor and weak isospin type. The strength of these couplings is not predicted in any way by the theory, although a definite hierarchical structure, with the elements decreasing as they are farther away from the diagonal, has been determined [43],

$$|V_{CKM}| = \left| \begin{pmatrix} V_{ud} & V_{us} & V_{ub} \\ V_{cd} & V_{cs} & V_{cb} \\ V_{td} & V_{ts} & V_{tb} \end{pmatrix} \right| = \tag{1.12}$$

$$\begin{pmatrix} 0.97383^{+0.00024}_{-0.00023} & 0.2272^{+0.0010}_{-0.0010} & (3.96^{+0.09}_{-0.09}) \times 10^{-3} \\ 0.2271^{+0.0010}_{-0.0010} & 0.97296^{+0.00024}_{-0.00024} & (42.21^{+0.10}_{-0.80}) \times 10^{-3} \\ (8.14^{+0.32}_{-0.64}) \times 10^{-3} & (41.61^{+0.12}_{-0.78}) \times 10^{-3} & 0.999100^{+0.000034}_{-0.000004} \end{pmatrix}.$$

A variety of experimental measurements, theoretical inputs, and the unitarity of V_{CKM} were used in the above determination of the CKM matrix elements.

V_{CKM} is a unitary matrix and for n generations has $n(n-1)/2$ real parameters and $n(n+1)/2$ complex parameters. However after taking into account the rephasing invariance of the quark fields $2n-1$ phases can be removed. For three generations 3 real parameters and one complex parameter are left.

A parametrization which makes the unitarity restrictions explicit is the Kobayashi-Maskawa representation

$$V_{CKM} = \begin{pmatrix} c_1 & -s_1c_3 & -s_1s_3 \\ s_1c_2 & c_1c_2c_3 - s_2s_3e^{i\delta} & c_1c_2s_3 + s_2c_3e^{i\delta} \\ s_1s_2 & c_1s_2c_3 + c_2s_3e^{i\delta} & c_1s_2s_3 - c_2c_3e^{i\delta} \end{pmatrix} \tag{1.13}$$

where $s_\alpha \equiv \sin\theta_\alpha$, $c_\alpha \equiv \cos\theta_\alpha$, $(\alpha = 1,2,3)$. The Wolfenstein parametrization makes the hierarchical structure more explicit

$$V_{CKM} = \begin{pmatrix} 1-\lambda^2/2 & \lambda & \lambda^3 A(\rho - i\eta(1-\lambda^2/2)) \\ -\lambda & 1-\lambda^2/2 - i\eta A^2\lambda^4 & \lambda^2 A(1+i\eta\lambda^2) \\ \lambda^3 A(1-\rho-i\eta) & -\lambda^2 A & 1 \end{pmatrix} \tag{1.14}$$

In this parametrization the matrix elements of V_{CKM} are expanded in powers of $\lambda \equiv |V_{us}| \approx 0.22$. In Eq. (1.14) terms up to $\mathcal{O}(\lambda^3)$ have been kept.

1.2 Flavour Physics, Lattice QCD, and the Search for New Physics

There are two main characteristics of the CKM matrix that could provide insights into and constraints for new physics. In the SM QCD and QED conserve charge-conjugation (C), parity reversal (P), and time reversal (T) separately. The charged electroweak interactions break C and P separately, and only if there is a non-zero complex parameter in V_{CKM} is CP invariance violated. CP violation has been observed and so is known to exist in nature: for example in neutral kaon mixing. There are restrictions on the size of the CP asymmetry implied by the SM and experiment, and if the asymmetry is larger than expected in a process there is some new and unknown interaction contributing to that process. The other characteristic of the CKM matrix relevant for new physics is its unitarity. Any violations of the unitarity conditions cannot be described within the context of the SM and indicate new physics.

To the current precision at which the CKM matrix elements are known the unitarity restrictions are not violated. A major effort of flavour physics is to test these restrictions by reducing the uncertainty in the CKM matrix elements by making more precise measurements and theoretical calculations. The only way to determine many of the CKM matrix elements is through a combination of experimental and theoretical input, both of which have an uncertainty associated with them. Most theoretical expressions for flavour changing, or weak, processes can be factored into a product of CKM matrix elements, perturbative coefficients due to electroweak interactions, and a hadronic matrix element due to the strong interaction, QCD. Often, as in the case of $|V_{ub}|$, $|V_{cb}|$, $|V_{td}|$, and $|V_{ts}|$, the theoretical uncertainty is dominated by the QCD governed hadronic matrix elements.

The large uncertainty in the hadronic matrix elements comes from the fact that QCD is non-perturbative at the energies at which the measurements can be made. As a consequence of its non-abelian nature the strong coupling at these energies is large. Because of this the usual perturbative methods of quantum field theories are not applicable and a non-perturbative method must be used to evaluate the hadronic matrix elements. The only current method that leads to systematically reducible errors is to place QCD on a discrete space-time lattice: this method is known as Lattice QCD.

Example Electroweak Process: π^+ Meson Decay

As a typical example of how a weak process factors into perturbative and non-perturbative pieces that can be confronted with experiment consider the π^+

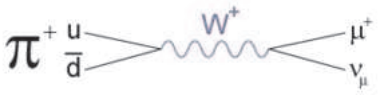

Figure 1.1: $\pi^+(q) \to \bar{\nu}(p)\nu_\mu(k)$

leptonic decay rate shown in Fig. 1.1, $\pi^+(q) \to \bar{\mu}(p)\nu_\mu(k)$. The tree-level invariant amplitude is

$$\begin{aligned}
&\mathcal{M}_{\pi^+\to\mu^+\nu_\mu} \qquad (1.15)\\
&= V_{ud}\frac{g_2^2}{8}\langle 0|\bar{d}\gamma_\mu(1+\gamma_5)u|\pi^+(q)\rangle\frac{(-g^{\mu\nu}+q^\mu q^\nu/M_W^2)}{q^2-M_W^2}\bar{u}_{\nu_\mu}(k)\gamma_\nu(1+\gamma_5)v_\mu(p)\\
&\approx \frac{V_{ud}G_F}{\sqrt{2}}\langle 0|\bar{d}\gamma_\mu(1+\gamma_5)u|\pi^+(q)\rangle\bar{u}_{\nu_\mu}(k)\gamma^\mu(1+\gamma_5)v_\mu(p)
\end{aligned}$$

where the approximation $1 \gg q^2/m_W^2$ has been used and u_{ν_μ} and v_μ correspond to dirac spinors with masses of their respective lepton labels. The u and $\bar{d}$ quarks are bound into a colorless π^+ meson by QCD and can in no way be thought of as free particles. There is no known way to analytically evaluate the bound state. The hadronic matrix element is parametrized as shown in Eq. (1.16) by the momentum factor, q_μ, and the pion decay constant, f_π,

$$\langle 0|\bar{d}\gamma_\mu(1+\gamma_5)u|\pi^+(q)\rangle = q_\mu f_\pi. \qquad (1.16)$$

The invariant matrix element can be used to derive a measurable decay rate

$$\Gamma = \frac{|V_{ud}|^2 G_F^2}{8\pi} f_\pi^2 m_\pi m_\mu^2 (1 - m_\mu^2/m_\pi^2). \qquad (1.17)$$

The weak and electromagnetic contributions can be calculated by perturbative means and determined to arbitrary accuracy. V_{ud} is an unknown input into the theory. Eq. (1.17) can be used together with an experimental measurement of the decay rate to determine $|V_{ud}|$. The uncertainty in $|V_{ud}|$ then depends only on the precision with which the decay rate is measured and f_π calculated. There are many other flavour changing related quantites which have the same form and problem, namely the non-perturbative nature of the hadronic matrix element.

The process which this report addresses is mixing in the neutral B_q^0 meson system. B_q^0 mixing is sensitive to $|V_{td}|$ and $|V_{ts}|$. These CKM matrix elements are poorly known and vital inputs into the testing of the CKM matrix's unitarity.

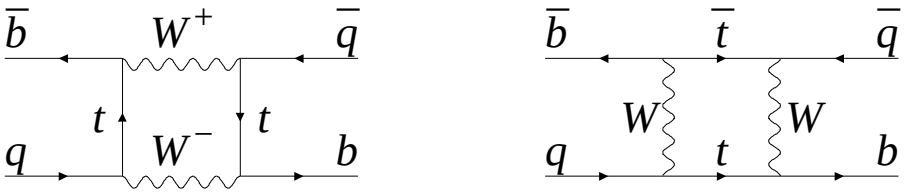

Figure 1.2: The two diagrams contributing to $B^0 - \bar{B}^0$ mixing.

1.3 $B_q^0 - \bar{B}_q^0$ System

The following description applies to the B_q^0 ($q = d, s$) neutral meson system, where by convention the B_q^0 meson contains a $\bar{b}$ anti-quark and the $\bar{B}_q^0$ a b quark. The two-particle system is described by the Schroedinger like equation (derived via the Wigner-Weisskopff approximation) [2]

$$i\frac{d}{dt}\begin{pmatrix} |B(t)\rangle \\ |\bar{B}(t)\rangle \end{pmatrix} = \left(M - i\frac{\Gamma}{2}\right)\begin{pmatrix} |B(t)\rangle \\ |\bar{B}(t)\rangle \end{pmatrix} \tag{1.18}$$

where the Hamiltonian, $M - i\frac{\Gamma}{2}$, is time-independent, and M and Γ are separately Hermitian. CPT invariance ensures the B_q^0 and $\bar{B}_q^0$ particles have identical masses and decay rates, implying $M_{11} = M_{22}$ and $\Gamma_{11} = \Gamma_{22}$. The eigenstates of the system, the mass eigenstates, evolve through time as

$$\begin{aligned} |B_H(t)\rangle &= e^{-iM_H t - \frac{\Gamma_H}{2}t}|B_H(0)\rangle \\ |B_L(t)\rangle &= e^{-iM_L t - \frac{\Gamma_H}{2}t}|B_L(0)\rangle \end{aligned} \tag{1.19}$$

where

$$|B_H\rangle = p|B_q^0\rangle - q|\bar{B}^0\rangle,\ |B_L\rangle = p|B_q^0\rangle + q|\bar{B}^0\rangle,\ |p|^2 + |q|^2 = 1, \tag{1.20}$$

are referred to as the heavy (H) and light (L) mass eigenstates. If there is no CP violation in mixing $|p/q| = 1$.

The eigenvalues are, expanding in the phenomenologically small quantity $|\frac{\Gamma_{12}}{M_{12}}|$ to $\mathcal{O}(|\frac{\Gamma_{12}}{M_{12}}|^2)$,

$$\begin{aligned} M_H &= M_{11} + |M_{12}| \qquad \Gamma_H = \Gamma_{11} - |\Gamma_{12}|\cos\phi \\ M_L &= M_{11} - |M_{12}| \qquad \Gamma_L = \Gamma_{11} + |\Gamma_{12}|\cos\phi \\ \phi &= \arg(-\frac{M_{12}}{\Gamma_{12}}). \end{aligned} \tag{1.21}$$

and the coefficients for the eigenvectors are

$$\frac{q}{p} = -\frac{\Delta M_q + \frac{i}{2}\Delta\Gamma_q}{2M_{12} - i\Gamma_{12}} \tag{1.22}$$

The fact that $|\Gamma_{12}/M_{12}| \ll 1$ can be understood by considering that the magnitude of the amplitudes increases with the mass of the heaviest quark in their loops, and M_{12} has virtual top quarks in it, while Γ_{12} has only real quarks as intermediate states, u and c.

The mass and width differences of these eigenstates are

$$\begin{aligned}\Delta M_q &= M_H - M_L = 2|M_{12}| + \mathcal{O}(|\frac{\Gamma_{12}}{M_{12}}|^2) \\ \Delta\Gamma_q &= \Gamma_L - \Gamma_H = 2|\Gamma_{12}|\cos\phi + \mathcal{O}(|\frac{\Gamma_{12}}{M_{12}}|^2).\end{aligned} \tag{1.23}$$

These quantities govern the time evolution of a pure B_q^0 or $\bar{B}_q^0$ state from $t = 0$ as

$$\begin{aligned}|B_q^0(t)\rangle &= g_+(t)|B_q^0\rangle + \frac{q}{p}g_-(t)|\bar{B}_q^0\rangle, \\ |\bar{B}_q^0(t)\rangle &= g_+(t)|\bar{B}_q^0\rangle + \frac{q}{p}g_-(t)|B_q^0\rangle,\end{aligned} \tag{1.24}$$

where

$$g_\pm(t) = \frac{e^{-\Gamma_q t}}{2}\left[\cosh(\frac{\Delta\Gamma_q}{2}t) \pm \cos(\Delta m_q t)\right], \tag{1.25}$$

and $\Gamma_q = (\Gamma_H + \Gamma_L)/2$.

The off-diagonal matrix elements, M_{12} and Γ_{12}, can be calculated by evaluating the box diagrams in Fig. 1.2 to obtain expressions for the measurable quantities ΔM_q and $\Delta\Gamma_q$,

$$\Delta M_q = 2|M_{12}| = \frac{G_F^2 M_W^2}{6\pi^2}|V_{tq}^* V_{tb}|^2 \eta_2^B S_0(x_t) M_{B_q} f_{B_q}^2 \hat{B}_{B_q}, \tag{1.26}$$

$$\Delta\Gamma_q = 2|\Gamma_{12}|\cos\phi = \frac{G_F^2 m_b^2}{12\pi M_{B_q}}|V_{cb}^* V_{cs}|^2 \left[c_L(z)\langle Q_1\rangle + c_S(z)\langle Q_2\rangle\right] \qquad z = m_c^2/m_b^2 \tag{1.27}$$

where $x_t = m_t^2/M_W^2$, $S_0(x_t)$ is the Inami-Lim function, η_2^B is a perturbative QCD correction coefficient, and $c_L(z)$, $c_S(z)$ are Wilson coefficients. $|V_{tq}^* V_{tb}|$ are the CKM matrix elements, and $\frac{8}{3}f_{B_q}^2 B_{B_q} m_{B_q}^2 = \langle\bar{B}_q^0|\bar{q}\gamma_\mu(1-\gamma_5)b\bar{q}\gamma^\mu(1-\gamma_5)b|B_q^0\rangle$ is the hadronic matrix element and can only be calculated non-perturbatively. $|V_{tb}| = 0.999100^{+0.000034}_{-0.000004}$ is known to high percision, and therefore a comparison between experimental measurements of ΔM_q and theoretical predictions can be used to determine $|V_{tq}|$.

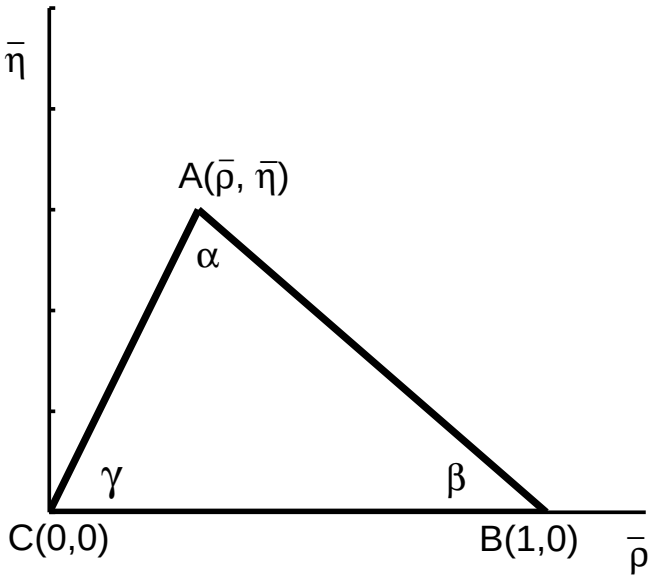

Figure 1.3: The CKM Unitarity Triangle.

B Mixing's Impact on the CKM Unitarity Triangle Analysis

The ratio of CKM matrix elements $|\frac{V_{td}}{V_{ts}}|$ is particularly important because it provides strong constraints on the CKM Unitarity Triangle

$$V_{ud}V_{ub}^* + V_{cd}V_{cb}^* + V_{td}V_{tb}^* = 0. \tag{1.28}$$

The Unitarity Triangle is usually normalized as

$$\begin{aligned} &\frac{V_{ud}V_{ub}^*}{-V_{cd}V_{cb}^*} + \frac{V_{td}V_{tb}^*}{-V_{cd}V_{cb}^*} = 1 \\ &\rightarrow (\bar{\rho} + i\bar{\eta}) + (1 - \bar{\rho} + \bar{\eta}) = 1 \\ &\rightarrow \sqrt{\bar{\rho}^2 + \bar{\eta}^2}e^{i\gamma} + \sqrt{(1-\bar{\rho})^2 + \bar{\eta}^2}e^{-i\beta} = 1 \end{aligned} \tag{1.29}$$

where the CKM matrix elements have been rewritten in the Wolfenstein parametrization and

$$\bar{\rho} = (1 - \frac{1}{2}\lambda^2)\rho, \quad \bar{\eta} = (1 - \frac{1}{2}\lambda^2)\eta. \tag{1.30}$$

The triangle is shown in Fig. 1.3, with

$$\gamma = \arg(-\frac{V_{ud}V_{ub}^*}{V_{cd}V_{cb}^*}), \quad \beta = \arg(-\frac{V_{cd}V_{cb}^*}{V_{td}V_{tb}^*}), \quad \alpha = \arg(-\frac{V_{td}V_{tb}^*}{V_{ud}V_{ub}^*}). \tag{1.31}$$

The ratio of V_{td} and V_{ts} in the Wolfenstein parametrization is

$$|\frac{V_{td}}{V_{ts}}| = \lambda\sqrt{[1-\bar{\rho})^2 + \bar{\eta}^2}, \tag{1.32}$$

and is used in the standard Unitarity Triangle fit [8]. It gives the length between vertices B and A.

The ratio of CKM matrix elements can be determined from the combination of the measured mass differences and a calculation of the $SU(3)$ breaking ratio ξ on the lattice

$$|\frac{V_{td}}{V_{ts}}| = \frac{f_{B_s}\sqrt{B_{B_s}}}{f_{B_d}\sqrt{B_{B_d}}}\sqrt{\frac{\Delta M_d M_{B_s}}{\Delta M_s M_{B_d}}} = \xi\sqrt{\frac{\Delta M_d}{\Delta M_s}\frac{M_{B_s}}{M_{B_d}}}. \tag{1.33}$$

The measured values for the mass differences are [11][43]

$$\Delta M_d = 0.507 \pm 0.005\,\mathrm{ps}^{-1} \tag{1.34}$$

$$\Delta M_s = 17.77 \pm 0.10(\mathrm{stat.}) \pm 0.07(\mathrm{syst.})\,\mathrm{ps}^{-1} \tag{1.35}$$

The current determination for the ratio $|V_{td}/V_{ts}|$ is obtained using the above experimental measurements combined with lattice calculations for ξ,

$$|V_{td}/V_{ts}| = \xi\sqrt{\frac{\Delta M_d}{\Delta M_s}\frac{m_{B_s}}{m_{B_d}}} = 0.2060 \pm 0.0007(\mathrm{exp.})^{+0.0081}_{-0.0060}(\mathrm{theo.}), \tag{1.36}$$

where the theoretical uncertainty, $\sim 4\%$, dominates the total uncertainty. The value of ξ used in Eq. (1.36) is [43]

$$\xi = \frac{f_{B_s}\sqrt{B_{B_s}}}{f_{B_d}\sqrt{B_{B_d}}} = 1.21^{+0.047}_{-0.035}. \tag{1.37}$$

This calculation of ξ is, however, a combination of calculations: one of f_{B_s}/f_{B_d} from the HPQCD collaboration [18], and one of B_{B_s}/B_{B_d} from the JLQCD collaboration [3]. It is important to note that, while the calculation of f_{B_s}/f_{B_d} was done with 2+1 dynamical sea quarks, the calculation of B_{B_s}/B_{B_d} was done with only 2 dynamical sea quarks and suffers from uncontrolled systematic errors. Neglecting sea quark effects in a lattice calculation is referred to as quenching. A quenched theory has no quantitative connection to QCD and has completely uncontrolled systematic errors. While it is reasonable to neglect the sea charm, bottom, and top quarks because their masses are much greater than the QCD scale, Λ_{QCD}, neglecting the much lighter sea strange quark is an uncontrolled approximation.

This report attempts to improve on the current situation by providing a complete calculation of ξ with systematic errors conservatively accounted for. In the process the matrix elements $\langle \bar{B}^0_d|\bar{d}\gamma_\mu(1-\gamma_5)b\bar{d}\gamma^\mu(1-\gamma_5)b|B^0_d\rangle$, $\langle \bar{B}^0_s|\bar{s}\gamma_\mu(1-\gamma_5)b\bar{s}\gamma^\mu(1-\gamma_5)b|B^0_s\rangle$ are separately calculated. It will be seen that we were not able to reduce the uncertainty in ξ below 4%, however the errors and central values of our determination can be considered more reliable than previous calculations: there is no uncontrolled systematic error such as quenching the strange sea quark.

The organization of this report and calculation is outlined below:

- Chapter 2 overviews basic lattice field theory techniques with a focus on those used in our calculation. The setup of our calculation is also described.
- Chapter 3 explains the methods for the two- and three-point correlator fits used to extract the mixing matrix elements. Results are presented.
- Chapter 4 describes the perturbative calculation necessary to connect the lattice results to continuum results. The calculation is referred to as perturbative matching and is used to correct for the difference between the UV behavior in the continuum and on the lattice.
- Chapter 5 overviews chiral perturbation theory. The chiral expressions for the mixing matrix elements are presented here.
- Chapter 6 describes the methods used in the chiral fits and extrapolations and presents results for the mixing matrix elements.
- Chapter 7 explores and estimates the systematic errors present in our calculation. Final results for the matrix elements and total estimated errors are presented.
- Chapter 8 presents the final results of this report's analysis. It also describes the next steps in the calculation that are already underway. It should be noted that the perturbative matching calculation is not yet finalized and so values for the matrix elements themselves are not final. The result presented for the ratio, ξ, can however be considered final since the matching calculation will not significantly affect it.

Chapter 2

Lattice QCD

The degrees of freedom in the QCD action are individual quarks and gluons. QCD is however strongly interacting at the energies of hadrons, and has a property known as confinement: in nature QCD's fundamental quark and gluon particles are always bound into colorless states called hadrons, and the force between the quarks and gluons only increases as they are separated. Experimental measurements of QCD governed processes therefore only detect hadrons, which are either composed of quark anti-quark states, mesons, or three quark (or anti-quark) states, baryons.

Confinement is generally understood to be a consequence of the non-abelian gauge structure of QCD, with the physical interpretation that it is due to the ability of the charged gluons to interact with each other. These interactions cause the strong coupling constant, α_s, to grow stronger with decreasing energy or increasing distance between the particles. At higher energies α_s becomes small enough for perturbation theory to work, which has allowed analytic predictions for high energy QCD processes to be made and compared with experiment. The behavior of α_s is referred to as asymptotic freedom. The success of these comparisons is one indicator that QCD is the theory of strong interactions. However, perturbative methods don't work for soft processes and cannot be used for calculations of QCD governed quantities such as hadronic matrix elements. The only known way to perform such a calculation with systematically reducible errors is through a non-perturbative method known as Lattice QCD.

Observables in field theory are related to vacuum expectation values of operators which can be calculated by path integration

$$\langle \mathcal{O}(t_1, t_2, \ldots \rangle = \langle 0 | T \left[\mathcal{O}(t_1, t_2, \ldots \right] | 0 \rangle = \frac{\int DAD\bar{\psi}D\psi \mathcal{O}(t_1, t_2, \ldots) e^{-iS}}{\int DAD\bar{\psi}D\psi e^{-iS}}, \quad (2.1)$$

where T is the time ordering operator and S is the action of the theory. In some theories, such as QED, the path integral can be series expanded in powers of the coupling constant, and vacuum expectation values perturbatively calculated. The series expansions in QED tend to quickly converge because the coupling, α_e, is approximately $1/137$, very small.

As mentioned above the behaviour of QCD is quite different. Assuming the energy scale, q, is large a one-loop calculation is adequate to describe the

evolution of the strong coupling

$$\alpha_s(q^2) = \frac{2\pi}{(11 - \frac{2}{3}n_f)\log(q^2/\Lambda^2_{\rm QCD})}, \tag{2.2}$$

where n_f is the number of quark flavors in the theory. As q decreases and becomes comparable to $\Lambda_{\rm QCD}$ Eq. 2.2 shows that α_s becomes very large. $\Lambda_{\rm QCD}$ ranges from 100-300 MeV and QCD is typically not perturbative until $q > 1\,GeV$.

Wilson developed a non-perturbative approach to evaluate the path integral. He places the theory on a discrete space-time lattice, which converts the infinite dimensional integral above into a finite dimensional one which can be numerically evaluated [41]. This method necessarily introduces statistical errors from the numerical integration, and systematic errors from the effects of discretization. There are many other errors that are introduced in this method that will be described throughout this report. However, unlike other methods for calculating QCD governed quantities, Lattice QCD provides a way to quantify and systematically reduce all errors in a calculation.

This chapter provides an overview of general Lattice QCD techniques, with a focus on those methods that are relevant to our calculation of the B mixing hadronic matrix elements.

2.1 Numerical Evaluation of the Path Integral

Before numerical methods can be employed we must first Wick rotate the path integral into four-dimensional Euclidean space. By doing so the difficult to evaluate oscillating exponential becomes an exponential damping

$$Z = \int DA(x)D\bar{\psi}(x)D\psi(x)e^{-S_{QCD}}. \tag{2.3}$$

$S_{\rm QCD}$, the QCD action in Euclidean space, is

$$S_{\rm QCD} = \int d^4x \sum_q \bar{\psi}_q(x)(\not{D} + m_q)\psi_q(x) - \frac{1}{4}F^a_{\mu\nu}F_a^{\mu\nu}, \tag{2.4}$$

where $F^a_{\mu\nu} = \partial_\mu A^a_\nu(x) - \partial_\nu A^a_\mu(x) + g f^{abc} A^b_\mu(x) A^c_\nu(x)$ is the gluon field strength, $D_\mu = \partial\mu - igA^a_\mu(x)T^a$ is the gauge covarient derivative, and q labels the quark flavor.

The are many ways to discretize the theory which will later be described, but for now we will assume a suitable one has been chosen. In this case the functional path integral measure becomes a standard integration (although of extremely high dimension if N is large) with the fields as variables on lattice

sites N

$$DA(x)D\bar{\psi}(x)D\psi(x) \rightarrow DUD\bar{\psi}D\psi \equiv \prod_{i}^{N} dU_i d\bar{\psi}_i d\psi_i. \tag{2.5}$$

The first step in numerically evaluating the discretized path integral is to integrate over the fermion fields: because we only consider actions which are bilinear in the fermion fields, and they are Grassman variables, the integration is straightforward

$$\begin{aligned} Z = \int DUD\bar{\psi}D\psi e_{i}^{S_g(U)-\sum_i \bar{\psi}_i M_f(U)\psi} = \\ \int DUDet[M_f(U)]e^{S_g(U)} = \int DUe^{S_g(U)-\mathrm{tr}\,[\log M_f(U)]}, \end{aligned} \tag{2.6}$$

where S_g is the gluon action and M_f is the fermion matrix. The path integral is now entirely in terms of the gauge fields, U. The highly peaked, high dimension path integral can then be evaluated numerically using Monte Carlo techniques with importance sampling such as described in Ref. [36]. [1] Correlation functions involving the fermion fields can also be written in terms of the gauge fields,

$$\langle \psi_x \bar{\psi_y} \rangle = Z^{-1} \int DUe^{S_g(U)+\mathrm{tr}\,[\log M_f(U)]} S_{xy}(U), \tag{2.7}$$

where $S_{xy}(U)$ is the fermion propagator.

A typical lattice calculation works as follows. A large number of gauge configurations are generated with some importance sampling algorithm, such as Metropolis, which generates gauge configurations using a probability governed by the exponential in Eq. (2.6). The desired correlation function is Wick contracted so that it is written in terms of propagators. The fermion action is then constructed on the background gauge fields. The fermion action is then inverted to obtain the fermion propagator, and then tied together with other fermion propagators to obtain the desired correlation function. This is done on all the gauge configurations and the correlation functions averaged. In the limit of a large number of configurations this averaging is equivalent to integration of the path integral. Techniques that will be described later in the chapter are then used to extract the parameters of interest, usually masses or amplitudes, from the correlation function.

There are several important considerations about the method just described

[1] In practice numerical integration is not so straightforward as implied above. There is an enormous amount of research and effort in developing efficient actions and integration algorithms, with advantages and trade-offs in each choice of method that must be carefully considered. In fact for years the calculation of $Det[M_f(U)]$ was computationally unfeasible as it is by far the most computationally expensive part of the integral evaluation. In the past this term was set to a constant, a process referred to as quenching, which introduces an uncontrolled approximation because there are no sea quark loops. Only in the past decade has it become possible to simulate unquenched QCD, with 3 flavors of sea quarks (the heaviest 3 quark flavors have masses$\gg \Lambda_{\mathrm{QCD}}$ and so the effects of their absence is negligible and errors due to their absence can be estimated).

which are relevant to phenomenological calculations:

- Lattice spacing: As the lattice spacing, a, is made smaller more lattice points are required in order to maintain the same physical volume, requiring more computational resources. Lattice calculations using dynamical fermions typically scale as $(\frac{L}{a})^4(\frac{1}{a})\frac{1}{m_\pi^2 a}$. Lattice spacings used in this analysis range from $0.09 - 0.15$fm. Lattice spacing artifacts scale as powers of a. It is possible to reduce the effects of these artifacts in most actions by adding irrelevant terms using a formalism known as Symanzik improvement. Through the improvement process an action that had discretization errors that scaled as a is modified so as to have errors that scale as a^n, where $n > 1$. The improved action is typically more complex, and so more computationally demanding; however, improvement is usually less computationally demanding than making the lattice spacing smaller.

- Determinant and Propagator calculation: The the speed of the algorithms used to calculate the determinant and the propagators generally decrease as the quark masses become lighter. The lightest sea and valence quark masses used in this calculation are $m_s/10$, where m_s is the mass of the strange quark. Quantities cannot be calculated at physical light quark masses, so Chiral Perturbation Theory is usually necessary to perform an extrapolation on the lattice data from the lattice masses to the physical light quark masses.

- Finite size effects: The length of the sides of the lattice must be large compared to the pion wavelength, $L \gg 1/am_\pi$, otherwise the pions will interact with their mirror images (periodic boundary conditions are typically used in lattice calculations). Calculations presented in this analysis are performed on lattices with spatial lengths of ≈ 2.5fm. Finite size effects are typically very small and under good control on the MILC collaborations configurations, the configurations the B mixing analysis is performed on. This is partly due to the fact that the light quarks are heavier than their physical counterparts.

All the above considerations and their particular relevance to B mixing are discussed in this report.

2.2 From the Continuum to the Lattice

This section describes the transcription of fermionic and bosonic fields from the continuum to the lattice. The method of discretizating the action is not unique, and the most basic discretizations are presented. In later sections these discretizations are modified to arrive at the actions used in the B mixing calculation.

2.2.1 Transcription of QCD Fields to the Lattice

Discretization of the continuum theory will break certain symmetries of QCD depending on how it is implemented, an unavoidable instance being the reduction of the continuum's Euclidean symmetry to a the hyper-cubic group's discrete 90° rotational symmetry. However, as long as these symmetries are recovered in the continuum limit a controlled and systematic approximation to continuum QCD is possible.

The most important symmetry to maintain is that of the strong interaction's, the SU(3) gauge symmetry. Without this symmetry the multiple couplings that would arise in its absence would have to be carefully tuned so as to recover the gauge symmetry in the continuum limit. Wilson's transcription of the continuum fields to the lattice preserves this symmetry [41].

In order to preserve gauge symmetry a method must be devised to account for the phase shift a fermion in the continuum acquires when moving from a space-time point x to y

$$\psi(y) = \mathcal{P} e^{\int_x^y igA_\mu(x)dx_\mu} \psi(x). \tag{2.8}$$

Wilson substituted a discrete version of the path ordered product into Eq. (2.8), referred to as a link variable

$$U(x, x+\hat{\mu}) \equiv U_\mu(x) = e^{iagA_\mu(x+\frac{\hat{\mu}}{2})} \tag{2.9}$$

$$U(x, x-\hat{\mu}) \equiv U_{-\mu}(x) = e^{-iagA_\mu(x-\frac{\hat{\mu}}{2})} = U^\dagger(x-\hat{\mu}, x), \tag{2.10}$$

so that Eq. (2.8) becomes

$$\psi(x+\hat{\mu}) = U_\mu(x)\psi(x), \tag{2.11}$$

where $U_\mu(x)$ is an SU(3) matrix element and x is a lattice site. The transcribed fermion fields are located on lattice sites, and gauge fields are links connecting lattice sites. Under a gauge transformation the link variable transforms as

$$U_\mu(x) \to V(x)U_\mu(x)V^\dagger(x+\hat{\mu}) \tag{2.12}$$

and the fermion fields as

$$\psi(x) \to V(x)\psi(x) \tag{2.13}$$

$$\bar{\psi}(x) \to \bar{\psi}(x)V^\dagger(x) \tag{2.14}$$

where $V(x)$ is also an element of SU(3). It can be seen that by forming closed loops of link variables or strings of link variables with fermions capping the ends that gauge invariant objects can be constructed.

2.2.2 Gauge Action

The most basic loop that can be constructed is the plaquette

$$P_{\mu\nu} = \frac{1}{3}\mathrm{Re}\,\mathrm{Tr}(U_\mu(x)U_\nu(x+\hat{\mu})U_\mu^\dagger(x+\hat{\nu})U_\nu^\dagger(x)). \tag{2.15}$$

The plaquette can be used to construct an action for the gauge fields

$$S_W = \beta\sum_x\sum_{\mu<\nu}\mathrm{Re}\,\mathrm{Tr}\frac{1}{3}(1-P_{\mu\nu}) \tag{2.16}$$

commonly referred to as the Wilson gluon action [41]. The connection between the Wilson gluon action and the continuum gluon action can be seen by expanding Eq. (2.15) in powers of the lattice spacing a

$$P_{\mu\nu} = 1 - \frac{a^4}{6}\mathrm{Tr}[g^2F^{\mu\nu}F_{\mu\nu}] + \frac{a^2}{6}F_{\mu\nu}(\partial_\mu^2 A_\nu - \partial_\nu^3 A_\mu) + \mathcal{O}(a^8) \tag{2.17}$$

to get

$$S_W = \beta\sum_x\sum_{\mu<\nu}\frac{a^4}{6}\mathrm{Tr}[g^2F^{\mu\nu}F_{\mu\nu}] + \mathcal{O}(a^6). \tag{2.18}$$

In the limit $a \to 0$

$$S_W = \int d^4x\frac{1}{2}\mathrm{Tr}[g^2F^{\mu\nu}F_{\mu\nu}] + \mathcal{O}(a^2) \tag{2.19}$$

where $\beta = \frac{6}{g^2}$. From the above procedure it is clear that discretization errors in the Wilson gluon action begin at $\mathcal{O}(a^2)$.

2.2.3 Naive and Wilson Fermion Actions

The transcription of the fermion fields to the lattice appears straightforward at first, but a problem with their physical interpretation quickly arises, known as the doubling problem. An extra mode for each component of the momentum appears because of the periodicity of the transcribed fermions' Brillouin zone.

To see why doubling occurs consider the naive discretization of the massless continuum Euclidean fermion lagrangian

$$\begin{aligned}&\bar{\psi}(x)\gamma_\mu D_\mu\psi(x) \\ &\to \frac{1}{2a}\bar{\psi(x)}\sum_\mu\gamma_\mu\left[U_\mu(x)\psi(x+\hat{\mu}) - U_\mu^\dagger(x-\hat{\mu})\psi(x-\hat{\mu})\right]\end{aligned} \tag{2.20}$$

As an aside note that expanding the kinetic term in powers of the lattice spacing

one gets

$$\begin{aligned}&\frac{1}{2a}\bar{\psi(x)}\gamma_\mu[(1+iagA_\mu(x+\hat{\mu}/2)+\cdots)(\psi(x)+a\partial_\mu\psi(x)+\cdots) \\ &-(1-iagA_\mu(x-\hat{\mu}/2)+\cdots)(\psi(x)-a\partial_\mu\psi(x)+\cdots)] \\ &=\bar{\psi}(x)\gamma_\mu\partial_\mu\psi(x)+ig\bar{\psi}(x)\gamma_\mu A_\mu(x)\psi(x)+\mathcal{O}(a^2),\end{aligned} \tag{2.21}$$

and so lattice errors in the Naive action begin at $\mathcal{O}(a^2)$. The inverse of the momentum-space propagator of the massless, free field naive fermion action, Eq. 2.20, is

$$S^{-1}(p)=\frac{i}{a}\sum_\mu\gamma_\mu\sin(p_\mu a). \tag{2.22}$$

This propagator has 16 poles at

$$p_\mu=\{(0,0,0,0),(\pi/a,0,0,,0),\ldots(\pi/a,\pi/a,\pi/a,\pi/a)\}, \tag{2.23}$$

corresponding to 16 particles, often called tastes to distinguish them from quark flavor. This is the doubling problem. The 15 tastes that don't arise in the continuum are unphysical and must be removed or accounted for in the theory. This unfortunate property is general to fermions on the lattice and described by the Nielsen-Ninomiya no-go theorem, which states no local, doubler free, and chirally symmetric fermion action can be constructed [33]. Because the different tastes lie on the edges of the periodic Brilliouin zone and can interact via gluon exchange, they have the ability to exchange a gluon with momentum of order π/a with fermions of another taste, and in the process change both fermions' tastes. These unphysical processes are referred to as taste changing interactions.

Fermion actions can be constructed which lack chiral symmetry (but which regain it in the continuum limit) and effectively remove the additional tastes and their interactions. One such action is known as the Wilson fermion action and is constructed by the addition of an irrelevant operator $ar\bar{\psi}\partial^2\psi$ (∂^2 is the lattice laplacian),

$$\begin{aligned}\frac{1}{2a}\sum_x\bar{\psi}(x)[(\gamma_\mu-r)U_\mu(x)\psi(x+\hat{\mu})-(\gamma_\mu+r)U_\mu^\dagger(x-\hat{\mu})\psi(x-\hat{\mu})] \\ +\frac{ma+4r}{a}\sum_x\bar{\psi(x)}\psi(x),\end{aligned} \tag{2.24}$$

where $0<r<1$. The inverse of the propagator in Eq. (2.24) is

$$S_W^{-1}=m+\frac{r}{a}\sum_\mu[1-\cos(p_\mu a)+\frac{i}{a}\gamma_\mu\sin(p_\mu a)]. \tag{2.25}$$

In the Wilson propagator all but the $p_\mu=(0,0,0,0)$ mode have a mass proportional to $\frac{r}{a}$, causing them to decouple in the continuum limit. Unfortunately the

Wilson fermion action breaks chiral symmetry at $\mathcal{O}(a)$ and has discretization errors at $\mathcal{O}(a)$.

Another problem with the Wilson fermion action is that its mass is additively and multiplicatively renormalized. This amounts to the possibility that, for fermions with masses of $\mathcal{O}(\Lambda_{\rm QCD})$, the statistical and quantum fluctuations on the configurations will give rise to zero modes in the propagator, allowing the fermion propagator to be singular for certain configurations. This means it cannot be unambiguously inverted causing large fluctuations in the correlation functions. This issue is not a concern for heavy fermions, where $m_{fermion} \gg \Lambda_{\rm QCD}$.

2.2.4 Staggered Fermion Action

If one wants to calculate correlation functions using light quark masses near to or less than the QCD scale a fermion discretization is required that retains chiral symmetry. The naive action is chirally symmetric, and in fact is what we use to simulate the light quarks in our operators. In practice however, it is much more computationally efficient when computing the propagator and fermion determinant to use a trick known as spin diagonalization, reducing the number of degrees of freedom by $\frac{1}{4}$ as was done first by Kogut and Susskind in Ref. [22]. From the resulting action, known as the staggered action, a staggered propagator can be computed. The naive propagator can be immediately recovered from the staggered propagator, as will be demonstrated below.

By defining the staggered fields as

$$\psi(x) = \Gamma(x)\chi(x) \quad \bar{\psi}(x) = \bar{\chi}(x)\Gamma(x)^\dagger \quad \Gamma(x) = \gamma_1^{x_1}\gamma_2^{x_2}\gamma_3^{x_3}\gamma_4^{x_4} \tag{2.26}$$

the naive action becomes

$$\begin{aligned} &S_{naive} \to S_\chi = m\sum_x \bar{\chi}(x)\chi(x) \\ &+\frac{1}{2}\sum_{x,\mu}\bar{\chi}(x)\eta_\mu(x)(U_\mu(x)\chi(x+\hat{\mu}) - U_\mu^\dagger(x-\hat{\mu})\chi(x-\hat{\mu})), \\ &\eta_\mu(x) = (-1)^{\sum_{\nu<\mu} x_\nu} \end{aligned} \tag{2.27}$$

The fermion spin components are now decoupled, and only one spin component need be kept for each site. There are now effectively four copies of fermions, referred to as tastes, with discretization errors starting at $\mathcal{O}(a^2)$.

The staggered action mixes Dirac indices with space-time points making it difficult to interpret the taste and spin of staggered quarks in terms of Dirac fermions and the construction of operators difficult. After the staggered propagator is generated it is useful to convert it to a naive propagator via the simple

relation [42]

$$S_{naive}(x,y) = \Gamma(x)\Gamma^{\dagger}(y)S_{staggered}(x,y). \tag{2.28}$$

Gauge configurations and correlation functions constructed using the the staggered or naive propagator have taste violating effects. These unphysical interactions can be suppressed as described in a later section. In heavy-light systems, where the heavy quark is wilson-like, i.e. contains no doublers in its propagator, it can be shown that taste violating interactions are very restricted. We demonstrate this also in a later section.

2.3 Symanzik Improvement

As mentioned in the previous sections it is possible to improve the actions and operators by explicitly adding irrelevant operators to the lattice theory which effectively cancel the lattice spacing a's effects to a given order. The procedure used in this analysis is referred to as the Symanzik improvement program [40].

The lattice theory (S_L) can be thought of as a low energy effective theory (Symanzik effective theory) for continuum QCD (S_{QCD}) with a hard cut-off at π/a. Introducing such a cutoff causes new interaction terms in the action

$$S_{QCD} = S_L + \sum_{n>4} a^n \sum_i c_{ni}\mathcal{S}_{ni} \tag{2.29}$$

and mixing in the operators

$$O_{QCD} = O_L + \sum_{n>4} a^n \sum_i d_{ni}\mathcal{O}_{ni}. \tag{2.30}$$

Therefore lattice artifacts enter into the calculation in powers of a, and can be removed by including the appropriate terms and coefficients into the lattice action and operator to whatever order is desired.

For a simple example consider the kinetic term in the free naive fermion lagrangian

$$\frac{\bar{\psi}(x+a\hat{\mu}) - \psi(x-a\hat{\mu})}{2a} = \bar{\psi}(x)\partial_\mu\psi(x) + \frac{a^2}{6}\bar{\psi}(x)\partial_\mu^3\psi(x) + \mathcal{O}(a^4) \tag{2.31}$$

From the above it is clear that to remove the $\mathcal{O}(a^2)$ errors in the free naive action it is sufficient to add the operator $\bar{\psi}(x)\partial_\mu^3\psi(x)$ with coefficient $-\frac{1}{6}$ to the action. This is in fact done in the case of the improved staggered/naive actions discussed later, and is referred to as the Naik term.

Of course this is only a tree level calculation. There are additional discretization errors arising with powers of α_s that are not removed by tree level improvement due to quantum effects.. If quantum effects up to order m are to be included m-loop calculations must be performed to the desired level of

accuracy, making sure that all $m-$loop quantities are improved to that level of accuracy. These additional improvements appear as coefficients times powers of $\alpha_s^m a^n$. In practice it requires long and tedious calculations to improve operators and actions beyond one-loop.

2.3.1 Improvement of the Wilson Gauge Action: MILC Gauge Action

The Wilson gauge action has discretization errors at $\mathcal{O}(a^2)$. Using the Symanzik improvement scheme we look for dimension 6 operators that can be used to remove these errors. There are only three types of 6 link loops

$$R_{\mu\nu} = \mathrm{tr}\,(D_\mu F_{\mu\nu} D_\mu F_{\mu\nu}), \tag{2.32}$$

$$\begin{aligned} T_{\mu\nu\rho} &= \mathrm{tr}\,(D_\mu F_{\nu\rho} D_\mu F_{\nu\rho}), \\ L_{\mu\nu\rho} &= \mathrm{tr}\,(D_\mu F_{\mu\rho} D_\nu F_{\nu\rho}), \end{aligned} \tag{2.33}$$

the rectangular, twisted, and L type loops.

At tree level only one loop, $R_{\mu\nu}$, is needed to remove the $\mathcal{O}(a^2)$ errors. To remove the $\mathcal{O}(\alpha_s a^2)$ errors $T_{\mu\nu\rho}$ is also needed. Through a one-loop calculation the appropriate coefficients for the various operators can be determined to arrive at the Symanzik improved gluon action

$$S_{SG} = \beta_P \sum_{\mu<\nu}(1 - P_{\mu\nu}) + \beta_R \sum_{\mu\neq\nu}(1 - R_{\mu\nu}) + \beta_T \sum_{\mu<\nu<\rho}(1 - T_{\mu\nu\rho}), \tag{2.34}$$

where

$$\beta_P = \frac{10}{g^2}, \quad \beta_R = -\frac{1}{2g^2}(1 + 0.4805\alpha_s), \quad \beta_T = -\frac{10}{g^2}0.03325\alpha_s. \tag{2.35}$$

Mean-field Improvement (Tadpole Improvement)

There is an additional improvement that is not immediately obvious, but which greatly improves the convergence of perturbatively calculated quantities, referred to as tadpole improvement [25]. To see the necessity of this step consider the expectation value of the small a expanded link variable

$$\begin{aligned} \langle U_\mu(x)\rangle &= \langle 1 + iagA_\mu(x) - a^2 g^2 A_\mu(x) A\mu(x) + \cdots \\ &= 1 - a^2 g^2 \langle A_\mu(x) A_\mu(x)\rangle + \cdots \end{aligned} \tag{2.36}$$

where the tadpole term using the Wilson gluon action is

$$\langle A_\mu(x) A_\mu(x)\rangle = \int_{-\pi/a}^{\pi/a} d^4k \frac{1}{(\frac{2}{a}\sum_\mu \sin\frac{k_\mu a}{2})^2} \tag{2.37}$$

in the Feynman gauge. As Lepage and Mackenzie pointed out, although the tadpole terms are formally suppressed by powers of $\alpha_s^2 a^2$, the integral is proportional to a^2 and cancels part of this suppression, reducing it to to a α_s^2 suppression. The fact that the tadpole diagrams tend to have very large values adds to this problem, making perturbative corrections much larger than naively expected.

We would like the expectation value of the link field to be the same as in the continuum, 1. To do this it is useful to integrate out the UV part of the link field, which is mostly composed of tadpole diagrams

$$U_\mu(x) = e^{iagA_\mu^{UV}} e^{iagA_\mu^{IR}} = u_0 e^{iagA_\mu^{IR}}, \tag{2.38}$$

where u_0 is the average value of the link field, and consists of mostly tadpoles. This suggests that in the simulations we set $U_\mu \to U_\mu/u_0$, and determine u_0 nonperturbatively.

This simple change amounts to a redefinition of the couplings within the theory, where in the Wilson gluon action $g^2 \to \frac{g^2}{u_0^4} \equiv \tilde{g}^2$. In the Symanzik improved gluon action, through a redefinition of the fields, couplings change as

$$\beta_P \to \frac{10}{\tilde{g}^2}, \quad \beta_R \to -\frac{1}{2\tilde{g}^2 u_0^2}(1 + 0.4805\alpha_s), \quad \beta_T \to -\frac{10}{\tilde{g}^2 u_0^2} 0.03325\alpha_s. \tag{2.39}$$

In practice this adjustment causes lattice perturbation theory to behave much more like continuum perturbation theory. The Symanzik improved gluon action, in combination with the tadpole improvement, constitutes the MILC gauge action, which is used in all our simulations [7, 1, 28]. It is one-loop Symanzik improved with tadpole improvement and has discretization errors starting at $\mathcal{O}(a^4, \alpha_s a^2)$.

2.3.2 Improvement of the Wilson Action: Clover Action→Fermilab Interpretation

The Wilson action, Eq. (2.24), has errors starting at $\mathcal{O}(a)$, due to the dimension 5 Laplacian term. The Symanzik program tells us to find the other operators of dimension 5, because they will have also have coefficients proportional to a. There is in fact only one, known as the the Sheikoholeslami-Wohlert (clover) term [38],

$$O_{SW}(x) = c_{sw}\bar{\psi}(x)\sigma_{\mu\nu}F^{\mu\nu}(x)\psi(x) \tag{2.40}$$

where the clover approximation to the field strength is used

$$F_{\mu\nu}(x) = \frac{1}{8a^2} \sum_{\bar{\mu}=\pm\mu,\bar{\nu}=\pm\nu} \text{sign}(\bar{\mu}\bar{\nu}) U_{\bar{\mu}} U_{\bar{\nu}} U_{\bar{\mu}}^\dagger U_{\bar{\nu}}^\dagger - h.c. \tag{2.41}$$

(this approximation contains no $\mathcal{O}(a)$ errors).

On of the two dimension five operators, the Laplacian or clover term, is redundant: it can be produced through a change of variables in the path integral. The physics of the path integral cannot change due to a change in variables and so the coefficients multiplying them are to some extent arbitrary. In this case the Laplacian term is introduced to remove the doublers, and through the appropriate choice of c_{sw} the clover term removes the $\mathcal{O}(a)$ discretization errors. One way to determine an appropriate tree-level value for c_{sw} is to consider the quark gluon vertex on the lattice and in the continuum, where it can be seen that $c_{sw} = 1$ causes them to agree to $\mathcal{O}(a)$. If one wanted the lattice and continuum actions to agree to $\mathcal{O}(a\alpha_s)$ a one-loop calculation would be required to determine the appropriate c_{sw}.

The Wilson fermion action, with the additional Clover term, is referred to as the Clover action. It has discretization errors starting $\mathcal{O}(a\alpha_s, a^2)$. The action is conventionally simulated in the hopping parameter form

$$\kappa \sum_x \bar{\psi}(x)[(\gamma_\mu - r)U_\mu(x)\psi(x+\hat{\mu}) - (\gamma_\mu + r)U^\dagger_\mu(x-\hat{\mu})\psi(x-\hat{\mu})] \qquad (2.42)$$
$$+ \sum_x \bar{\psi}(x)\psi(x) + \sum_x O_{SW}(x),$$

where $\kappa \equiv \frac{1}{2(m_0 a + 4r)}$.

It is also necessary to tadpole improve the Clover action if good perturbative behaviour is to be expected,

$$\kappa \to \kappa u_0, \quad c_{sw} \to \frac{c_{sw}}{u_0^3}. \qquad (2.43)$$

Fermilab Interpretation

A form of the Clover action, formerly correct to $\mathcal{O}(a)$, is what we use in our simulations for the heavy b quark. We must consider, however, that around the charm and bottom masses $m_Q \gg \Lambda_{\rm QCD}$, and at the lattice spacings we use $m_Q a \geq 1$ for heavy-quarks. The usual expansion in powers of the lattice spacing arise as powers of a times the four-momentum, ap. These correction are small when $p \sim \mathcal{O}(\Lambda_{\rm QCD})$, but when $m_Q \gg \mathcal{O}(\Lambda_{\rm QCD})$ the discretization errors scale as am_Q and are no longer small. The wavelength of the heavy-quark is too small to be "resolved" by the lattice spacing, and its dynamics are missed.

Heavy Quark Effective Theory (HQET) integrates out the heavy-quarks in QCD and includes their interactions as a systematic expansion in $\Lambda_{\rm QCD}/m_Q$. HQET tells us that it is not the total energy of the heavy-quark that is important to the dynamics of most processes, but rather the fluctuations about the energy of the heavy mass which are $\mathcal{O}(\Lambda_{\rm QCD})$. The fluctuations about the static quark limit, where $m_Q \to \infty$, are suppressed by powers of the quark mass, and so order by order the full theory can be built back up, where the size of the errors are proportional to some power of $\frac{\Lambda_{\rm QCD}}{m_Q}$. This suggests there may be ways

to use HQET to get the correct heavy-quark dynamics on the lattice without introducing large discretization errors.

There are currently two main approaches to simulating heavy-light systems in lattice simulations, both of which take advantage of HQET.

- Start at the static quark limit in continuum HQET, and add operators until continuum QCD and the HQET match to the desired order in $\frac{\Lambda_{\rm QCD}}{m_Q}$. Then discretize the HQET and match the lattice HQET to the continuum HQET to the desired order in a, resulting in a lattice theory that has errors arising as powers of m_Q^{-1} and a. This is a non-relativistic approach, and divergent as m_Q, or on the lattice $m_Q a$, is decreased. This is problematic, because no formal continuum extrapolation is possible, as $a \to 0$ $m_Q a \to 0$ and the "small" correction terms diverge. This approach has been heavily employed to simulate heavy-heavy and heavy-light systems [26].

- Start with the relativistic lattice theory, in this case the clover action, making no assumptions about the quark mass and allowing the temporal and spatial components of the action to differ. To do this we must retain the full mass dependence of the coefficients in the action. As was shown in Ref. [15], the actions and operators can then be matched to relativistic QCD for light-quarks, or non-relativistic HQET for heavy-quarks. Thus for heavy-quarks, rather than matching the operators and action in powers of ap to determine the improvement coefficients, they can be matched to the desired order in $a\vec{p}$ or equivalently $\Lambda_{\rm QCD}/m_Q$. The coefficients are bounded for all quark masses, and there is a smooth transition between the heavy and light quark limits, allowing quarks of any mass to be simulated using this action. This method is referred to as the Fermilab action or interpretation. For heavy-quarks the short distance interactions associated with the mass are not simulated on the computer but contained within the improvement coefficients. The error associated with the cutoff effects scales as powers of Λ_{QCD}/m_Q. This is the method we use to simulate the b quark in the B mixing calculation.

To see how the Fermilab interpretation works in practice and introduce some terminology consider the dispersion relation for the free Clover action where the full four-momentum dependence has been kept, and a factor ζ allows the weight of the spatial and temporal components to differ,

$$\cosh Ea = 1 + \frac{(1 + m_0 a + \frac{1}{2}\zeta\hat{p}^2 a^2)^2 + \zeta S^2 a^2}{2(1 + m_0 a + \frac{1}{2}\zeta\hat{p}^2 a^2)}, \tag{2.44}$$

where $S_i = a^{-1}\sin p_i a$ and $\hat{p}_i = 2a^{-1}\sin(p_i a/2)$ and $i = 1 - 3$. After expanding the dispersion relation in powers of $a\vec{p}$ we have

$$E^2 = M_1^2 + \frac{M_1}{M_2}\vec{p}^2 + \cdots, \tag{2.45}$$

where the rest mass is defined as

$$M_1 \equiv a^{-1} \log(1 + m_0 a) \tag{2.46}$$

and the kinetic mass as

$$M_2^{-1} \equiv \frac{2a\zeta}{m_0 a(2 + m_0 a)} + \frac{a\zeta}{1 + m_0 a}. \tag{2.47}$$

By tuning m_0 and ζ so that $M_1 = M_2 = m_Q$, where m_Q is the mass of the quark we wish to simulate, the relativistic continuum dispersion relation is approximated with discretization errors starting at $\mathcal{O}(\vec{p}^4 a/M_2^2)$. In heavy-light systems M_1 just causes an overall energy shift and all the interesting dynamics are created by M_2. Therefore we can set $\zeta = 1$ and tune m_0 so as to set $M_2 = m_Q$ [15].

By matching M_2 to m_Q as above, and the lattice and continuum residues with errors starting at $\mathcal{O}((a\vec{p})^2)$, we obtain a theory for heavy quarks that has discretization errors starting at $\mathcal{O}(\alpha_s \Lambda_{\rm QCD}/m_Q)$, $\mathcal{O}((\Lambda_{\rm QCD}/m_Q)^2)$. It has the same form as the relativistic Clover action, but with modified parameters. Tadpole improvement of the resulting action gives what is referred to as the Fermilab action. The same procedure must be carried out for the improvement of heavy-light operators being studied, and we will explicitly perform this for the B mixing matrix element later in this chapter.

2.3.3 Improvement of the Staggered Action: a Squared Tadpole Improved (Asqtad) Action

As discussed in Sec. 2.2.4, there are taste changing interactions in the staggered action at $\mathcal{O}(a^2\alpha_s)$. These interactions arise when a gluon with momentum of order π/a is exchanged between quarks within the theory. These interactions can be reduced if the high momentum, highly virtual gluons are sufficiently suppressed, which is exactly what the Asqtad action does [27]. The action, written before the spin diagonalization, looks like the usual naive action with the Naik improvement term,

$$S_{AsqTad} = \sum_x \bar{\psi}(x)(\gamma_\mu D'_\mu - \frac{a^2}{6}\gamma_\mu D^3_\mu + m)\psi(x), \tag{2.48}$$

where the links in D'_μ have been modified to suppress taste-changing interactions

$$D'_\mu\psi(x) = \frac{1}{2au_0}(V'_\mu(x)\psi(x+a\hat{\mu}) - V'^{\dagger}_\mu(x-a\hat{\mu})\psi(x-a\hat{\mu})), \quad (2.49)$$
$$V'_\mu = V_\mu(x) - \sum_{\rho\neq\mu}\frac{a^2(D_\rho)^2}{4}U_\mu(x),$$
$$V_\mu(x) = \prod_{\rho\neq\mu}(1+\frac{a^2D^{(2)}_\rho}{4})U_\mu(x).$$

The covariant second derivative is defined as

$$D^{(2)}_\rho U_\mu(x) = \frac{1}{u_0^2a^2}(U_\rho(x)U_\mu(x+a\hat{\rho})U^\dagger_\rho(x+a\hat{\mu}) - 2u_0^2U_\mu(x) \quad (2.50)$$
$$+U^\dagger_\rho(x-a\hat{\rho})U_\mu(x-a\hat{\rho})U_\rho(x-a\hat{\rho}+a\hat{\mu}))$$

The the complicated improvements necessary to arrive at the Asqtad action are relatively cheap to implement computationally, and this action is currently the most efficient action available for the simulation of light quarks. It is formally $\mathcal{O}(a^4, \alpha_s a^2)$ improved.

2.4 Correlation Functions and Parameter Extraction

Many physical (Minkowski space) results can be straightforwardly extracted from the Euclidean lattice. This is because we calculate time independent quantities which are equivalent up to a phase in Euclidean space and Minkowski space. To see how Minkowski results are extracted from a Euclidean field theory consider the two-point correlator in Euclidean space

$$C(t,p) = \int d^3x e^{-ipx}\langle 0|T\left[\phi(x,t)\phi(0,0)\right]|0\rangle = \quad (2.51)$$
$$\int d^3x e^{-ipx}\langle 0|\phi e^{-Ht+iKx}\phi|0\rangle$$

where $t > 0$, H is the hamiltonian and K is the momentum operator. Now insert a complete set of states between the Heisenberg operators, ϕ,

$$C(t,p) = \int d^3x \int d^3k e^{-ipx}\sum_\lambda \frac{\langle 0|\phi e^{-Ht+iKx}|\lambda_k\rangle\langle\lambda_k|\phi|0\rangle}{2E_k} = \quad (2.52)$$
$$\sum_\lambda \int d^3k\delta^3(k-p)\frac{\langle 0|\phi|\lambda_k\rangle\langle\lambda_k|\phi|0\rangle}{2E_k}e^{-E_kt} = \sum_\lambda \frac{\langle 0|\phi|\lambda_p\rangle\langle\lambda_p|\phi|0\rangle}{2E_p}e^{-E_pt}$$

It is clear from the above relation that by considering the limit $t \to \infty$ that the ground state will be projected out

$$C(t,p) \to_{lim\, t\to\infty} \frac{\langle 0|\phi|\Omega_p\rangle\langle\Omega_p|\phi|0\rangle}{2E_p} e^{-E_p t} \tag{2.53}$$

where Ω is the ground state that has overlap with ϕ. In this way Euclidean theory ground state amplitudes and energies can be extracted: they are equivalent to the corresponding quantities in the Minkowski theory. Ground state parameters from arbitrary N-pt correlation functions can be determined.

Whether the correlation function is odd in time or momentum, and whether the signal is in the real or imaginary part can be determined by considering the discrete symmetries: time reversal $\mathcal{T}$, parity $\mathcal{P}$, and the combined charge-conjugate parity hermiticity $\mathcal{CPH}$:

$$\begin{aligned} &\mathcal{P} : \psi(x,t) \to \gamma_4\psi(-x,t) \\ &\mathcal{T} : \psi(x,t) \to \gamma_4\gamma_5\psi(x,-t) \\ &\mathcal{CPH} : \psi(x,t) \to \gamma_5\gamma_4 C^{-1}\psi(x,t) \end{aligned} \tag{2.54}$$

where C^{-1} is the charge conjugation operator.

2.5 Heavy-Light Four-quark Operators: B Mixing

Now that the lattice methods relative to this calculation have been detailed it is useful to describe the specific implementation of them in our calculation of the B mixing hadronic matrix element. In fact these methods should be applicable to the analysis of any heavy-light four-quark operator. First the effects of the doubler modes on the four-quark operator are explored. This determines the form the three-point correlation function takes. Then the setup of the calculation and correlation functions needed are described, showing how a fourier transformed combination of propagators can be stored so that they can be used to build any four-quark operator. Finally the Fermilab interpretation is used to remove the $\mathcal{O}(a\vec{p})$ errors from the operator.

We show the basic set-up of the calculation in Fig. (2.1). The four-quark operator to be determined, Q, is placed at the origin, with the $\bar{B}$ and B mesons at points x and y. By setting it up in this way, only one heavy and one light quark inversion are needed. After fourier transforming the spatial components of the correlator a two-dimensional (in t_x and t_y) correlation function can be made by "tying" together the propagators in the appropriate fashion.

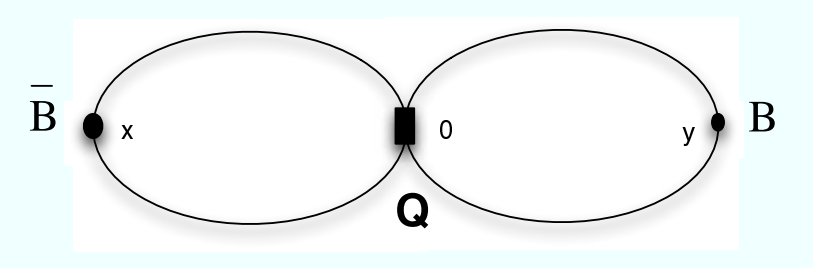

Figure 2.1: The set-up of the four-quark operator calculation is shown above. The operator Q is fixed at the origin, and the $\bar{B}$ and B interpolating fields varied over x and y.

2.5.1 Doubler Modes' Effect on the Form of the Correlation Functions

This section's discussion is a straightforward generalization of Ref. [42]'s analysis of doublers in bilinears to the case of four-quark operators. Throughout the rest of the chapter the heavy-quark field is referred to by b and the light-quark field by s.

Because of the doubling symmetry of the naive light quark,

$$\psi(x) \to e^{ix\cdot\pi_g} M_g \psi(x) \qquad \bar{\psi}(x) \to e^{ix\cdot\pi_g} \bar{\psi}(x) M_g^\dagger \tag{2.55}$$

where

$$\begin{aligned} M_g &= \prod_{\mu\in g} M_\mu \\ M_\mu &= i\gamma_5\gamma_\mu \end{aligned} \tag{2.56}$$

and

$$G = \{g : g = (\mu_1, \mu_2, \ldots), \mu_1 < \mu_2 < \ldots\}$$

$$(\pi_g)_\mu = \begin{cases} \frac{\pi}{a} & \text{if } \mu \in g \\ 0 & \text{otherwise,} \end{cases}$$

the 3-pt correlation function will have undesired oscillating terms contributing to it. Consider the 3-pt function in spatial momentum space:

$$\sum_{\vec{x},\vec{y}} \langle 0|\bar{b}(x)\gamma_5 s(x)\,[\bar{s}(0)\Gamma b(0)\bar{s}(0)\Gamma b(0)]\,\bar{b}(y)\gamma_5 s(y)|0\rangle =$$

$$\int_{-\pi/a}^{\pi/a} \frac{d^3\vec{p}}{(2\pi)^3}\frac{d^3\vec{k}}{(2\pi)^3} \langle 0|\tilde{\bar{b}}(\vec{p},t_x)\gamma_5\tilde{s}(\vec{p},t_x)\,[\bar{s}(0)\Gamma b(0)\bar{s}(0)\Gamma b(0)]\,\tilde{\bar{b}}(\vec{k},t_y)\gamma_5\tilde{s}(\vec{k},t_y)|0\rangle \tag{2.57}$$

where for now the bracketed 4-quark operator is left in position space and $\tilde{b}, \tilde{s}$ are the spatial momentum space fermion fields. Because of the doubling symmetry we can just integrate over the central half of the brilloun zone and sum over the

spatial doublers

$$\sum_{g_s,g_s'}\int_{-\pi/2a}^{\pi/2a}\frac{d^3\vec{p}}{(2\pi)^3}\frac{d^3\vec{k}}{(2\pi)^3}\langle 0|\bar{\tilde{b}}(\vec{p}+\Pi_{g_s},t_x)\gamma_5\tilde{s}(\vec{p}+\Pi_{g_s},t_x)\,[\bar{s}(0)\Gamma b(0)\bar{s}(0)\Gamma b(0)]\times$$
$$\bar{\tilde{b}}(\vec{k}+\Pi_{g_s'},t_y)\gamma_5\tilde{s}(\vec{k}+\Pi_{g_s'},t_y)|0\rangle, \tag{2.58}$$

where g_s denotes a particular spatial doubler mode. Because of the high momentum that will be imparted to the heavy quark when $g_s \neq \emptyset$, this state will be far off-shell and have a negligable effect on the correlation function. The taste of the temporal modes can now be considered by fourier transforming the light quarks' temporal component, and then again restricting the brilloun zone and summing over the doubler:

$$\begin{aligned}&\int_{-\pi/2a}^{\pi/2a}\frac{d^3\vec{p}}{(2\pi)^3}\frac{d^3\vec{k}}{(2\pi)^3}\int_{-\pi/2a}^{\pi/2a}\frac{dp_0}{(2\pi)}\frac{dk_0}{(2\pi)}e^{ip_0t_x+ik_0t_y} \\ &\times\langle 0|\bar{\tilde{b}}(\vec{p},t_x)\gamma_5\left[\tilde{s'}(\vec{p},p_0)+(-1)^{(t_x)}\tilde{s'}(\vec{p},p_0+\pi/a)\right] \\ &\times[\bar{s}(0)\Gamma b(0)\bar{s}(0)\Gamma b(0)]\,\bar{\tilde{b}}(\vec{k},t_y)\gamma_5\left[\tilde{s'}(\vec{k},k_0)+(-1)^{(t_y)}\tilde{s'}(\vec{k},k_0+\pi/a)\right]|0\rangle.\end{aligned} \tag{2.59}$$

Using the relation

$$\tilde{q'}^g(p)=\Pi_{\mu\in g}i\gamma_5\gamma_\mu\tilde{s'}(p+\pi_g) \tag{2.60}$$

so that

$$\tilde{s'}(\vec{p},p_0)=\tilde{q'}(\vec{p},p_0),\quad \tilde{s'}(\vec{p},p_0+\pi/a)=i\gamma_5\gamma_0\tilde{q'}^0(\vec{p},p_0), \tag{2.61}$$

allows the 3-pt function to be written as

$$\begin{aligned}&\int_{-\pi/2a}^{\pi/2a}\frac{d^3\vec{p}}{(2\pi)^3}\frac{d^3\vec{k}}{(2\pi)^3}\langle 0|\bar{\tilde{b}}(\vec{p},t_x)\gamma_5\left[\tilde{q}(\vec{p},t_x)+(-1)^{(t_x)}i\gamma_5\gamma_0\tilde{q}^0(\vec{p},t_x)\right] \\ &\times[\bar{s}(0)\Gamma b(0)\bar{s}(0)\Gamma b(0)]\,\bar{\tilde{b}}(\vec{k},t_y)\gamma_5\left[\tilde{q}(\vec{k},t_y)+(-1)^{(t_y)}i\gamma_5\gamma_0\tilde{q}^0(\vec{k},t_y)\right]|0\rangle,\end{aligned} \tag{2.62}$$

where the superscript 0 indicates a temporal taste and no superscript is the null taste at the center of the brilloun zone.

After fourier transforming, the bracketed 4-quark operator has no restrictions on the tastes that contribute to it. However, it must be contracted with the external quark fields to form the propagators. Because the Asqtad action is used, contractions between tastes of different types are supressed to $\mathcal{O}(a^2\alpha_s)$.

This results in the following form of the 3-pt function

$$\int_{-\pi/2a}^{\pi/2a} \frac{d^3\vec{p}}{(2\pi)^3}\frac{d^3\vec{k}}{(2\pi)^3}\langle 0|\bar{b}(\vec{p},t_x)\gamma_5\left[q(\vec{p},t_x)+(-1)^{(t_x)}i\gamma_5\gamma_0 q^0(\vec{p},t_x)\right] \\ \times\left[\left(\bar{q}(0)+i\gamma_5\gamma_0\bar{q}^0(0)\right)\Gamma b(0)\left(\bar{q}(0)+i\gamma_5\gamma_0\bar{q}^0(0)\right)\Gamma b(0)\right]\bar{b}(\vec{k},t_y)\gamma_5 \quad (2.63) \\ \times\left[q(\vec{k},t_y)+(-1)^{(t_y)}i\gamma_5\gamma_0 q^0(\vec{k},t_y)\right]|0\rangle,$$

where contractions between quarks of different tastes are suppressed to the order we are working.

2.5.2 The Wick Contractions→Open Propagators and Correlation Functions

We perform the Wick contractions of the matrix elements of general three and two-point functions to arrive at the traces used in our numerical calculations. We then show how these can be decomposed into what we refer to as the open-meson propagator.

General Two-point Correlator

We start with the matrix element

$$\langle 0|\bar{b}(x)\Gamma_1 s(x)\bar{s}(0)\Gamma_2 b(0)|0\rangle \quad (2.64)$$

and perform the wick contraction to get

$$\langle 0|\mathrm{tr}\left[\Gamma_1 N_s(x,0)\Gamma_2 H_b(0,x)\right]|0\rangle = \langle 0|\mathrm{tr}\left[\Gamma_1 N_s(x,0)\Gamma_2\gamma_5 H_b^\dagger(x,0)\gamma_5\right]|0\rangle, \quad (2.65)$$

where N_s is the naive s quark propagator and H_b is the heavy b quark propagator. The hermiticity symmetry, $H(x,0)=\gamma_5 H(0,x)^\dagger\gamma_5$, has been used. For concreteness consider the decay constant two-point function, where $\Gamma_1=\gamma_0\gamma_5$ and $\Gamma_2=\gamma_5$, so that

$$\langle 0|\bar{b}(x)\Gamma_1 s(x)\bar{s}(0)\Gamma_2 b(0)|0\rangle \rightarrow \quad (2.66) \\ \langle 0|\mathrm{tr}\left[\gamma_0\gamma_5 N_s(x,0)H_b^\dagger(x,0)\gamma_5\right]|0\rangle.$$

After fourier transforming the spatial components (sum over all $\vec{x}$ at 0 momentum) and inserting a complete set of states we have

$$C(t) = \langle 0|\mathrm{tr}\left[A_0\gamma_5 N_s(t_x,0)H_b^\dagger(t_x,0)\gamma_5\right]|0\rangle \quad (2.67) \\ = \sum_n \frac{\langle 0|\bar{b}\gamma_0\gamma_5 s|n\rangle\langle n|\bar{s}\gamma_5 b|0\rangle}{2m_n}e^{-m_n t}.$$

The interpolating field, $\bar{s}\gamma_5 b$, will couple to whatever states have the same quantum numbers, in this case $J^{PC}=0^{-+}$, and it is a pseudoscalar. In the large t

limit we obtain

$$C(t) =_{t\to\infty} \frac{ZA_0}{2m_B} 2e^{-m_B t_x}, \tag{2.68}$$

where $Z = \langle B|\bar{s}\gamma_5 b\rangle$ and $A_0 = \langle 0|\bar{b}\gamma_0\gamma_5|B\rangle = f_B m_B$. The amplitude A_0 is the decay constant for the pseudo-scalar meson B of mass m_B.

In practice the relatively small object, $D_{ij}^{ab} = N_{s,ik}^{ac}(t_x,0)H_{b,jk}^{*dc}(t_x,0)\gamma_5^{db}$, is first created, where the upper indices are Dirac and the lower are color. This object is saved and then tied together with $\gamma_0\gamma_5$. This object is what we refer to as the open-meson propagator.

The analysis of the doublers' effects is entirely analogous to the four-quark operator, and causes each term in the sum over states to appear as a pair of states

$$C(t) = \sum_n \left[\frac{\langle 0|\bar{b}\gamma_0\gamma_5 s|n\rangle\langle n|\bar{s}\gamma_5 b|0\rangle}{2m_n} e^{-m_n t} - (-1)^t \frac{\langle 0|\bar{b}s|n\rangle\langle n|\bar{s}\gamma_0 b|0\rangle}{2m_n} e^{-m_n t} \right] \tag{2.69}$$

where the first term in the pair couples to states of negative parity, $P = -1$, and the second, oscillating term couples to states of positive parity, $P = +1$. Because the positive parity state oscillates in Euclidean time it is straightforward to separate such doubler states from the desired non-oscillating states.

General Three-point Correlator

Starting with a generalized version of the matrix element that arises in $B - \bar{B}$ mixing

$$C_3(t) = \sum_{\vec{x}} \langle 0|\bar{b}(x)\gamma_5 s(x)\bar{s}(0)\Gamma_1 b(0)\bar{s}(0)\Gamma_2 b(0)\bar{b}(y)\gamma_5 s(y)|0\rangle \tag{2.70}$$

and performing the four possible wick contractions we get

$$\begin{aligned}
C_3(t_x,t_y) &= \sum_{\vec{x},\vec{y}} \mathrm{tr}\left[\gamma_5 N_s(x,0)\Gamma_1 H_b(0,x)\right]\mathrm{tr}\left[\gamma_5 N_s(y,0)\Gamma_2 H_b(0,y)\right] \\
&+\mathrm{tr}\left[\gamma_5 N_s(y,0)\Gamma_1 H_b(0,y)\right]\mathrm{tr}\left[\gamma_5 N_s(x,0)\Gamma_2 H_b(0,x)\right] \\
&+\mathrm{tr}\left[\gamma_5 N_s(x,0)\Gamma_1 H_b(0,y)\gamma_5 N_s(y,0)\Gamma_2 H_b(0,x)\right] \\
&+\mathrm{tr}\left[\gamma_5 N_s(x,0)\Gamma_2 H_b(0,y)\gamma_5 N_s(y,0)\Gamma_1 H_b(0,x)\right] \\
&= \sum_{\vec{x},\vec{y}} \mathrm{tr}\left[N_s(x,0)\Gamma_1\gamma_5 H_b^\dagger(x,0)\right]\mathrm{tr}\left[N_s(y,0)\Gamma_2\gamma_5 H_b^\dagger(y,0)\right] \\
&+\mathrm{tr}\left[N_s(y,0)\Gamma_1\gamma_5 H_b^\dagger(y,0)\right]\mathrm{tr}\left[N_s(x,0)\Gamma_2\gamma_5 H_b^\dagger(x,0)\right] \\
&+\mathrm{tr}\left[N_s(x,0)\Gamma_1\gamma_5 H_b^\dagger(y,0)N_s(y,0)\Gamma_2\gamma_5 H_b^\dagger(x,0)\right] \\
&+\mathrm{tr}\left[N_s(x,0)\Gamma_2\gamma_5 H_b^\dagger(y,0)N_s(y,0)\Gamma_1\gamma_5 H_b^\dagger(x,0)\right].
\end{aligned} \tag{2.71}$$

In practice, the object $E^{ab}_{ij}(t_x) = \gamma_5^{ac} H^{*dc}_{b,ki}(t_x,0) N^{db}_{s,kj}(t_x,0)$ is made and saved, and the above traces formed using it:

$$\begin{aligned} &\Gamma_1^{ba} E^{ab}_{ii}(t_x) \Gamma_2^{dc} E^{cd}_{jj}(t_y) + \Gamma_1^{ba} E^{ab}_{ii}(t_y) \Gamma_2^{dc} E^{cd}_{jj}(t_x) \\ &+\Gamma_1^{ba} E^{ac}_{ij}(t_x) \Gamma_2^{cd} E^{db}_{ji}(t_y) + \Gamma_1^{ba} E^{ac}_{ij}(t_y) \Gamma_2^{cd} E^{db}_{ji}(t_x). \end{aligned} \tag{2.72}$$

There are 24 possible heavy-light 4-quark operators which obey the symmetries of lattice QCD or could arise in extensions to the Standard Model. These are 12 color singlets and 12 more with the same gamma structures as the color singlets, but the color indices switched, i.e.

$$\begin{aligned} &\bar{s}_i(x)(1-\gamma_5) b_i(x) \bar{s}_j(x)(1-\gamma_5) b_j(x) \quad \text{vs.} \\ &\bar{s}_i(x)(1-\gamma_5) b_j(x) \bar{s}_j(x)(1-\gamma_5) b_i(x) \end{aligned} \tag{2.73}$$

where i and j are color indices. These 24 operators can all be constructed from the same open propagator in a very short amount of time on a single processor, <1 min.

As an example consider the first term in Eq. (2.72) with the color indices the same

$$\begin{aligned} &\langle 0 | \bar{b}_m(x) \gamma_5 s_m(x) \bar{s}_i(0) \Gamma_1 b_i(0) \bar{s}_j(0) \Gamma_2 b_j(0) \bar{b}_n(y) \gamma_5 s_n(y) | 0 \rangle \\ &\qquad = \Gamma_1^{ba} E^{ab}_{ii}(t_x) \Gamma_2^{dc} E^{cd}_{jj}(t_y) + \cdots \end{aligned} \tag{2.74}$$

and the same term with the color indices switched

$$\begin{aligned} &\langle 0 | \bar{b}_m(x) \gamma_5 s_m(x) \bar{s}_i(0) \Gamma_1 b_j(0) \bar{s}_j(0) \Gamma_2 b_i(0) \bar{b}_n(y) \gamma_5 s_n(y) | 0 \rangle \\ &\qquad = \Gamma_1^{ba} E^{ab}_{ij}(t_x) \Gamma_2^{dc} E^{cd}_{ji}(t_y) + \cdots \end{aligned} \tag{2.75}$$

It can be seen above that because the color indices are left open in the open propagator that the same one can be used for the color singlet and the color mixed by appropriately tying them together.

It is straightforward to show that as $t_x, -t_y \to \infty$ the correlator takes the

form

$$\sum_{\vec{x},\vec{y}} \langle 0|\bar{b}(x)\gamma_5 s(x)\left[\bar{s}(0)\Gamma b(0)\bar{s}(0)\Gamma b(0)\right]\bar{b}(y)\gamma_5 s(y)|0\rangle \rightarrow \tag{2.76}$$
$$\frac{e^{-E_{0^-}(t_x-t_y)}}{2E_{0^-}2E_{0^-}}\langle 0|\bar{b}(0)\gamma_5 s(0)|0^-\rangle\langle 0^-|\bar{b}(0)\gamma_5 s(0)|0\rangle\langle 0^-|\bar{s}(0)\Gamma b(0)\bar{s}(0)\Gamma b(0)|0^-\rangle$$
$$-(-1)^{t_x}\frac{e^{-E_{0^+}t_x+E_{0^-}t_y}}{2E_{0^+}2E_{0^-}}\langle 0|\bar{b}(0)i\gamma_0 s(0)|0^+\rangle\langle 0^+|\bar{s}(0)i\gamma_5\gamma_0\Gamma b(0)\bar{s}(0)\Gamma b(0)|0^-\rangle$$
$$\times\langle 0^-|\bar{b}(0)\gamma_5 s(0)|0\rangle$$
$$-(-1)^{t_y}\frac{e^{-E_{0^-}t_x+E_{0^+}t_y}}{2E_{0^+}2E_{0^-}}\langle 0|\bar{b}(0)\gamma_5 s(0)|0^-\rangle\langle 0^-|\bar{s}(0)\Gamma b(0)\bar{s}(0)i\gamma_5\gamma_0\Gamma b(0)|0^+\rangle$$
$$\times\langle 0^+|\bar{b}(0)i\gamma_0 s(0)|0\rangle$$
$$+(-1)^{t_x+t_y}\frac{e^{-E_{0^+}(t_x-t_y)}}{2E_{0^+}2E_{0^+}}\langle 0|\bar{b}(0)i\gamma_0 s(0)|0^+\rangle\langle 0^+|\bar{b}(0)i\gamma_0 s(0)|0\rangle$$
$$\times\langle 0^+|\bar{s}(0)i\gamma_5\gamma_0\Gamma b(0)\bar{s}(0)i\gamma_5\gamma_0\Gamma b(0)|0^+\rangle$$

The negative parity ground states are labeled 0^- and the positive 0^+. The higher energy states drop off more quickly in Euclidean time than the pseusoscalar states. These unwanted higher energy contributions are able to be "fitted" out, and the desired matrix element, which is proportional to the ground state amplitude, can be extracted.

2.5.3 Improving the Heavy-Light Four-Quark Operator

The B mixing operator has disretization errors starting at $\mathcal{O}(a\vec{p})$, due to the difference in the lattice heavy quarks' and continuum heavy quarks' small momentum behavior. To see this consider the small $a\vec{p}$ expansion of the heavy lattice spinor,

$$u^{lat}(\xi,\mathbf{p}) = \frac{\gamma_0 \text{sign}\xi \sinh Ea - i\gamma_j \sin(\mathbf{p}_j a) + 1 + m_0 a + \frac{1}{2}\hat{\mathbf{p}}^2 a^2 - \cos p_0 a}{\sqrt{2L(L+\sinh Ea)}} u(\xi,0) \tag{2.77}$$
$$= e^{-M_1 a/2}\left[1 - \frac{i\gamma\cdot\mathbf{pa}}{2\sinh M_1 a} + \mathcal{O}((a\mathbf{p})^2)\right]u(\xi,0)$$

where $\hat{p_i} = \frac{2}{a}\sin(\frac{p_i a}{2})$ and $L = 1+m_0 a+\frac{1}{2}\hat{\mathbf{p}}^2 a^2 - \cos p_0 a$, and ξ refers to the solution we are considering (particle/antiparticle, spin up/spin down), and that of the continuum spinor

$$u^{cont}(\xi,\mathbf{p}) = \left[1 - \frac{i\gamma\cdot\mathbf{p}}{2m} + \mathcal{O}((a\mathbf{p})^2)\right]u(\xi,0). \tag{2.78}$$

The lattice normalization factor, $Z = e^{-M_1 a/2}$, and mismatch between the small momentum terms can be easily removed by "rotating" the lattice heavy quark at was done to heavy-light bilinear operators in Ref. [15]. The naive lattice spinors have the same small momentum behavior as the continuum case and need not be matched.

Consider one of the terms in the contraction of the lattice operator

$$\langle s(p_s'), b(p_b')|\bar{s}\Gamma b\bar{s}\Gamma b|s(p_s), b(p_b)\rangle_{lattice} = \tag{2.79}$$
$$N_s(p_s')N_s(p_s)N_b(p_b')N_b(p_b)\bar{u}_{lat}(p_s')\Gamma u_{lat}(p_b')\bar{u}_{lat}(p_s)\Gamma u_{lat}(p_b)$$
$$+(other\, contractions),$$

where $N_s(p)$ and $N_b(p)$ are normalization factors that are can be set to Z at the

order we are working. Following the Symanzik procedure we demand the lattice and continuum match at $\mathcal{O}(a\mathbf{p})$,

$$\begin{aligned} Z(\bar{u}(\xi,0)[1-\frac{i\gamma\cdot\mathbf{p'_s}}{2m_s}]\Gamma e^{-M_1^b a/2}[1-\frac{i\gamma\cdot\mathbf{p'_b}a}{2\sinh M_1^b a}]u(\xi,0) \\ \times\bar{u}(\xi,0)[1-\frac{i\gamma\cdot\mathbf{p_s}}{2m_s}]\Gamma e^{-M_1^b a/2}[1-\frac{i\gamma\cdot\mathbf{p_b}a}{2\sinh M_1^b a}]u(\xi,0)) \\ +aZC_nO_n = \bar{u}(\xi,0)[1-\frac{i\gamma\cdot\mathbf{p'_s}}{2m_s}]\Gamma[1-\frac{i\gamma\cdot\mathbf{p'_b}}{2m_b}]u(\xi,0) \\ \times\bar{u}(\xi,0)[1-\frac{i\gamma\cdot\mathbf{p_s}}{2m_s}]\Gamma[1-\frac{i\gamma\cdot\mathbf{p_b}}{2m_b}]u(\xi,0)+O((\mathbf{p}a)^2), \end{aligned} \tag{2.80}$$

the dimension seven operators and coefficients, C_n and O_n, and appropriate normalization, are straightforward to identify (m_b must be identified with the Fermilab kinetic mass, M_2.)

The two operators, $\bar{s}\Gamma\gamma\cdot\mathbf{D}b\bar{s}\Gamma b$ and $\bar{s}\Gamma b\bar{s}\Gamma\gamma\cdot\mathbf{D}b$, after matching of the coefficients, will remove remove the $\mathbf{p}a$ discrepancy. After matching we have

$$C_1 = C_2 = [\frac{1}{\sinh M_1^b a} - \frac{1}{2M_2^b a}] \tag{2.81}$$

and

$$Z = e^{M_1^b a}. \tag{2.82}$$

However, adding these operators is the same effect, up to $\mathcal{O}(a\mathbf{p})$, as inducing the "rotation"

$$b'(x) = [1 + ad\gamma\cdot\mathbf{D}]b(x) \tag{2.83}$$

where

$$d = C_1 = C_2. \tag{2.84}$$

2.5.4 Naive Spinors

For completeness the improved naive spinors are shown

$$u(\xi,\mathbf{p}) = \frac{-i\gamma_\mu(\sin(p_\mu a)+\frac{1}{6}\sin^3(p_\mu a))+m_0 a}{\sqrt{2m_0 a(m_0 a+\sinh Ea)}}u(\xi,0). \tag{2.85}$$

The discretization errors in the naive spinors begin at $\mathcal{O}((a\mathbf{p})^3)$. Again ξ refers to which of the four solutions to the dirac equation you are considering.

2.6 Code Development

Due to the highly collaborative nature of lattice calculations of this type it is appropriate to point out which parts of the code were developed by the author.

The MILC ensembles with 2+1 flavors of sea quarks were generated before this report's calculation took place and they are publicly available. Details of the code used in the ensembles' generation can be found at `http://www.physics.utah.edu/detar/milc/`.

The author wrote the propagator creation and correlator calculation code using

libraries from the C++ based `FermiQCD` toolkit, developed my Massimo di Pierro [13]. `FermiQCD` provides the algorithms necessary to perform the sparse matrix inversions of the fermion actions. In this analysis the Biconjugate Gradient Method as described in Ref. [36] is used. `FermiQCD` also has convenient classes to represent the various field theoretic structures of the calculation: gauge configurations, spinors, gamma matrices, link variables, etc. It also provides easy to use classes that nearly automate the parallelization of the calculations.

The correlator and chiral fits codes were written by the author. The fitting codes incorporate a `Python` based code of Peter Lepage for non-linear least squares curve fitting. It provides an easy to use `Python` interface for the GSL's (GNU Scientific Library) Levenberg-Marquardt algorithm described in Ref. [36], modified so as to be able to perform Bayesian fits [24].

Excerpts of the correlator construction code and correlator fitting code are given in Appendix A.

Chapter 3

Correlator Fitting

In the following chapter we explain the fitting procedure we use to extract the $B_q^0 - \bar{B}_q^0$ mixing hadronic matrix element from the three-point correlator, where $q = d, s$. The mixing parameter $\beta_q = f_{B_q}\sqrt{M_{B_q} B_{B_q}}$ parametrizes the hadronic matrix element contributing to the B_q^0 system mass eigenstate difference

$$\Delta M_q = \frac{G_F^2 M_W^2}{16\pi^2}|V_{tb}^* V_{tq}|^2 \eta_B S_0(x_t) C(\mu_b) \langle \bar{B}_q | Q_q^1 | B_q \rangle(\mu_b) = \tag{3.1}$$
$$\frac{G_F^2 M_W^2}{16\pi^2}|V_{tb}^* V_{tq}|^2 \eta_B S_0(x_t) C(\mu_b) \frac{8}{3} M_{B_q}^2 f_{B_q}^2 B_{B_q}(\mu_b), \quad \mu_b = m_b,$$

where $Q_q^1 = \bar{b}\gamma_\mu(I-\gamma_5)q\bar{b}\gamma_\mu(I-\gamma_5)q = \frac{8}{3}M_{B_q}^2 f_{B_q}^2 B_{B_q}$. B_{B_q} in combination with a separate determination of f_{B_q} can also be used to calculate $\langle \bar{B}_q | Q_q^1 | B_q \rangle$.

A calculation of the B meson decay decay constants, f_B and f_{B_s}, is an ongoing project of the Fermilab Lattice and MILC collaborations, and a combination of separately calculated bag parameters and decay constants could possibly lead to results for the matrix elements with less uncertainty. At this stage of the analysis we consider the calculation of B_{B_q} as a secondary goal and don't attempt to quantify its systematic errors as fully as for $\langle \bar{B}_q | Q_q^1 | B_q \rangle$, using it just as a consistency check. The scalar-psuedoscalar, $S-P$, four-quark matrix element with the operator $Q_q^2 = \bar{b}(I-\gamma_5)q\bar{b}(I-\gamma_5)q = \frac{5}{3}M_{B_q}^2 f_{B_q}^2 B_{B_q}^S$, is also needed for the continuum to lattice matching calculation at one-loop that will be discussed in Chapter 4. Results for this matrix element are also presented here. The following methods should work in general for all heavy-light four-quark operators when the operator, Q_q^i, is placed at the origin. This is significant because additional operators can contribute to B^0 mixing in extensions to the Standard Model.

We obtain Q_q^1 from the zero momentum three-point correlation function

$$C_{Q_q^1}(t_1, t_2) = \sum_{\vec{x_1}, \vec{x_2}} \langle \bar{B}_q(t_1, \vec{x_1}) | Q_q^1(0) | B_q(t_2, \vec{x_2}) \rangle. \tag{3.2}$$

The correlation function has the following form after inserting a complete set of states,

$$C_{Q_q^1}(t_1, t_2) = \sum_{i,j} ((-1)^{t_1+1})^i ((-1)^{t_2+1})^j \frac{Z_i Z_j O_{ij}}{(2E_i)(2E_j)} e^{-E_i t_1 - E_j t_2}, \tag{3.3}$$

where $O_{00} = \langle \bar{B}_q | Q_q^1 | B_q \rangle$, and the oscillations in time are due to the naive light valence quarks. In order to isolate β_q the three-point function can be simultaneously fit with

the zero momentum, pseudoscalar B_q^0 meson propagator

$$C_{PS}(t) = \sum_{\vec{x}} \langle B_q(t,\vec{x}) | \bar{q}(0)\gamma_5 b(0) \rangle = \sum_i ((-1)^{t+1})^i \frac{|Z_i|^2}{2E_i} e^{-E_i t}. \tag{3.4}$$

To extract B_{B_q} the B_q^0 decay constant, or axial-vector, two-point function must be calculated and simultaneously fit to,

$$C_{A_4}(t) = \sum_{\vec{x}} \langle B_q(t,\vec{x}) | \bar{q}\gamma_4\gamma_5 b(0) \rangle = \sum_i ((-1)^{t+1})^i \frac{A_{4,i} Z_i}{2E_i} e^{-E_i t}, \tag{3.5}$$

where $A_{4,0} = f_{B_q} M_{B_q}$.

We construct the correlation functions using improved naive propagators for the light valence quarks, and clover propagators with the Fermilab interpretation for the heavy quarks [15][27]. Practically the light quark propagators are calculated using Asqtad fermions, which are then converted to improved naive fermions before the correlator is constructed. This approach saves computational time (Asqtad quarks have 1/4 the degrees of freedom naive quarks do) but allows the correlation functions to retain their dirac structure.

The mixing operator is placed at the origin, and the $\bar{B}_q$ and B_q mesons at positions x_1 and x_2. This set up allows the fits to be done two dimensionally, and makes the incorporation of the open-propagator method straightforward. As explained in Chapter 2 the heavy-quark is rotated at the source. This removes $\mathcal{O}(\Lambda_{\rm QCD}/M)$ discretization errors in the operator. The heavy-quark is then either rotated at the sink or exponentially smeared using a 1S wavefunction. The additional rotation is to ensure the local-local meson correlator is positive-definite, and the 1S smearing greatly improves the overlap with the ground state. The naive quark propagator is local at source and sink. The correlation functions are calculated for four different time sources and then averaged over the time sources. The statistical errors in the data and fits were reduced with each additional time source, approximately by what is expected, $\sigma \rightarrow \approx \sigma/\sqrt{2}$, suggesting that the different time source correlators are weakly correlated and statistical power is gained by averaging.

3.1 Fitting Method

General Description of the Method

The model functions the data are fit to are highly non-linear as can be seen in Eqs. (3.3),(3.4), and (3.5). The algorithm used to perform the fit is a Leven-Marquardt minimization routine. The algorithm minimizes the χ^2 function

$$\chi^2 = \sum_{i,j} (f_i(\{p\}) - \bar{d}_i)\sigma_{ij}^{-1}(f_j(\{p\}) - \bar{d}_j). \tag{3.6}$$

The sum is over data points, in this case time slices. $f_i(\{p\})$ is the model function at time i with the set of parameters $p_n \in \{p\}$, which correspond to the amplitudes and energies in the correlator model functions. $\bar{d}_i$ is the average of data points d_i at time i, and σ_{ij}^{-1} is the inverse of the covariance matrix of the data. σ_{ij} is inverted using a singular value decomposition (SVD) algorithm, where eigenvalues below the (SVD cut)$\times$ (the largest eigenvalue) are set to zero to prevent the matrix from being singular

due to round-off error. Details of the SVD algorithm can be found in Ref. [36].

The correlators used to determine β_q and B_{B_q} on a particular ensemble and valence mass m_q are simultaneously fit to using a Bayesian fitting approach [24]. Bayesian fitting incorporates theoretical and experimental constraints into the fitting parameters, such as positive definiteness in amplitudes and increasing energies in the tower of states. In the same spirit it also uses priors and prior widths for the parameters in the fit. The priors for the ground state meson mass are set by examining effective mass plots. The priors and prior widths for the excited meson masses are set from experimental data such as contained in Ref. [43]. The priors and prior widths for the amplitudes are set based on physical assumptions: we expect excited state amplitudes to be of similar order or less to the ground state amplitude. This allows parameters that cannot be well determined from the data to be included in the model function and still obtain good fits, i.e. fits are biased to stay in physical regions of parameter space even with undetermined parameters that, unconstrained, might acquire highly non-physical values.

The basic fitting method is to include additional terms in the χ^2 function to get an augmented χ^2 function, $\chi^2_{aug} = \chi^2 + \chi^2_{priors}$

$$\chi^2_{aug} = \sum_{i,j}(f_i(\{p\}) - d_i)\sigma_{ij}^{-1}(f_j(\{p\}) - d_j) + \sum_{p_n}\frac{(p_n - \hat{p}_n)^2}{\sigma_n^2} \tag{3.7}$$

and $\hat{p}_n$ and σ_n are the prior and prior width of parameter p_n. The augmenting priors cause the χ^2_{aug} to increase if the fit parameters stray too far outside of their widths, biasing but not forcing the parameters to stay within the width ranges. Of course, an indication of bad prior and prior width choices is if good χ^2s cannot be obtained, or if the parameters' central values obtained from the fit are outside of the prior width.

Numerical Considerations

A numerical "trick" that helps prevent roundoff error in the covariance matrix inversion is to first normalize the elements of the matrix by the diagonal elements

$$\hat{\sigma}_{ij} = \frac{\sigma_{ij}}{\sigma_{ii}\sigma_{jj}}, \tag{3.8}$$

which is a consistent alteration if the model function and data are similarly scaled

$$\begin{aligned}\hat{f}_i(\{p\} &= \frac{f_i(\{p\})}{\sigma_{ii}} \\ \hat{d}_i &= \frac{d_i}{\sigma_{ii}}.\end{aligned} \tag{3.9}$$

This protects against the round-off error that the SVD cut controls, and because more eigenvalues can be kept more information is left in the covariance matrix. This is particularly important when simultaneously fitting to separate correlators, because the variances of the data points in some correlators are much larger than in others, and much of the information from the noisier correlator might be lost in the SVD cut if they are not scaled to have eigenvalues of similar order.

Another concern is the size of the covariance matrix versus the number of samples or in our case configurations. The dimensions of the covariance matrix are the same as the number of time slices included in the fits, $N_{data} \times N_{data}$. If the covariance

matrix is too large compared to the number of samples it is not well "resolved". The standard rule of thumb is that N_{data} should not exceed $\sqrt{N_{samples}}$, where $N_{samples}$ is the number of samples d_i used in the fit. The size of the covariance matrices used in our fits are too large according to the standard rule, $\sqrt{N_{samples}} \sim 25$ and $N_{data} \sim 60$. If the 4 time sources used to average each correlator are considered $\sqrt{N_{samples}} \sim 50$. This is approaching the samples needed according to the rough estimate above and the quality of the correlation matrix needs to be checked. The straight forward way to do this is check that there is a range of time slices where the fit results are stable, which we have done. In all case we can vary the three-point time ranges from at least $t_1, t_2 = 2-6 \rightarrow 2-12$ and use $t_1, t_2 = 2-8$ in the central fits. The two-point functions are stable at least from $t = 2-10 \rightarrow 2-25$.

Statistical Considerations and Boostrapping

The error estimation is done using the standard bootstrap method. For these fits 500 bootstrap ensembles are constructed from the original ensemble by sampling with replacement. The extent to which the distribution is gaussian can be tested in this way by examining the upper and lower error bars in the fits. The correlations between the fit parameters are also properly accounted for which is important if a final result is needed that is a combination of fit parameters. It was demonstrated recently by Doug Toussaint of the MILC collaboration that in practice the covariance matrix should be remade for each bootstrap ensemble in order to prevent underestimation of the statistical errors. The specific reasons behind this are not yet known, however this procedure is what we use in our fits.

The different configurations are autocorrelated so it is also useful to bin the data to reduce the correlations. Binning is done to the original ensemble, where for example

$$d_i'^k = \frac{d_i^k + d_i^{k+1} + d_i^{k+2} + d_i^{k+3}}{4}, \tag{3.10}$$

where k number the sample and $d_i'^k$ is the new sample k data point at time i. For the following fits it was seen that binning the data by four is optimal.

In addition, according to Ref. [24] it is proper to choose the priors for each bootstrap sample based on sampling from a Gaussian distribution with the prior value the mean and the prior width the standard deviation. In practice, if the widths are not too wide, this adjustment makes little difference in most fits.

Physical Constraints

At first Eq. (3.3) appears to imply that the number of fit parameters, O_{ij}, increases as N^2, where N=number of states. However, it is easy to show that $O_{mn} = O_{nm}$ for all m and n: For a real matrix element with external states M and N we have the identity

$$O_{mn} = \langle M|O|\bar{N}\rangle = (\langle M|O|\bar{N}\rangle)^\dagger = \langle \bar{N}|O^\dagger|M\rangle. \tag{3.11}$$

This identity holds because the matrix element is a real scalar, and

$$\langle \bar{N}|O^\dagger|M\rangle = \langle N|O|\bar{M}\rangle = O_{nm} \tag{3.12}$$

because of the CP invariance of QCD.

This reduces the number of O_{ij} parameters to $2N$. This constraint is valid for any other matrix elements of this form. Another straightforward constraint is using a parametrization that forces the tower of physical states to be increasing in energy,

$$E_{i+1} = E_i + e^{\Delta E_{i,i+1}}, \tag{3.13}$$

where $\Delta E_{i,i+1} = \log(E_{i+1} - E_i)$ is the fit parameter. Each physical state has unphysical oscillating partners because of the temporal doubler, and a separate constraint on these energies must be used

$$E^p_{i+1} = E^p_i + e^{\Delta E^p_{i,i+1}}. \tag{3.14}$$

It is also useful for the stability of the fits to implement the constraint that $E_0 < E^p_0$, which obviously holds in all cases: otherwise $i = 0$ would not be the ground state.

An additional constraint is the discrete time reversal symmetry ($\mathcal{T}$) of the correlators. C_{PS} is positive under reflections about the time axis

$$\begin{aligned} &C_{PS}(t) = \langle 0|\bar{q}(t)\gamma_5 b(t)\bar{b}(0)\gamma_5 q(0)|0\rangle \rightarrow_{\mathcal{T}} \\ &\langle 0|\bar{q}(-t)\gamma_5\gamma_4\gamma_5\gamma_4\gamma_5 b(-t)\bar{b}(0)\gamma_5\gamma_4\gamma_5\gamma_4\gamma_5 q(0)\rangle = +\langle 0|\bar{q}(-t)\gamma_5 b(-t)\bar{b}\gamma_5 s|0\rangle, \end{aligned} \tag{3.15}$$

C_{A_4} is negative

$$C_{A_4}(t) = \langle 0|\bar{q}(t)\gamma_5 b(t)\bar{b}(0)\gamma_4\gamma_5 q(0)|0\rangle \rightarrow_{\mathcal{T}} -\langle 0|\bar{q}(-t)\gamma_5 b(-t)\bar{b}\gamma_4\gamma_5 s|0\rangle, \tag{3.16}$$

and $C_{Q_{iq}}$ is positive under simultaneous reflection of both t_1 and t_2. It should be noted that while all four-quark operators will have a $\mathcal{T}$ symmetry, some will be negative under reflection. In practice this constraint is enforced by "folding" the correlators: the $+t$ and $-t$ slices are averaged appropriately.

3.2 Fits

We overview priors and present fit results for $\beta_q = f_{B_q}\sqrt{m_{B_q}B_{B_q}}$, $\beta^S_q = f_{B_q}\sqrt{m_{B_q}B^S_{B_q}}$, and B_{B_q} in this section.

Direct fits

The direct correlator fits are done to the raw correlators for the sea and valence masses shown in Table 3.1, with only time reflection averaging.

For the coarse and medium ensembles for $f_{B_q}\sqrt{m_{B_q}B_{B_q}}$ and $f_{B_q}\sqrt{m_{B_q}B^S_{B_q}}$ we found the smallest errors and largest stability using 3 correlators:

- C_{PS} local source/local sink
- C_{PS} local source/1S smeared sink
- $C_{Q^i_q}$ local source/ 1S smeared sink

and for the fine ensembles 2 correlators:

- C_{PS} 1S smeared source/1S smeared sink
- $C_{Q^i_q}$ local source/ 1S smeared sink.

$a(fm)$	Volume	m_L/m_h	N_{confs}	am_q
0.15	$16^3 \times 48$	0.2	631	0.0048, 0.007, 0.0097, 0.0194, 0.29,0.0484
0.15	$16^3 \times 48$	0.4	631	0.0048, 0.007, 0.0097, 0.0194, 0.29,0.0484
0.15	$16^3 \times 48$	0.6	440	0.0048, 0.007, 0.0097, 0.0194, 0.29,0.0484
0.12	$24^3 \times 64$	0.1	529	0.005, 0.007, 0.01, 0.02, 0.03, 0.0415
0.12	$20^3 \times 64$	0.14	833	0.005, 0.007, 0.01, 0.02, 0.03, 0.0415
0.12	$20^3 \times 64$	0.2	592	0.005, 0.007, 0.01, 0.02, 0.03, 0.0415
0.12	$20^3 \times 64$	0.4	460	0.005, 0.007, 0.01, 0.02, 0.03, 0.0415
0.09	$28^3 \times 96$	0.2	557	0.0031, 0.0044, 0.062, 0.0124, 0.0272, 0.031
0.09	$28^3 \times 96$	0.4	534	0.0031, 0.0042, 0.062, 0.0124, 0.0272, 0.031

Table 3.1: Ensembles on which two and three-point functions were calculated. Three different lattice spacings were used, with 6 different light valence quark masses, m_q, on each ensemble. The sea quark masses are labeled as m_L for the 2 degenerate light sea quarks and m_h for strange sea quark. All correlators were calculated at four different time sources and averaged over them.

All B_{B_q} fits were done using 2 correlators:

- C_{A_4} local source/1S smeared sink
- $C_{Q_q^i}$ local source/ 1S smeared sink.

ISA Fits

These fits attempt to reduce the oscillating states' contribution to the correlation functions as explained in Section 3.2.3. This method works poorly for extracting the mixing parameters because averaging noisier high time slice data with less noisy low time slice data prevents good determinations for the light valence mass data. The work done with it is mentioned here because it may be of more utility when correlators with smaller statistical errors are calculated.

For β_q the medium and coarse ensembles use a 2 correlator two-point fit

- C_{PS} local source/local sink
- C_{PS} local source/1S smeared sink .

and for the fine a 1 correlator two-point fit

- C_{PS} 1S smeared source/1S smeared sink .

to extract the ground state amplitude and mass, $|Z_0^{1S}|$ and m_0. The ISA is performed on

- $C_{Q_q^i}$ local source/1S smeared sink

and β_q is then extracted.

B_{B_q} is more straightforward, because the ratio $\frac{C_{Q_q^i}}{C_{A_4}C_{A_4}}$ approaches B_{B_q} as $t_1, t_2 \rightarrow \infty$, so no separate determination of $|Z_0^{1S}|$ and m_0 is necessary. The ISA is performed on the ratio of the 2 correlators

- C_{A_4} local source/1S smeared sink
- $C_{Q_{iq}}$ local source/1S smeared sink.

3.2.1 Direct Fit Details

Priors

The priors used for the direct fits are in Table (3.2). We obtained the ground state

Prior Values and Prior Widths		
Parameter	Prior Value	Width
Z_0^{1S}	2.2	0.5
Z_i^{1S}	0.01	0.5
Z_0^d	0.45	0.45
Z_i^d	0.01	1
A_0	0.3	0.3
A_i	0.5	0.5
O_{00}	0.01	0.02
O_{ij}	0.01	0.1
med coarse m_0	2.25	0.15
med coarse m_0^p	2.55	0.15
coarse m_0	1.95	0.15
coarse m_0^p	2.25	0.15
fine m_0	1.65	0.15
fine m_0^p	1.85	1.85
$\log \Delta E_{i+1,i}$	-1.5	0.5
$\log \Delta E_{i+1,i}^p$	-1.5	0.5

Table 3.2: The priors with index 0 refer to the ground state. Higher energy state priors have indices i and j. The superscript p indicates the first opposite parity excited state. These priors are used for the β_q fits. O_{00} is set to 0.3 for the B_{B_q} fits. These priors are used for the two-point correlator fits in the ISA as well. The ISA is a plateau fit, and the prior value is unconstrained.

start and prior values from plots of the data. We used effective mass plots to find the approximate ground state mass. For the overlap factors, Z_0, we examined the amplitude of the B meson propagator with the exponentials removed. We did the same for O_{00}, where the Z_0 amplitudes are accounted for.

For the higher states' overlap factors we simply gave start and prior values that were close to the ground state values, adjusting these values by small amounts to make sure they didn't affect the quality of the fits. The widths of these priors are larger than the ground state's in some cases because our only guide as to their magnitudes is that they should be of similar order to or less than the ground state's. The energy differences have priors and widths that allow them to vary from $\Delta E_{i+1,i} \approx 0.14 - 0.37$, where Ref. [43] has been used as a guide.

The same priors are used for all ensembles, with the exception of m_0 and m_0^p. These parameters govern the overall behavior of the correlators strongly, and are very different between lattice spacings so must be set with more care.

Time Slices and Number of States Used

The number of states and time slices we use in the direct fits are shown in Table 3.3. The fits are done simultaneously to all correlators listed for a particular ensemble and parameter.

β_q	Medium Coarse and Coarse	
Correlator	Number of States	Time Slice
C_{PS} (local/local)	3+3	2-15
C_{PS} (local/1S)	2+2	2-15
$C_{Q_q^i}$ (local/1S)	2+2	$2-8\times 2-8$

β_q	Fine	
Correlator	Number of States	Time Slice
C_{PS} (1S/1S)	2+2	2-20
$C_{Q_q^i}$ (local/1S)	2+2	$2-8\times 2-8$

B_{B_q}	Medium Coarse, Coarse, Fine	
Correlator	Number of States	Time Slice
C_{A_4} (d/1S)	2+2	2-20
$C_{Q_q^i}$ (local/1S)	2+2	$2-8\times 2-8$

Table 3.3: Number of states and time slices used for each correlator in the direct fits.

Following Ref. [24], the number of states are determined by first performing the fit using 1+1 states starting at high time slice, where the higher energy states are no longer contributing significantly and a good χ^2 per degree of freedom (dof) is obtained (≈ 1). The fit is then performed using one lower time slice as the starting time, and this is repeated until the $\chi^2/dof \gtrsim 1.5$. Then an additional pair of states is added to the model function, and the process repeated. Once the timeslice $t = 2$ can be included that number of states is used[2]. In order to check that this number of states is sufficient additional states are added, and the stability of the fit is examined. Examples of stability plots over numbers of states are shown in Figs. 3.2-3.4.

For the three-point function, we fit using $n_{states} = 4$, using timeslices $t_1 = t_2 = 2-8$ for all ensmbles. We have used up to 8 states in the three-point fits, but the central value for β_q does not change as shown in Fig. 3.2. The heavier valence mass B_{B_q} data has the same behavior as show in Figs. 3.3-3.4, however the lighter valence mass B_{B_q} data's errors increase significantly at 6 states, and a very conservative fit for B_{B_q} might call for 6 states for the lightest valence masses. We believe this behavior is due to the increase in statistical noise for these lighter mass data points, as opposed to a real physical effect though: 4 states is all that is necessary to get stable fits for the $f_B\sqrt{m_B}$ two-point function and β_q three-point function, therefore it seems unreasonable that a combined fit to the two functions requires more states. At this point, only 4 states were used in the B_{B_q} fits.

The two-point functions are usually fit from $t = 2-20$, with the number of states necessary depending on the smearing: the source and sink smeared two-point correlators only requires 4 states, while two-points with a delta source or sink also require 4, and those with both a delta source and delta sink require 6.

[2] $t = 0$ and $t = 1$ are noise, at $t = 0$ all states contribute because they have the same exponential weighting and $t = 1$ is contaminated by higher energy states because the staggering of the light quarks spreads their degrees of freedom over two time slices.

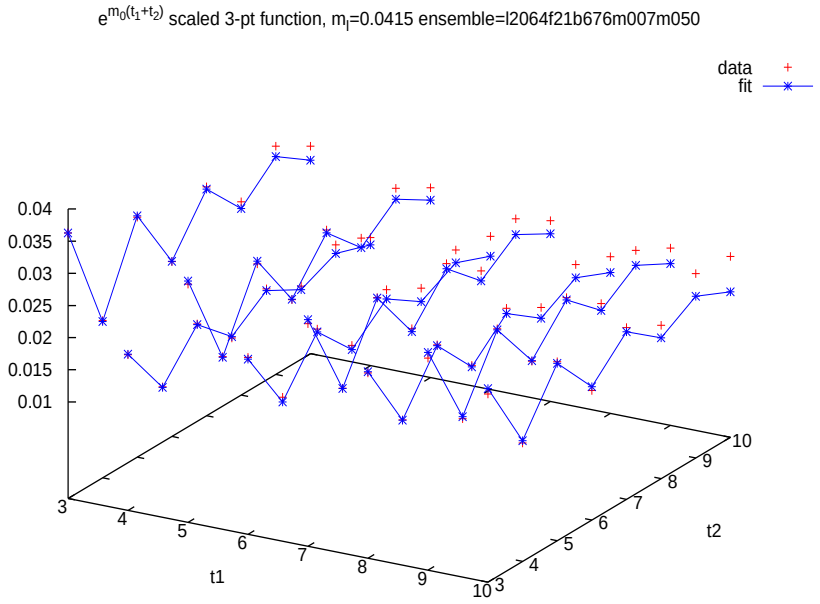

Figure 3.1: An example fit in 2 dimensions. The red crosses are the data points and the blue points and lines are the fit. Statistical errors are not shown because of the 2 dimensional nature of the plot, but grow rapidly in time.

3.2.2 Correlator Fit Results and Example Plots

We show the fit results for β_q, β_q^S and B_{B_q} in Table 3.4 and 3.5 and Table 3.6. There is no matching attempted between the bag parameters at this stage of the calculation so B_B^S is not needed.

Example fits are shown in Figs. 3.5-3.9, and to demonstrate the 2 dimensional nature of the fits an example plotted in 2 dimensions is shown in Fig. 3.1. Statistical error bars could not be included in the 2 dimensional plot. In the plots of the fit results, Figs. 3.10-3.11, it can be seen that $\beta_q = f_{B_q}\sqrt{M_{B_q}B_{B_q}}$ and $\beta_q^S = f_{B_q}\sqrt{M_{B_q}B_{B_q}^S}$ have a weak sea mass dependence, and a stronger valence mass dependence. In Fig. 3.12 it can be seen that in B_{B_q} the sea and valence mass dependence is very small in the fits with the smallest statistical errors. The statistical errors are too large for some of the sea and valence masses to make a judgment about the light quark mass dependence.

Throughout the plots and tables data from an ensemble will be referred to by its sea quark mass content in lattice units. This label uniquely identifies which ensemble a particular data point is from. Fit results for the medium coarse data are not shown in Figs. 3.10-3.11.

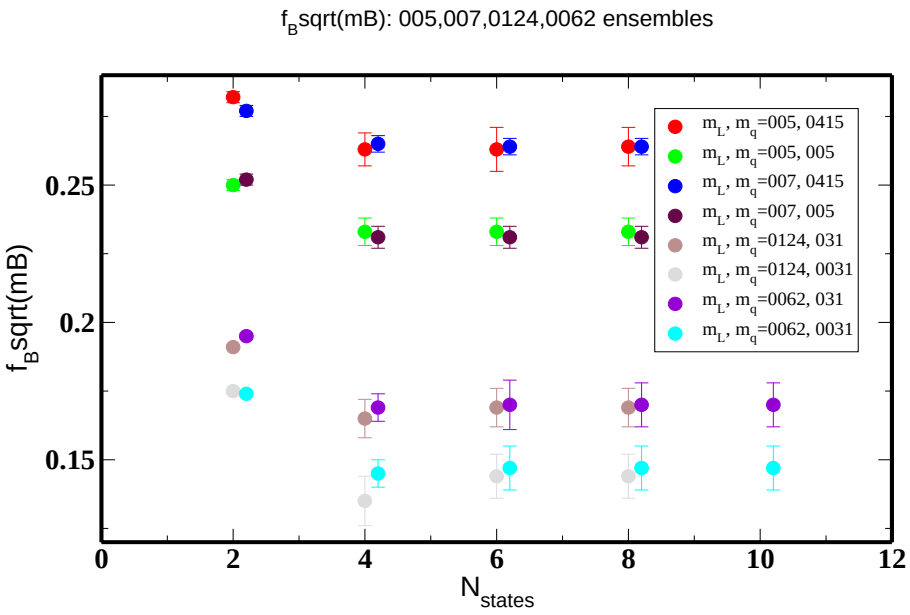

Figure 3.2: $f_B\sqrt{m_B B_B}$ for a variety of states. Fits are stable by $N_{states} = 4$.

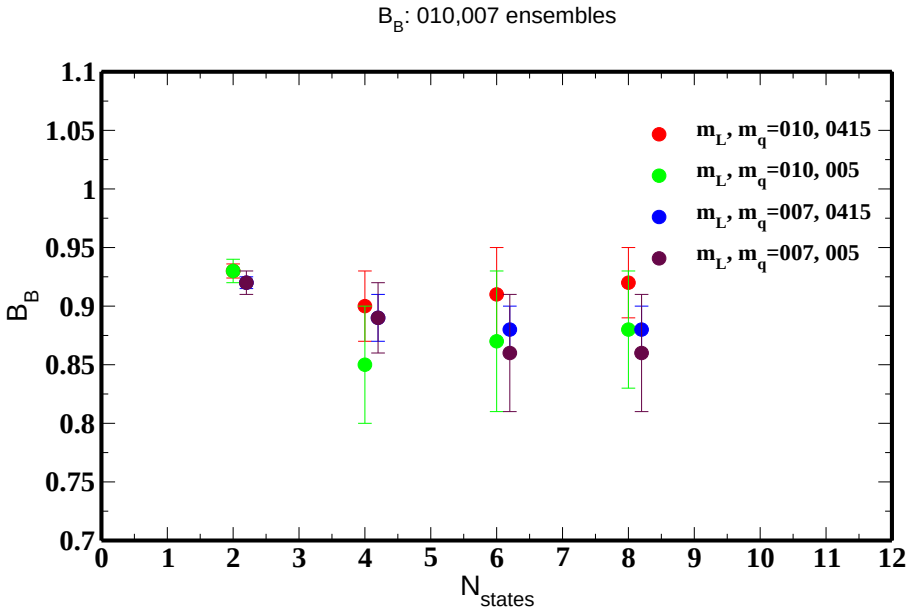

Figure 3.3: B_B for a variety of states. Heavier valence mass data is stable by $N_{states} = 4$. The light valence mass data's central value is stable at $N_{states} = 4$, but the errors increase and stabilize at $N_{states} = 6$.

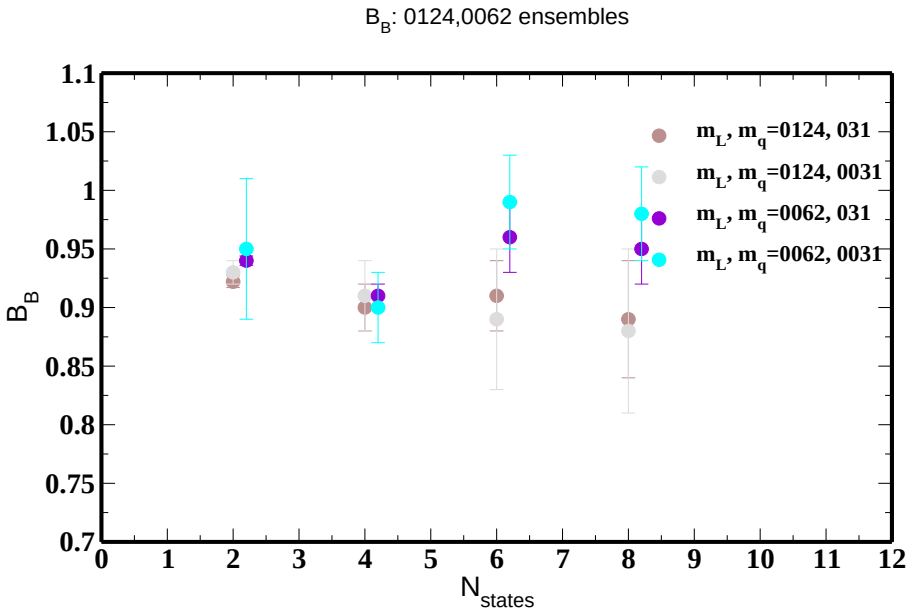

Figure 3.4: B_B for a variety of states. Same case as coarse B_B data.

$\beta_q a^{3/2} = f_{B_q}\sqrt{m_{B_q} B_{B_q}} a^{3/2}$
Medium Coarse (a=0.15 fm)
m_q=0.0048,0.007,0.0097,0.0194,0.029,0.0484
0097/0484
0.311(20), 0.322(16), 0.332(14), 0.349(13),0.355(20),0.383(20)
0194/0484
0.306(43), 0.304(44), 0.302(44), 0.322(35),0.347(27),0.386(16)
0290/0484
0.344(29), 0.348(20), 0.351(16), 0.356(15),0.369(17),0.394(21)
Coarse (a=0.12 fm)
m_q=0.005,0.007,0.01,0.02,0.03,0.0415
005/050
0.225(9), 0.227(8), 0.230(9), 0.240(9),0.250(8),0.260(8)
007/050
0.223(6), 0.225(6), 0.228(6), 0.241(4),0.251(5),0.261(5)
010/050
0.217(8), 0.222(7), 0.228(8), 0.244(5),0.256(5),0.269(4)
020/050
0.218(11), 0.219(8), 0.225(7), 0.238(7),0.249(6),0.260(6)
Fine (a=0.09 fm)
m_q=0.0031,0.0044/0.0042,0.0062,0.0124,0.0272,0.031
0062/031
0.143(5), 0.146(4), 0.148(4), 0.155(3),0.168(3),0.172(3)
0124/031
0.136(6), 0.138(5), 0.141(5), 0.148(4),0.161(4),0.165(4)

Table 3.4: Correlator fit results for $f_{B_q}\sqrt{M_{B_q} B_{B_q}}$.

$\beta_q^S a^{3/2} = f_{B_q}\sqrt{m_{B_q} B_{B_q}^S}\, a^{3/2}$
Medium Coarse (a=0.15 fm)
m_q=0.0048,0.007,0.0097,0.0194,0.029,0.0484
0097/0484
0.371(17), 0.380(14), 0.388(14), 0.401(13),0.420(13),0.458(10)
0194/0484
0.377(15), 0.379(14), 0.380(13), 0.398(12),0.417(11),0.452(9)
0290/0484
0.372(18), 0.373(18), 0.378(17), 0.398(15),0.418(13),0.460(9)
Coarse (a=0.12 fm)
m_q=0.005,0.007,0.01,0.02,0.03,0.0415
005/050
0.265(14), 0.266(13), 0.270(12), 0.282(12),0.292(13),0.305(13)
007/050
0.280(6), 0.283(5), 0.287(5), 0.300(4),0.311(4),0.325(4)
010/050
0.269(8), 0.273(7), 0.279(9), 0.296(7),0.311(6),0.327(6)
020/050
0.268(10), 0.268(9), 0.276(8), 0.291(8),0.304(8),0.318(8)
Fine (a=0.09 fm)
m_q=0.0031,0.0044/0.0042,0.0062,0.0124,0.0272,0.031
0062/031
0.166(6), 0.168(6), 0.170(6), 0.176(5),0.192(5),0.171(6)
0124/031
0.171(6), 0.172(6), 0.173(5), 0.179(5),0.195(4),0.200(4)

Table 3.5: Correlator fit results for $f_{B_q}\sqrt{M_{B_q} B_{B_q}^S}$.

B_{B_q}
Medium Coarse (a=0.15 fm)
m_q=0.0048,0.007,0.0097,0.0194,0.029,0.0484
0097/0484
0.90(6)), 91(6), 0.91(5), 0.92(4),0.93(4),0.94(3)
0194/0484
0.91(6), 0.90(5), 0.91(4), 0.92(4), 0.93(3), 0.94(2)
0290/0484
1.03(77), 1.01(66), 0.99(6), 0.96(4), 0.96(3), 0.95(2)
Coarse (a=0.12 fm)
m_q=0.005,0.007,0.01,0.02,0.03,0.0415
005/050
0.94(6), 0.95(6) 0.96(6), 0.97(5), 0.97(4), 0.97(4)
007/050
0.89(4), 0.89(3), 0.89(2), 0.89(2), 0.89(2), 0.89(2)
010/050
0.85(7), 0.86(6), 0.86(8), 0.89(5), 0.89(5), 0.90(4)
020/050
0.92(7), 0.91(6), 0.91(6), 0.92(4), 0.93(4), 0.92(3)
Fine (a=0.09 fm)
m_q=0.0031,0.0044/0.0042,0.0062,0.0124,0.0272,0.031
0062/031
0.90(3), 0.90(3), 0.91(3), 0.91(2), 0.91(2), 0.91(2)
0124/031
0.90(4), 0.91(3), 0.92(3), 0.91(3), 0.90(2), 0.90(2)

Table 3.6: Correlator fit results for B_{B_q}.

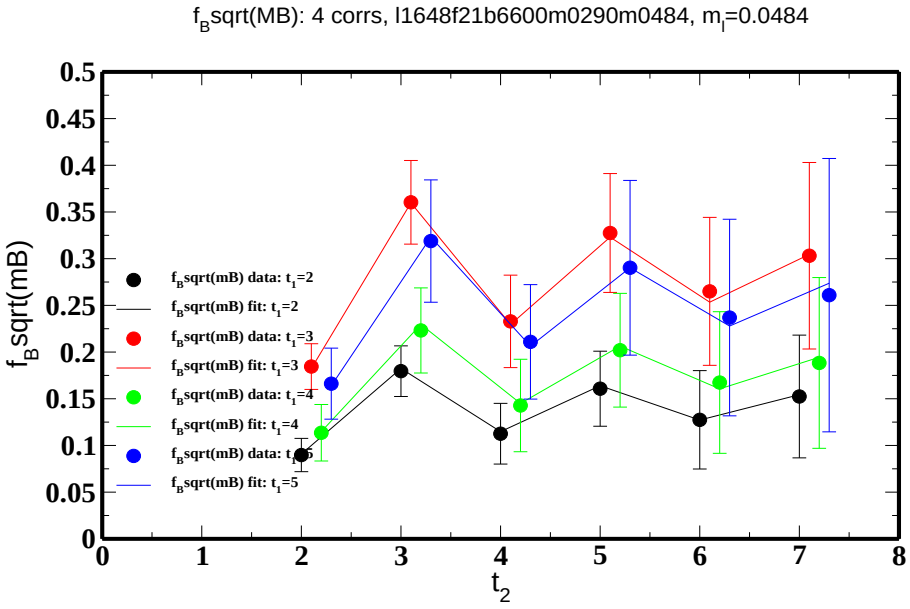

Figure 3.5: $f_B\sqrt{m_B B_B}$: Example fit. All fits are 2 dimensional. The different t_1 timeslices are overlayed.

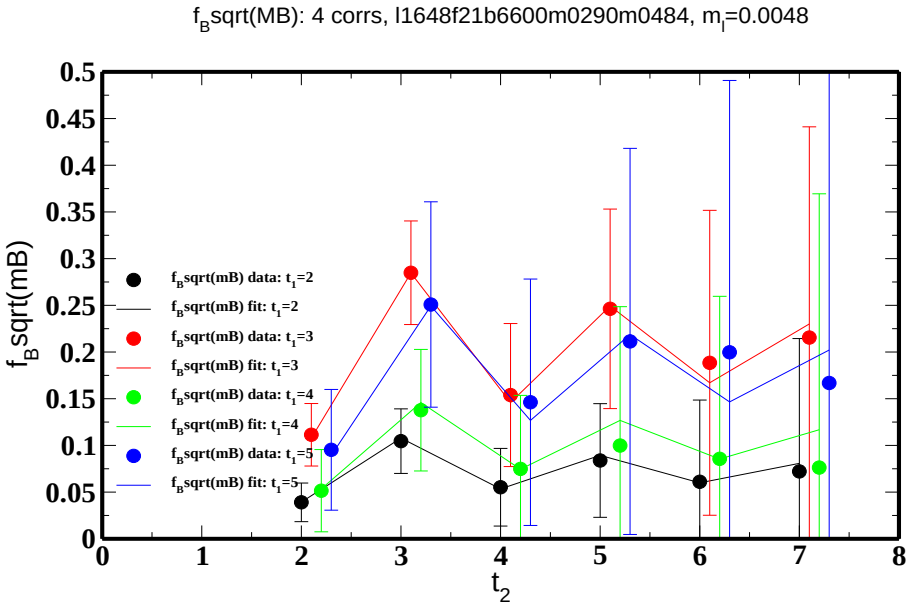

Figure 3.6: $f_B\sqrt{m_B B_B}$: Example fit.

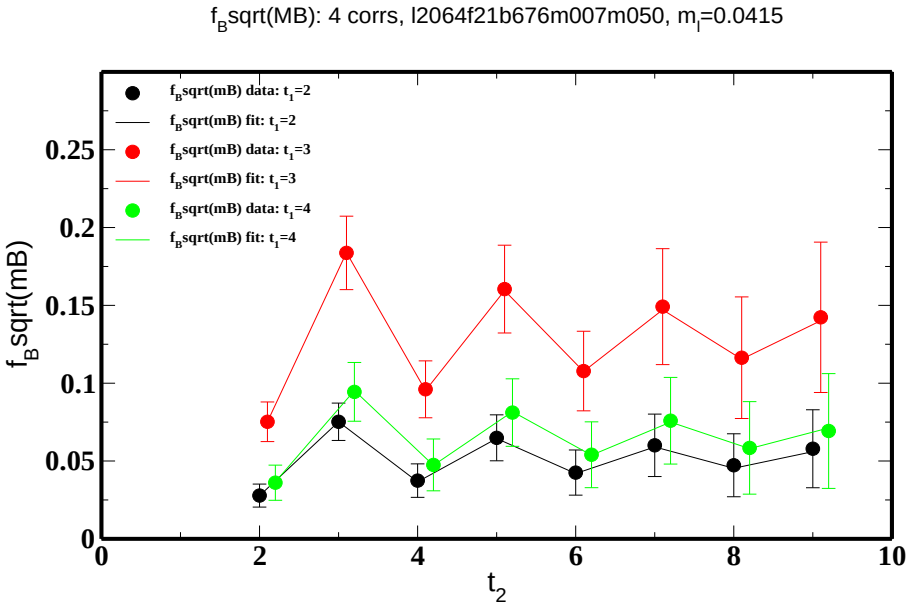

Figure 3.7: $f_B\sqrt{m_B B_B}$: Example fit.

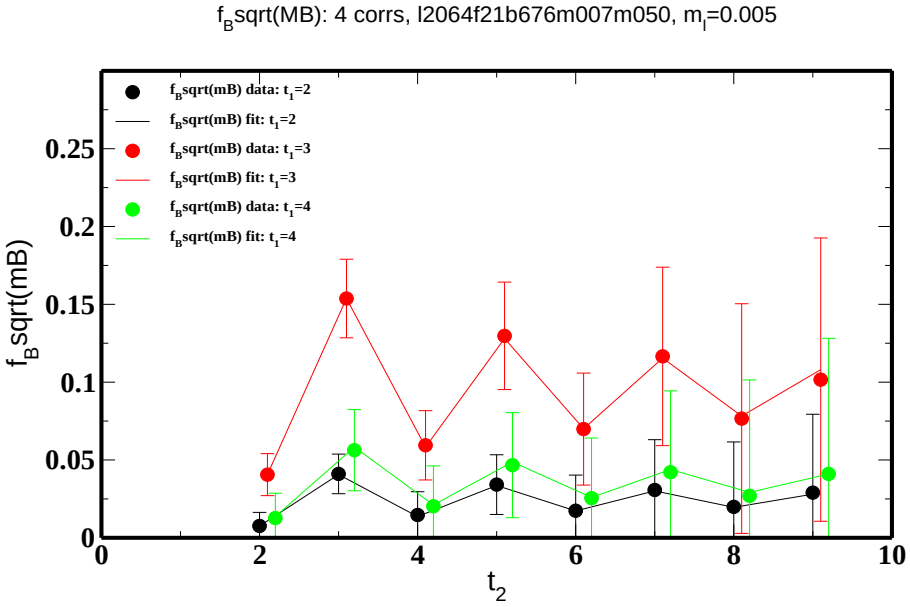

Figure 3.8: $f_B\sqrt{m_B B_B}$: Example fit.

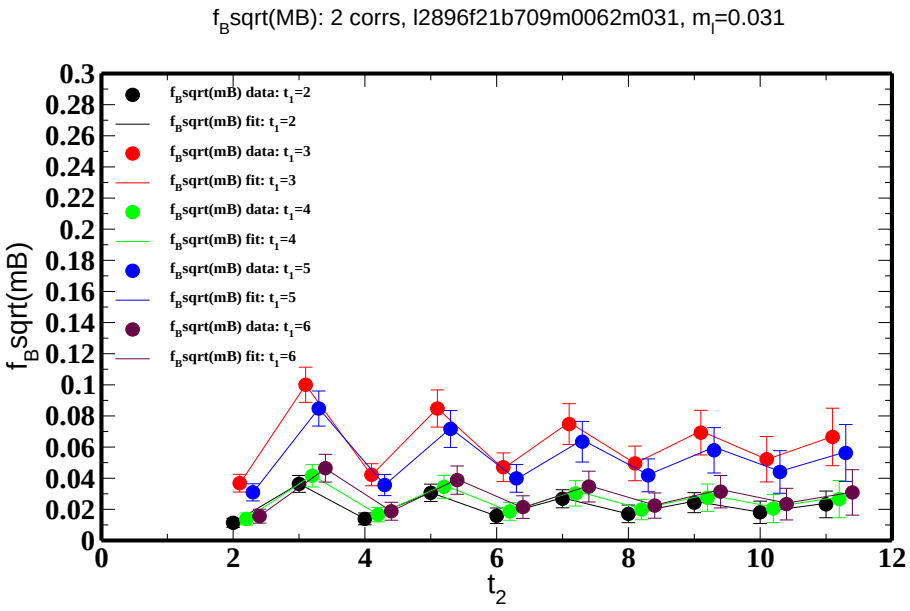

Figure 3.9: $f_B\sqrt{m_B B_B}$: Example fit.

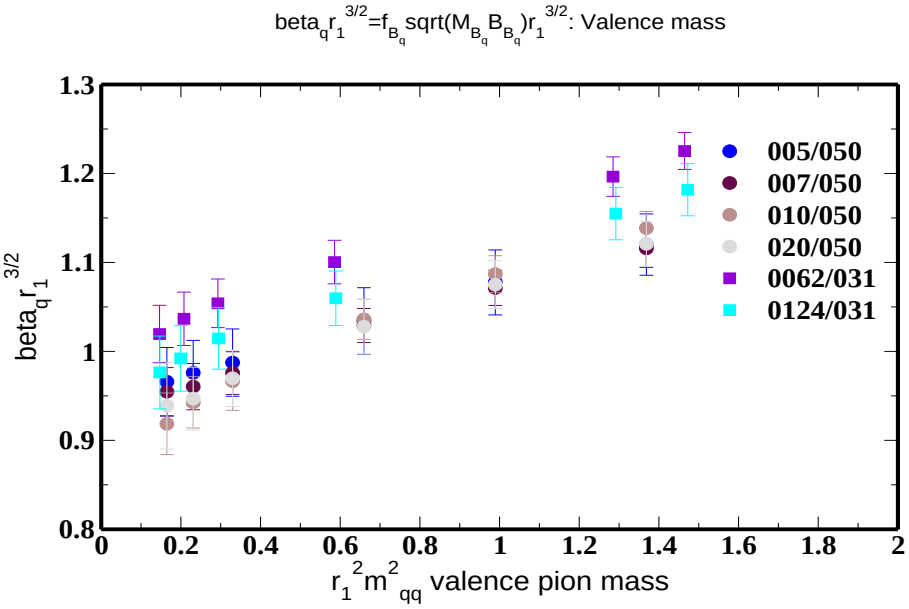

Figure 3.10: $\beta_q = f_{B_q}\sqrt{m_{B_q} B_{B_q}}$. Fit results are shown. The sea mass dependence is weak. r_1 is a scale dependent quantity used to convert data in lattice units to a common physical scale. It's precise definition and the definition of $m_{qq}^2 \sim m_q$ will be explained in Chapter 6.

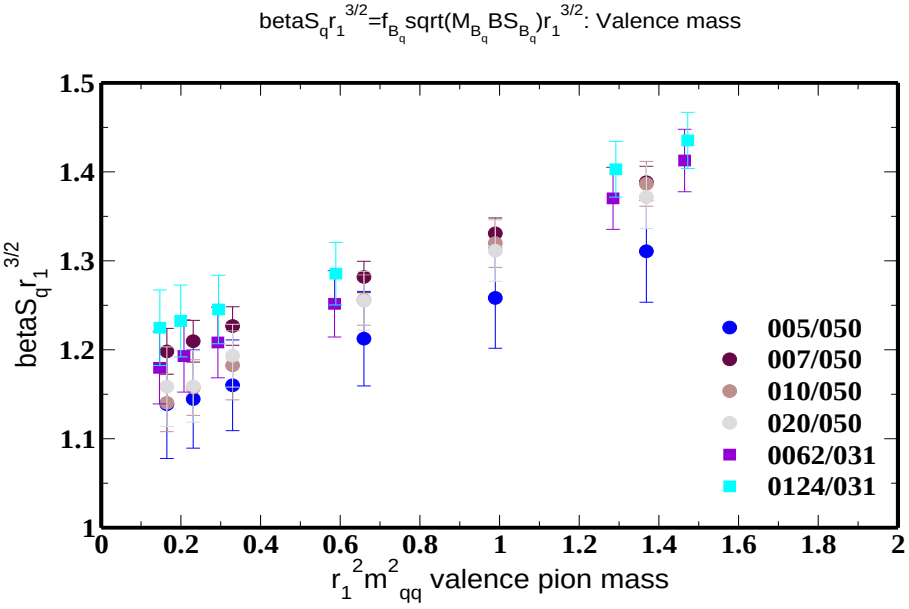

Figure 3.11: $\beta_q^S = f_{B_q}^S\sqrt{m_{B_q} B_{B_q}^S}$. Fit results are shown. The light mass dependence of the data is nearly identical to that of β_q.

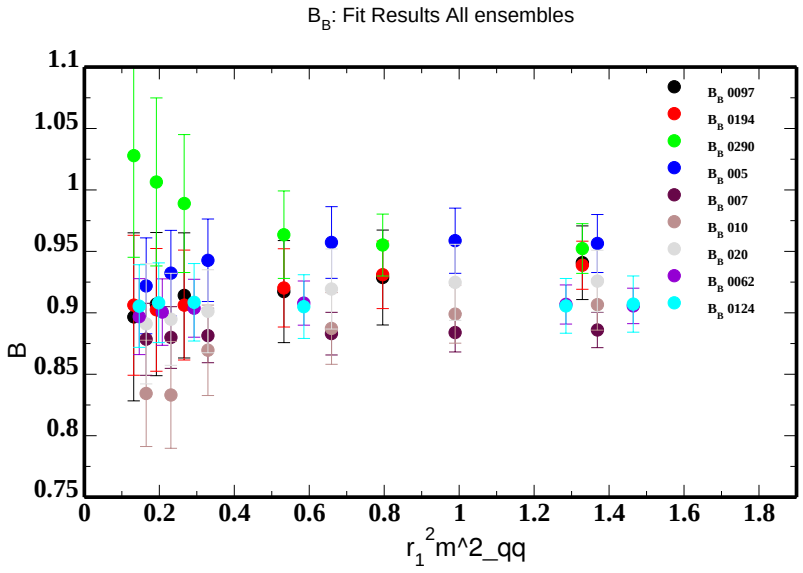

Figure 3.12: Fit results are shown for B_{B_q}. The sea mass dependence is weak in the data with small statistical errors. Some of the data is extremely noisy.

3.2.3 ISA Fits: Procedure

This method was introduced by Ruth van der Water of the Fermilab Lattice and MILC collaborations for the calculation of $B \to \pi$ form factors. The iterated super-average (ISA) is a method to reduce the oscillating excited state contamination. We have found that with our current statistics it is not an improvement over the direct fit method, and is much worse for the light valence mass correlators. Nevertheless it provides a consistency check with the direct fit results and it makes the data easier to visualize, and so is worth examining. In addition the technique may become of greater use when the statistical errors in the correlators are significantly reduced.

Consider the first four terms, or first 2 states, in the three-point function with the ground state exponential dependence scaled out

$$\begin{aligned} R(t_1,t_2) &= e^{m_0(t_1+t_2)} C_{Q_1}(t_1,t_2) \\ &= e^{m_0(t_1+t_2)} \sum_{i,j} (-1)^{it_1}(-1)^{jt_2} \frac{Z_i Z_j O_{ij}}{(2E_i)(2E_j)} e^{-E_i t_1 - E_j t_2} \\ &\approx \frac{|Z_0|^2 O_{00}}{4m_B^2} + \frac{Z_0 Z_1 \frac{(O_{01}+O_{10})}{2}}{4m_B E_1}((-1)^{t_2} e^{-\Delta_{10} t_2} + (-1)^{t_1} e^{-\Delta_{10} t_1}) \\ &+(-1)^{t_1+t_2} \frac{|Z_1|^2 O_{11}}{4E_1^2} e^{-\Delta_{10} t_1 - \Delta_{10} t_2}, \end{aligned} \tag{3.17}$$

where $\Delta_{10} = E_1 - m_B$. Now we compute the average of neighboring time slices in t_2, which we refer to as the Masataka average (MA).

$$\begin{aligned} MA(t_1,t_2) &= \frac{R(t_1,t_2) + R(t_1,t_2+1)}{2} \approx \frac{|Z_0|^2 O_{00}}{4m_B^2} \\ &+\frac{Z_0 Z_1 \frac{(O_{01}+O_{10})}{2}}{8m_B E_1}((-1)^{t_2} e^{-\Delta_{10} t_2}(1 - e^{-\Delta_{10}}) \\ &+2(-1)^{t_1} e^{-\Delta_{10} t_1}) + (-1)^{t_1+t_2} \frac{|Z_1|^2 O_{11}}{8E_1^2} e^{-\Delta_{10} t_1 - \Delta_{10} t_2}(1 - e^{-\Delta_{10}}), \end{aligned} \tag{3.18}$$

and then again in t_1 which we refer to as the super average (SA)

$$\begin{aligned} SA(t_1,t_2) &= \frac{MA(t_1,t_2) + MA(t_1+1,t_2)}{2} \approx \frac{|Z_0|^2 O_{00}}{4m_B^2} \\ &+\frac{Z_0 Z_1 \frac{(O_{01}+O_{10})}{2}}{8m_B E_1}((-1)^{t_2} e^{-\Delta_{10} t_2}(1 - e^{-\Delta_{10}}) \\ &+(-1)^{t_1} e^{-\Delta_{10} t_1}(1 - e^{-\Delta_{10}})) + (-1)^{t_1+t_2} \frac{|Z_1|^2 O_{11}}{16E_1^2} e^{-\Delta_{10} t_1 - \Delta_{10} t_2}(1 - e^{-\Delta_{10}})^2 \\ &\approx \frac{|Z_0|^2 O_{00}}{4m_B^2} + \frac{Z_0 Z_1 \frac{(O_{01}+O_{10})}{2}}{4m_B E_1}((-1)^{t_2} e^{-\Delta_{10} t_2}(-\Delta_{10}/2 + \Delta_{10}^2/2) \\ &+(-1)^{t_1} e^{-\Delta_{10} t_1}(-\Delta_{10}/2 + \Delta_{10}^2/2)) + (-1)^{t_1+t_2} \frac{|Z_1|^2 O_{11}}{4E_1^2} e^{\Delta_{10} t_1 \Delta_{10} t_2}(\Delta_{10}/2)^2 \\ &+\mathcal{O}(\Delta_{10}^3), \end{aligned} \tag{3.19}$$

where a typical value for $\Delta_{10}/2 = 0.11$ in lattice units, which is how much the oscillating states have been suppressed.

The process can be repeated, first over one time and then over the other, in order to suppress the excited states by a typical value of $\Delta_{10}^2/2 = 0.0242$, or about 2% of it's original value. This additional averaging is referred to as the iterated superaverages

(ISA_n), where n is the number of additional timeslices that have been averaged over. It should be noted that more highly excited states are not systematically suppressed by this procedure. Also, smearing over time slices mixes the earlier, statistically cleaner time slice data points with later, noisier time slice points, reducing the statistical power of the sample.

In order to isolate $f_B\sqrt{m_B B_B}$ a bootstrap ensemble of two-point function fit results for Z_0 and m_0 must be generated. The same bootstrap ensemble is then used to fit the three-point correlator to Eq. (3.19). B_B is more straightforward: the ratio of the three-point correlator and two two-point decay correlators give B_B directly, and so no two-point function fits are necessary.

3.2.4 ISA Fits: Results

As a demonstration of the ISA method's effect on the correlation function we plot the three-point function after each step of the averaging procedure has been performed in Figs. (3.13-3.16). As shown in Fig. (3.17) the method does not work as well for noisier data, in our case the data with the lightest valence quark masses. For data with better statistics the method clearly removes most or all of the oscillating states' contributions, and a plateau fit is all that is necessary to obtain good χ^2s. In fact including additional excited states does not improve the fit: in all cases their contribution has been reduced to less than 1% of the ground state's. It is better to use exactly the same smearings in two-point data as the three-point data for the ISA fits because the fits are so sensitive to the ground state energy: the ground state energy is systematically slightly different depending on where the smearings are located. While the different energies are statistically comparable, the correlation function is scaled by the exponential of the energy, and the "flatness" of the correlation function produced by this scaling can be reduced if the wrong energy is used.

The same time slices appear to work for all ensembles (typically $t_1 = t_2 = 3 - 8$), but the method appears to work much better for heavier sea and valence masses and finer lattices. The best fits are obtained for the ensemble with the most configurations (and hence best statistics), the 007/050 ensemble. Fits at two different valence masses are shown in Figs. (3.18-3.19). The χ^2's are good in these fits, ~ 1.

Fit results for the ISA method are tabulated in Table (3.7). We have not been able to get good results for all ensembles for $f_B\sqrt{mB_B}$ yet. B_B is more straightforward, because forming a ratio between the three-point function and two decay constant two-point functions removes the ground state energy and B meson amplitude without contributing additional statistical errors. $f_B\sqrt{mB_B}$ requires a separate two-point fit to obtain these quantities. The B_B ISA results compare reasonably well with the direct fits. Due to the above considerations only results for B_B are presented. These results are not used in the chiral fits.

B_{B_q}
Medium Coarse (a=0.15 fm)
m_q=0.0048,0.007,0.0097,0.0194,0.029,0.0484
0097/0484
0.91(3) 0.92(2), 0.92(1), 0.91(2), 0.92(1), 0.92(1)
0194/0484
0.93(3), 0.93(2), 0.93(2), 0.96(2), 0.96(1), 0.97(1)
0290/0484
0.92(4), 0.91(3), 0.92(2), 0.90(2), 0.93(1)
Coarse (a=0.12 fm)
m_q=0.005,0.007,0.01,0.02,0.03,0.0415
005/050
0.90(2), 0.91(2), 0.91(2), 0.92(1), 0.92(1), 0.92(1)
007/050
0.91(2), 0.91(2) 0.91(2), 0.91(1), 0.91(1), 0.91(1)
010/050
0.86(3), 0.85(2), 0.87(2), 0.89(2), 0.90(1), 0.91(1)
020/050
0.95(3), 0.92(2), 0.93(2), 0.92(1), 0.92(1), 0.92(1)
Fine (a=0.09 fm)
m_q=0.0031,0.0044/0.0042,0.0062,0.0124,0.0272,0.031
0062/031
0.90(2), 0.89(2), 0.89(2), 0.91(1), 0.91(1), 0.91(1)
0124/031
0.95(2), 0.93(2), 0.93(1) 0.93(1), 0.93(1), 0.93(1)

Table 3.7: ISA fit results for B_{B_q}.

Examples of ISA Procedure-Figs. (3.13-3.16): Heavy valence masses (least noisy data) work well.

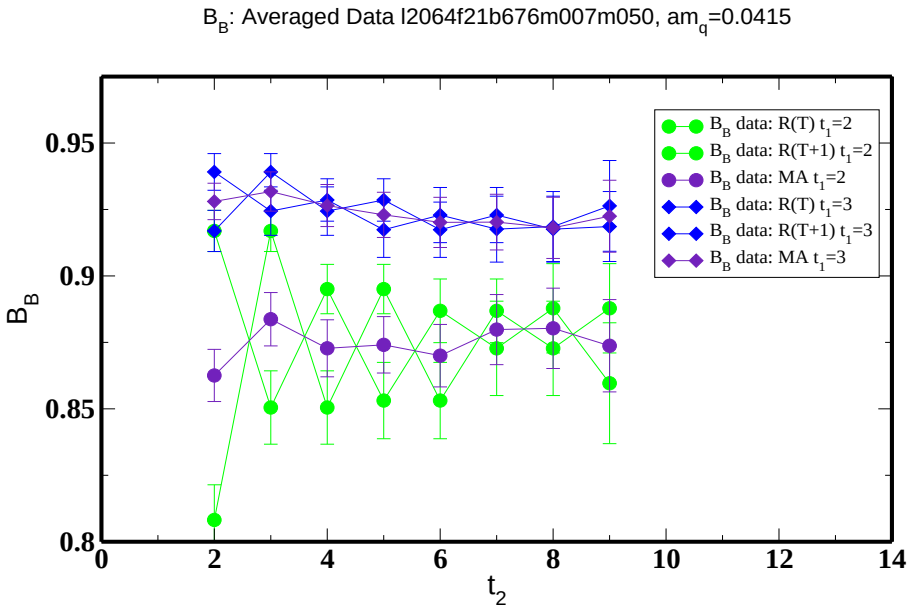

Figure 3.13: MA's effect: B_B. The oscillations along t_2 are significantly reduced. Green and blue data are the offset scaled correlators, $R(T)$ and $R(T+1)$, for timeslices $t_1 = 2, 3$, from which the MA's are constructed. Lines are for visualization only, NOT fits to the data.

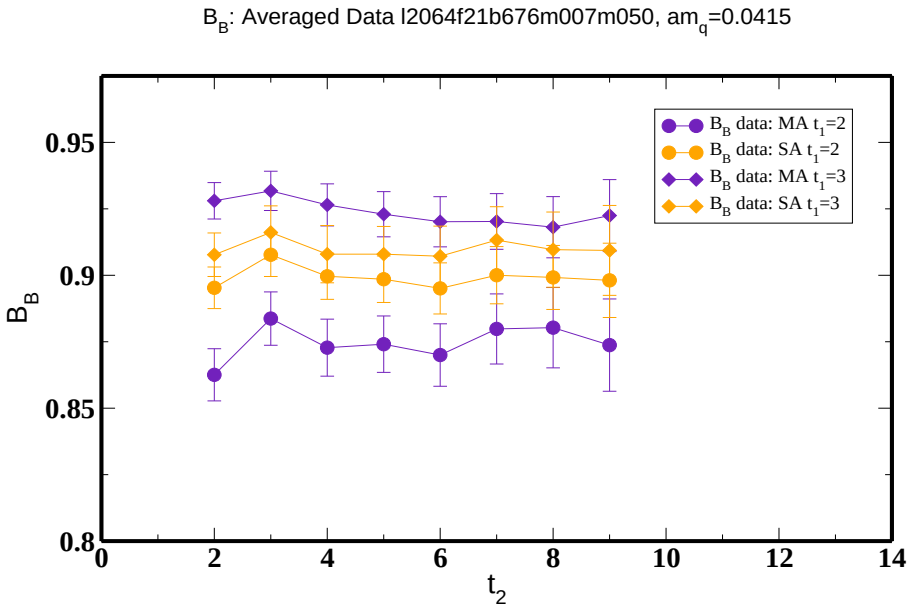

Figure 3.14: SA's effect: B_B. The oscillations along t_1 are now also reduced.

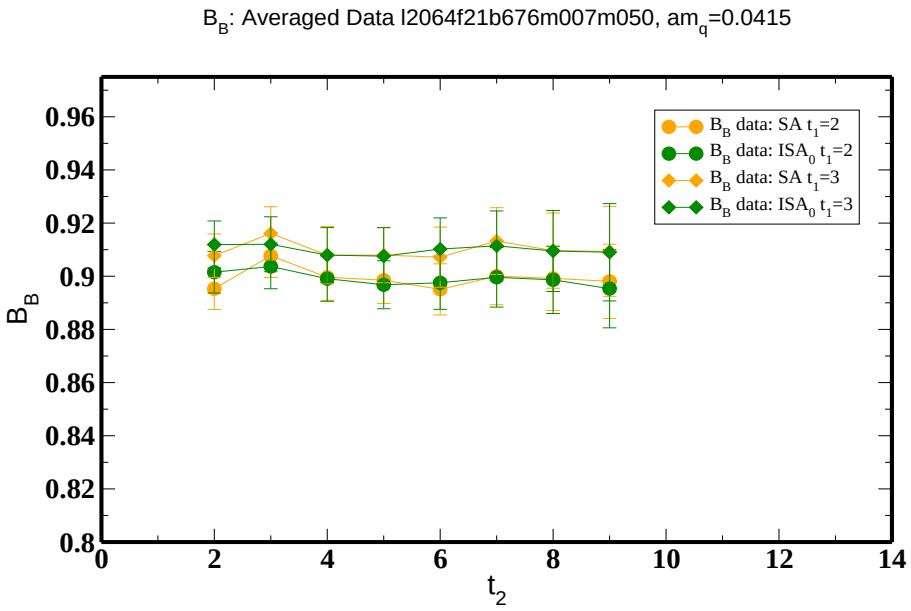

Figure 3.15: ISA_0's effect: B_B

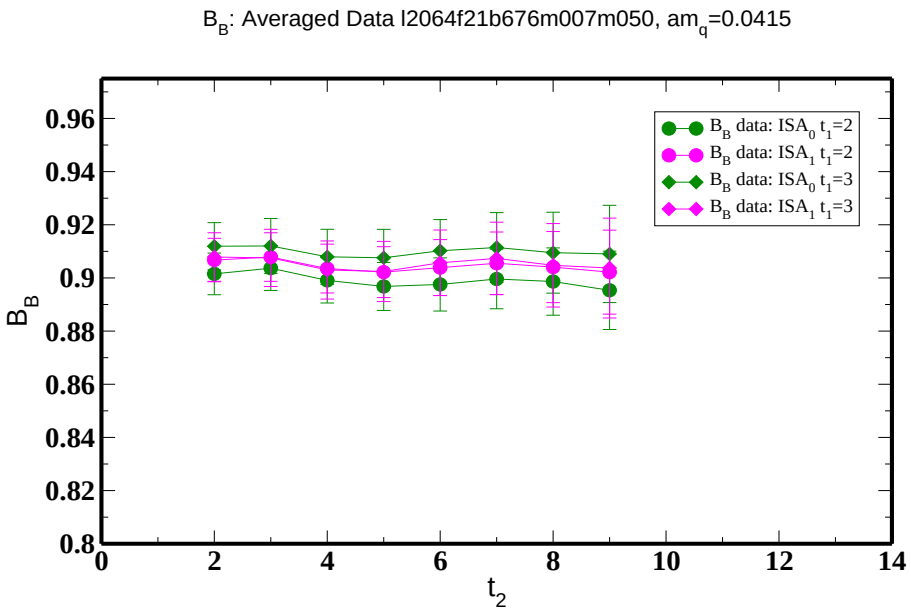

Figure 3.16: ISA_1's effect: B_B. Oscillations are no longer discernible and a plateau is produced.

Examples of ISA Procedure-Fig. (3.17): Light valence masses (most noisy data) work poorly and are not shown.

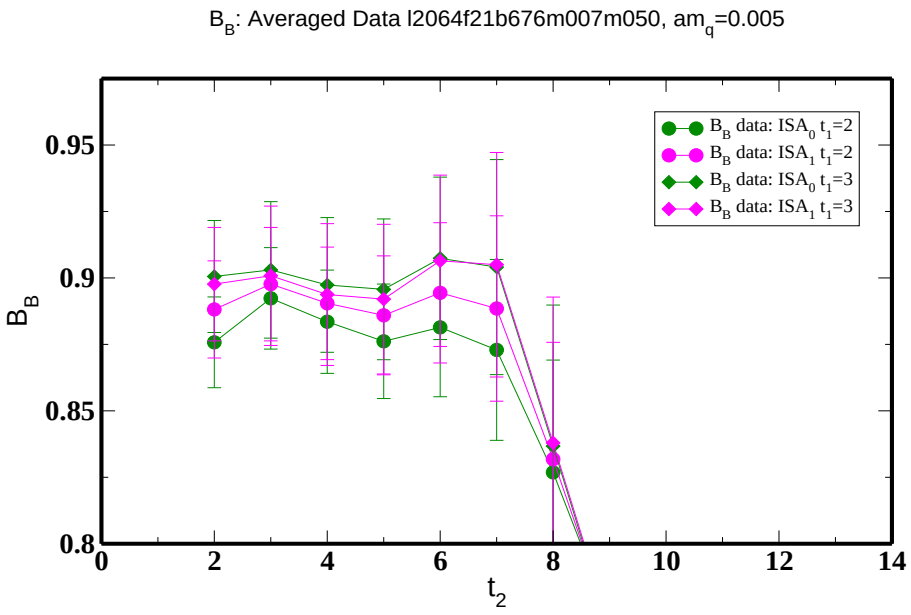

Figure 3.17: ISA procedure's effect on noiser data, in this case a lighter mass valence quark: B_B. The data by ISA_1 is too noisy to obtain a reliable plateau.

Example Fits to ISA_1-Figs. (3.18-3.19)

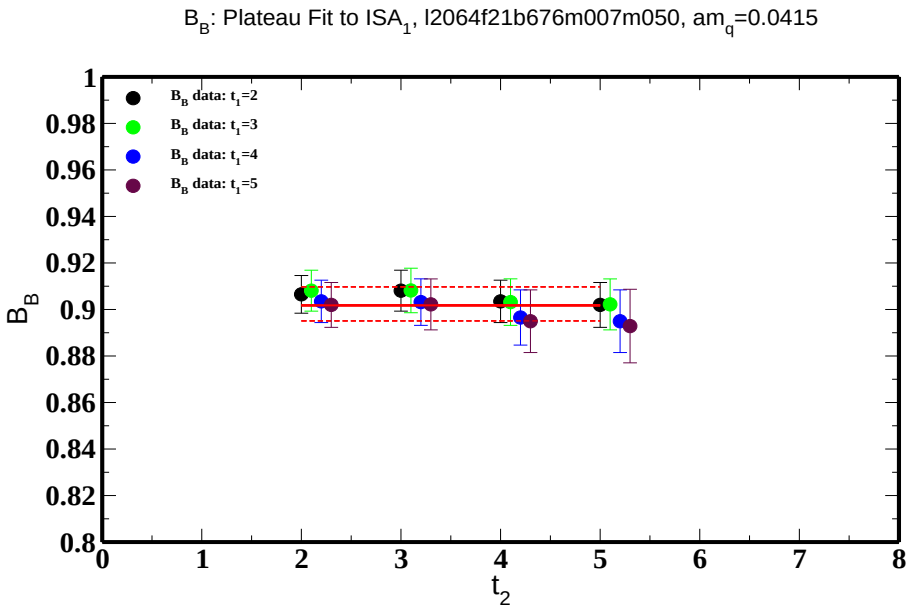

Figure 3.18: Plateau fit to ISA_1 data. The fit looks good for less noisy data. The upper and lower dashed lines are the error bars on the fit, and the central line is the fit.

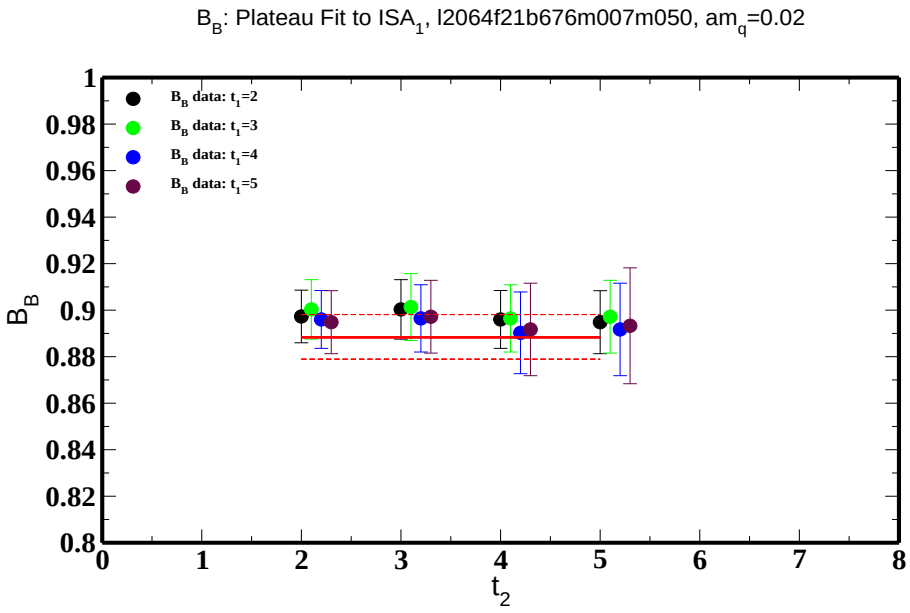

Figure 3.19: Plateau fit to ISA_1 data.

Chapter 4

Perturbative Matching

QCD in the continuum and on the lattice necessarily use different UV regularization schemes. For finite lattice spacing the lattice has a hard cutoff of π/a and hence no UV divergences, while in the continuum there are UV divergences and a variety of schemes such as dimensional regularization or Paul-Villars used to control them. Thus while the lattice and continuum theories have the same low energy behavior, their UV behavior differs and a matching calculation must be performed if connections with existing continuum results are to be made. The details of the matching calculation for the B mixing operator are beyond the scope of this report, however the calculation will be outlined in this chapter and results for the perturbative coefficients presented.

The perturbative corrections to a continuum operator O^{cont} have the general form

$$\langle O \rangle^{cont} = \langle O \rangle^{tree} + \sum_{n=1} \alpha_s^n \sum_i Z_i^{cont,n} \langle O \rangle_i^{tree,n} \tag{4.1}$$

where n is the number of loops, or the order in α_s at which the calculation is performed, $Z_i^{cont,n}$ are the perturbatively determined coefficients, and $O_i^{tree,n}$ consists of the tree level operator O^{tree} and tree level operators that mix with it under renormalization at order n. The operators that mix must have the same symmetries as O^{tree}. The case is identical on the lattice, where

$$\langle O \rangle^{lat} = \langle O \rangle^{tree} + \sum_{n=1} \alpha_s^n \sum_j Z_j^{lat,n} \langle O \rangle_j^{tree,n}, \tag{4.2}$$

however different operators may mix than in the continuum because of different lattice and continuum symmetries. Setting the on-shell amplitudes equal the one-loop matching relation is

$$\langle O \rangle^{cont} = \langle O \rangle^{lat} + \alpha_s \sum_j \rho_j^n \langle O \rangle_j^{lat,n}, \tag{4.3}$$

where the matching coefficients,

$$\rho_i^n = Z_{cont}^n - Z_{lat}^n, \tag{4.4}$$

are the difference of the lattice and continuum renormalization coefficients at order n.

As discussed in Chapter 2 lattice operators will generally have large renormalizations unless they are tadpole improved and these improvement coefficients must be incorporated into the perturbative matching. In addition, using an optimal coupling constant, where many higher order effects are incorporated into the coupling's definition, greatly reduces the size of higher order effects. The way we determine this

optimal coupling and its scale are explained in Sec. 4.1. The operators contributing to the B mixing matching calculation are found in Sec. 4.2. The diagrams contributing to B mixing renormalization are then detailed and the matching coefficients' values presented in Sec. 4.3.

The author is not directly involved in the matching aspect of the calculation, which is being carried out by Elvira Gamiz. The perturbative matching calculation is also not yet complete. This means the final results for β_d and β_s presented could be shifted by 5-10%. Preliminary calculations of the coefficients suggest the value for ξ will not significantly change. The shift in values is just an overall shift of the data, so the methods developed for the analysis of the matrix elements described in this report will not change.

4.1 Determination of the Optimal Coupling: α_V

When a lattice quantity is perturbatively expanded in its bare coupling constant, $\alpha_{lat} = \frac{g_0^2}{4\pi}$, perturbative effects are typically drastically underestimated and there is a large mismatch between lattice and continuum perturbative results for short distance quantities. As pointed out by Lepage and Mackenzie in [25] this is due to large renormalizations in α_{lat} arising from tadpole diagrams, which can be accounted for by using a suitably defined coupling α_s.

The large renormalizations due to tadpole diagrams are mostly removed in tadpole improvement, where $U_\mu \rightarrow U_\mu/u_0$ and $\alpha_{lat} \rightarrow \hat{\alpha}_{lat} = \frac{g_0^2}{u_0^4}$. $\hat{\alpha}_{lat}$ could be used in perturbative expansions; however, a better choice for α_s is possible. The aim is to include as many of the higher order effects in the definition of α_s as possible. The resulting optimal choice of coupling, referred to as α_V, is formerly equivalent to α_{lat} up to the order in α_s one is working at, but in practice there are large coefficients relating the couplings and their numerical values are very different.

A natural way to ensure α_s incorporates many higher order effects is to define it in a physically motivated way, such as through the static quark potential $V(q)$,

$$V(q) = -\frac{(4/3)4\pi\alpha_V(q)}{q^2}, \tag{4.5}$$

where $V(q)$ can be measured by a lattice calculation at a particular scale q, and then $\alpha_V(q)$ determined. This definition of the coupling takes into account the tadpole effects and should agree closely with $\hat{\alpha}_{lat}$, which in fact it does to a few percent at the scale of the cutoff $q = \pi/a$ [34],

$$\alpha_V(\pi/a) = \hat{\alpha}_{lat}(1 + 0.513\alpha_V + \mathcal{O}(\alpha_V^2)). \tag{4.6}$$

$\alpha_V(q)$ measured at a momentum q can be run to the desired scale by the relation

$$\alpha_V(q) = \alpha_V(\mu)(1 + \beta_0 \ln(q/\mu)^2\alpha_V(\mu) + (\beta_0 \ln(q/\mu)^2)\alpha_V(\mu))^2 + \cdots \tag{4.7}$$

To capture as much of the renormalization effects as possible it is advantageous to use a value for the scale q, q^*, that is representative of the process being studied, which can be achieved by using a typical gluon momentum in the process. For this calculation

we use a value of q^* very close to that calculated for heavy-light currents, $q^* = 2/a$.

The basic procedure for the coupling determination that we use in practice for the B mixing calculation is as follows:

1. Tadpole improve lattice operators causing their perturbative expansions to behave more like their continuum counterparts.
2. Use a measured value for $\alpha_V(q)$, in our case a value obtained from small Wilson loops defined in Ref. [25].
3. Evolve $\alpha_V(q)$ to $q^* = 2/a$ using Eq. (4.7).

4.2 Operator Mixing and the Matching Relation

Any operator which has the same symmetries and dimension as the mixing operator, Q^1, could potentially arise at one-loop order in the perturbative calculation. There are 12 color singlet and 12 color mixed Dirac structures of four-quark operators which respect hypercubic symmetry and are parity invariant,

$$\begin{aligned}
&(1-\gamma_5)\times(1-\gamma_5),\ (1-\gamma_5)\times(1+\gamma_5),\ (1+\gamma_5)\times(1-\gamma_5), \\
&(1+\gamma_5)\times(1+\gamma_5),\ \gamma_\mu(1-\gamma_5)\times\gamma_\mu(1-\gamma_5),\ \gamma_\mu(1-\gamma_5)\times\gamma_\mu(1+\gamma_5), \\
&\gamma_\mu(1+\gamma_5)\times\gamma_\mu(1-\gamma_5),\ \gamma_\mu(1+\gamma_5)\times\gamma_\mu(1+\gamma_5),\ \sigma_{\mu\nu}(1-\gamma_5)\times\sigma_{\mu\nu}(1-\gamma_5), \\
&\sigma_{\mu\nu}(1-\gamma_5)\times\sigma_{\mu\nu}(1+\gamma_5),\ \sigma_{\mu\nu}(1+\gamma_5)\times\sigma_{\mu\nu}(1-\gamma_5),\ \sigma_{\mu\nu}(1+\gamma_5)\times\sigma_{\mu\nu}(1+\gamma_5),
\end{aligned} \tag{4.8}$$

where $\sigma_{\mu\nu} = \frac{i}{2}[\gamma_\mu, \gamma_\nu]$. Negative parity operators cannot mix with Q^1 since the lattice actions used are parity invariant. Also by considering the chiral symmetry of the naive quark, q, it can be shown that only operators with the same chirality as Q^1_q can mix under renormalization [16].

Finally the $\sigma_{\mu\nu}(1-\gamma_5)\times\sigma_{\mu\nu}(1-\gamma_5)$ operator can be related to $(1-\gamma_5)\times(1-\gamma_5)$ using the Fierz relation

$$\begin{aligned}
&\bar{u}_Q\sigma_{\mu\nu}(1-\gamma_5)u_q\bar{v}_Q\sigma_{\mu\nu}(1-\gamma_5)v_q = \\
&8\bar{u}_Q(1-\gamma_5)v_q\bar{v}_Q(1-\gamma_5)u_q - 4\bar{u}_Q(1-\gamma_5)u_q\bar{v}_Q(1-\gamma_5)v_q,
\end{aligned} \tag{4.9}$$

which is valid at leading order in $\Lambda_{\rm QCD}/M$, where M is the mass of the heavy quark. In our case corrections due to this approximation then start at $\mathcal{O}(\alpha_s\Lambda_{\rm QCD}/M)$, beyond the order we are considering. [17].

So of the operators listed in Eq. (4.8) only

$$Q^2 = \bar{Q}(1-\gamma_5)q\bar{Q}(1-\gamma_5)q \tag{4.10}$$

needs to be considered in mixing with Q^1, which is also the case in the continuum. The matching relation between $\overline{MS}$ and the lattice is

$$\langle Q^1\rangle(\mu)^{\overline{MS}} = (1+\alpha_V(q^*)\rho_{11}(\mu)\langle Q^1\rangle^{lat} + \alpha_V(q^*)\rho_{12}(\mu)\langle Q^2\rangle^{lat}, \tag{4.11}$$

where at the end we set $\mu = m_b$ so that many of the higher order logarithms in the

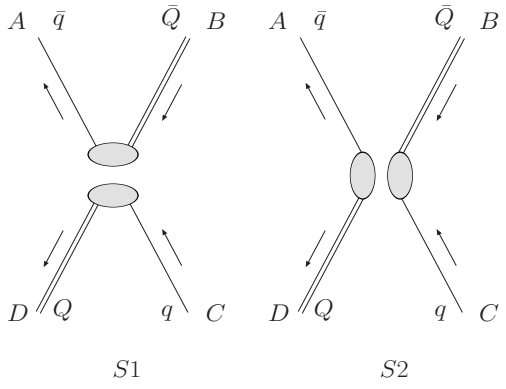

Figure 4.1: The two possible Dirac structures of the matching diagrams for Q^1, where $S1 = (\bar{u}_Q \Gamma u_q)(\bar{v}_Q \Gamma v_q)$ and $S2 = (\bar{u}_Q \Gamma v_q)(\bar{v}_Q \Gamma u_q)$

coefficients disappear. The matching coefficients take the following form

$$\rho_{XY} = Z_{XY}^{\overline{MS}} - Z_{XY}^{lat}. \tag{4.12}$$

The $\overline{MS}$ coefficients are known [21]

$$Z_{11}^{\overline{MS}} = \frac{1}{4\pi}\left(-\frac{35}{3} - 2\log(\frac{\mu^2}{M^2}) - 4\log(\frac{\lambda^2}{M^2})\right) \tag{4.13}$$

$$Z_{12}^{\overline{MS}} = -\frac{8}{4\pi}. \tag{4.14}$$

λ is fictitious gluon mass used to regulate the infrared divergences. The following sections will outline how the ρ_{XY}s are determined.

4.3 Calculation Procedure

The perturbative corrections to Q^1 can be calculated by considering scattering from a heavy anti-quark, $\bar{Q}$, light quark, q, initial state $|\bar{Q}^B, q^C\rangle$, into a heavy quark, Q, light antiquark, $\bar{q}$, final state $\langle Q^D, \bar{q}^A|$, with A, B, C, D color indices. The two possible Dirac structures, $S1$ and $S2$, that arise are shown in Fig. 4.1. The two structures arise from the four possible contractions of the tree level expression

$$\begin{aligned}&\langle Q^D, \bar{q}^A|\bar{\psi}_Q^j \Gamma \psi_q^j \bar{\psi}_Q^j \Gamma \psi_q^j |\bar{Q}^B, q^C\rangle = \\ &2\delta_{AB}\delta_{CD}[(\bar{u}_Q \Gamma u_q)(\bar{v}_Q \Gamma v_q)] - 2\delta_{AD}\delta_{BC}[(\bar{u}_Q \Gamma v_q)(\bar{v}_Q \Gamma u_q)],\end{aligned} \tag{4.15}$$

where $u_{Q,q}$ are the heavy/light quark spinors, and $v_{Q,q}$ are the heavy/light anti-quark spinors. The 12 diagrams, without considering rotations, that need to be calculated are shown in Fig. 4.2.

The Fermilab action's propagator and improved gluon vertices are given in [31] and the modifications due to rotations in [20]. The naive quark is treated as massless and its Feynman rules, propagator and improved gluon vertices, are given in [19]. The improved gluon propagator is given in [28]. Care must be taken to include the

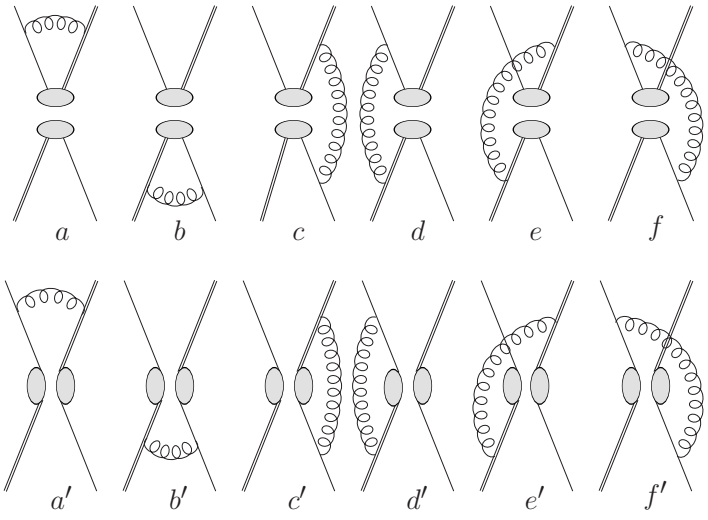

Figure 4.2: The diagrams, without rotations, contributing to the Q^1 matching calculation.

appropriate combinations of the tadpole improvement coefficient, u_0.

By considering the symmetries you can relate many of the diagrams in Fig. 4.2 with each other, up to overall color factors. After this is done there are only 4 independent topologies, and after projecting them onto the appropriate operator the following expressions for the Z_{1Y}^{lat}s are obtained

$$Z_{11}^{lat} = 2Z_{11}^{a} - 4Z_{11}^{c} + 3Z_{12}^{c} - 2Z_{11}^{e} - 2Z_{11}^{f} + Z_q + Z_Q + Z_q^u + Z_Q^u \tag{4.16}$$

$$Z_{12}^{lat} = 2Z_{12}^{a} + 8Z_{12}^{c}. \tag{4.17}$$

Z_Q, Z_q are the wavefunction renormalizations and the tadpole improvement terms Z_Q^u, Z_q^u that contribute to them are given by

$$\begin{aligned} Z_Q^u &= -\frac{1}{4\pi} u_0^{[1]} (1 + \frac{1}{am_0}) \\ Z_q^u &= -\frac{9}{4}\frac{1}{4\pi} u_0^{[1]}, \end{aligned} \tag{4.18}$$

where m_0 is the bare mass in the Fermilab action. $u_0^{[1]}$ is the one-loop tadpole correction factor defined as [16],

$$u_0 = 1 - \alpha_s u_0^{[1]} + \mathcal{O}(\alpha_s^2). \tag{4.19}$$

It is a perturbatively calculated quantity and in our case corresponds to the fourth-root of the average plaquette with the value

$$u_{0,plaquette}^{[1]} = 0.750. \tag{4.20}$$

In addition the $\mathcal{O}(1/M)$ diagrams due to the rotation of the heavy quark in Fig. 4.3 must be calculated. The black dot in Fig. 4.3 denotes a derivative acting on the

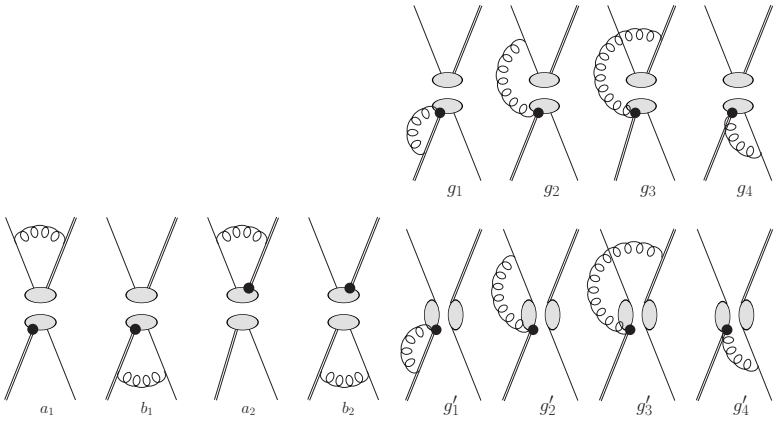

Figure 4.3: Additional diagrams due to rotations. Diagrams $c - f'$ with a rotation are not shown. The diagrams, $a_1 - f'_1$ are calculated in the same way as $a - f'$ but with a derivative acting on the heavy quark/anti-quark propagator, indicated by the black dot. Diagrams $g_1 - g'_4$ have a gluon vertex attached to the heavy quark rotation, and the same diagrams exist with the gluon vertex attached to the heavy anti-quark rotation.

heavy quark/anti-quark propagator. Only some of the diagrams are shown. Diagrams g_2, g'_2, g_4, g'_4 vanish [17].

4.4 Matching Coefficients

The integrals represented by the diagrams were calculated by Elvira Gamiz [16] to determine the lattice coefficients. The analytic expressions for the continuum coefficients in the $\overline{MS}$ scheme are used. The infrared divergences for both the lattice and the continuum coefficients are regulated using the same fictitious gluon mass. Because the infrared behavior of the two theories is the same the gluon mass dependent terms are identical and cancel.

A variety of checks have been performed on the calculation, including agreement with previous four-quark matching calculations for massless Clover/Asqtad operators and infinite mass NRQCD/Asqtad operators. Also the the gauge independence of the coefficients has been checked. Examples of the preliminary coefficients are listed in Table 4.1. They are presented in the Feynman gauge for the coarse lattice.

Z_q	-0.924+$\frac{4}{3} \times IR$
Z_Q	-0.231-$\frac{8}{3} \times IR$
Z_{11}^a	0.872-$\frac{8}{3} \times IR$
Z_{11}^c	-0.092+$\frac{1}{3} \times IR$
Z_{11}^e	-0.118+$\frac{1}{3} \times IR$
Z_{11}^f	0.164-$\frac{2}{3} \times IR$
Z_{12}^a	-0.059
Z_{12}^c	-0.007

Table 4.1: The matching coefficients for Q^1. $IR = \frac{1}{4\pi}\log(\lambda^2)$, where λ is the gluon mass used as an infrared regulator [16].

Chapter 5

Chiral Perturbation Theory

As discussed in Chapter 2, computational power limits the light sea and valence quark masses that can be used in lattice simulations to unphysically large values. To obtain results at physical masses we need a framework to understand the light mass dependence of the mixing matrix elements. The framework we use is chiral perturbation theory (χPT) [14].

Chiral perturbation theory is an effective theory that describes low energy QCD interactions, where the momentum, p, of the system is such that $p \ll \Lambda_\chi \approx 1$ GeV. It is an expansion in momentum, p, and the pseudoscalar meson masses, about the massless limit of QCD, where the left and right handed degrees of freedom decouple and exact chiral symmetry is obtained. Mesons composed of u, d, and s quarks are the degrees of freedom of χPT, with their fields constructed and combined in such a way as to maintain chiral symmetry.

The main idea behind the construction of χPT is to note that although massless QCD has an $SU(3)_L \times SU(3)_R$ symmetry, in nature, this symmetry breaks down to a $SU(3)_V$ symmetry, where rotations are performed with $L = R$. This is assumed to happen through a process referred to as spontaneous chiral symmetry-breaking ($SCSB$); however, how this occurs is not known. Because there are 16 generators in the original symmetry group, and only 8 generators after $SCSB$, Goldstone's Theorem tells us that there are 8 Goldstone bosons, in this case the pseudoscalar octet $(\pi^+, \pi^-, \pi^0, K^+, K^-, \bar{K}^0, K^0, \eta)$. Because the finite mass term in the QCD lagrangian explicitly breaks chiral symmetry these are pseudo-Goldstone bosons and acquire a small mass. There is however a large mass gap between the pseudoscalar octet and the rest of the hadron spectrum.

It is possible to take advantage of this difference in energy scales for low energy processes by constructing an effective theory for QCD in terms of the low energy degrees of freedom (the pseudoscalar octet). The higher energy degrees of freedom in low energy processes appear local and can be systematically incorporated into the low energy theory as local interaction terms with unknown low energy constants (LECs). The effective (chiral) theory's interaction terms are restricted by Lorentz and chiral symmetry.

By comparing the chiral theory for a process to experimental results for that process it is sometimes possible to determine the unknown LECs. The determined LECs can then be used to make predictions for other low energy processes. χPT is more effective at describing interactions involving only pions since particles containing an s quark are heavier and break the chiral symmetry to a larger degree. This means higher order terms are required to describe processes involving s quarks, complicating the theory and introducing additional LECs that must be determined.

Because the quark masses are an input to a lattice calculation, it is possible to perform the calculation for many sea and valence masses, with the cases where the sea and valence masses are not equal referred to as partially quenched QCD (PQQCD), and the cases where they are equal full QCD. We perform our calculation at 6 sea and 6 valence quark masses in order to extrapolate to the physical quark masses. In addition, the leading order taste violations, which arise at $\mathcal{O}(a^2\alpha_s)$, can be included in the theory and then removed when the extrapolation is performed. This specialized version of χPT, which we use in our calculation, is referred to as rooted staggered χPT.

Section 5.1 discusses general properties of χPT, with the incorporation of heavy quark fields also described. In Section 5.2 an overview of rooted staggered χPT is given. Finally in Section 5.3 the chiral expression of the mixing matrix element, $\langle \bar{B}_q^0 | Q_q^1 | B_q^0 \rangle$, is described.

5.1 Continuum Chiral Perturbation Theory

In the massless limit QCD has a global $\mathrm{SU}(3)_L \times \mathrm{SU}(3)_R$ symmetry, referred to as chiral symmetry, where the lagrangian is separately invariant under rotations of the SU(3) triplets

$$\psi_L = \begin{pmatrix} u \\ d \\ s \end{pmatrix}_L, \quad \psi_R = \begin{pmatrix} u \\ d \\ s \end{pmatrix}_R. \tag{5.1}$$

ψ_L are purely left-handed fields and ψ_R are purely right-handed,

$$\begin{aligned} \psi_L &= \frac{(1-\gamma_5)}{2}\psi \\ \psi_R &= \frac{(1+\gamma_5)}{2}\psi. \end{aligned} \tag{5.2}$$

The chiral effective field theory (EFT) is constructed from the field

$$\Sigma = e^{2i\pi^a \lambda^a / f}, \tag{5.3}$$

where λ^a, $a = 1-8$ are the 8 SU(3) generators, and under a $\mathrm{SU}(3)_L \times \mathrm{SU}(3)_R$ transformation

$$\Sigma \to U_L \Sigma U_R^\dagger, \quad \Sigma^\dagger \to U_R \Sigma^\dagger U_L^\dagger. \tag{5.4}$$

where U_L, U_R are SU(3) matrices.

The explicit form of $\pi^a\lambda^a$ is

$$\frac{1}{\sqrt{2}}\sum_{a=1}^{8} \pi^a \lambda^a = \begin{pmatrix} \frac{1}{\sqrt{2}}\pi^0 + \frac{1}{\sqrt{6}}\eta_8 & \pi^+ & K^+ \\ \pi^- & -\frac{1}{\sqrt{2}}\pi^0 + \frac{1}{\sqrt{6}}\eta_8 & K^0 \\ K^- & \bar{K}^0 & -\frac{2}{\sqrt{6}}\eta_8 \end{pmatrix}. \tag{5.5}$$

The construction of this parametrization is non-trivial and described in Ref. [35]. f is an LEC which can be identified with the pion decay constant f_π. The $\pi^a\lambda^a$ are generically referred to as pion fields in this report.

The lowest order, non-trivial lagrangian constructed from Σ involves two derivatives, or is $\mathcal{O}(p^2)$

$$L_\chi = \frac{f^2}{4}\text{tr}\,(\partial_\mu \Sigma \partial_\mu \Sigma^\dagger). \tag{5.6}$$

The non-linear relationship between the Σ and pion fields gives rise to all possible pion interactions.

Symmetry breaking terms, in this case mass terms, can be introduced by using spurion fields. Mass terms at $\mathcal{O}(m_\pi^2 \sim p^2)$ would take the form $M\Sigma$, which is not invariant under chiral transformations. However, by promoting M to a "spurion" field, and defining it to transform the same as Σ, invariant combinations can be formed. The leading order chiral langrangian is $\mathcal{O}(p^2, m_\pi^2)$,

$$L_\chi = \frac{f^2}{4}\text{tr}\,(\partial_\mu \Sigma \partial_\mu \Sigma^\dagger) - \frac{f^2 B_0}{2}\text{tr}\,(M\Sigma^\dagger + \Sigma M^\dagger), \tag{5.7}$$

where f and B_0 are undetermined LECs, and

$$M = \begin{pmatrix} m_u & 0 & 0 \\ 0 & m_d & 0 \\ 0 & 0 & m_s \end{pmatrix} \tag{5.8}$$

χPT is not a predictive theory, nor is it renormalizable. For every term added to the lagrangian, as is done to include higher order effects, an additional undetermined *LEC* is added.

Expanding Eq. (5.7) in $\pi^a \lambda^a$, tree level relations between pion masses and the quark masses can immediately be seen. For example the charged pion masses have the simple form

$$m_{\pi,ij}^2 = B_0(m_i + m_j), \tag{5.9}$$

where $i, j = u, d, s$. This relation provides a simple instance of how χPT can be used to determine the light-quark mass dependence of non-perturbatively determined quantities: given m_i and m_j and a lattice measurement of $m_{\pi,ij}^2$, B_0 can be determined, and meson masses composed of other quark masses can be extrapolated to. Although it is not predictive it can be used as a quantitative guide.

Technical Aside: Spurions

The spurion "trick" uses the fact that the EFT's mass term breaks chiral symmetry in the same way as the QCD lagrangian's mass term. Including such symmetry breaking terms is therefore consistent with the symmetries of the full theory. By defining the spurion field to transform in a chirally invariant way, it is more straightforward to include all terms (up to the desired order) which involve the spurion field, rather than trying to come up with operators that transform (break the chiral symmetry) the same way as the QCD mass term.

5.1.1 Partially-Quenched Chiral Perturbation Theory

In partially-quenched QCD the light valence and sea quarks have different masses. For χPT to be useful in lattice simulations there must be data at enough different masses so that the LEC's of the chiral expression can be determined. The advantage of using different sea and valence quark masses is that in general it is far more costly to create many ensembles with different sea quark masses than to create many propagators on one ensemble with different valence quark masses.

Using Morel's trick [32] a quantitative connection between full QCD and PQQCD can be defined. This trick introduces commuting spin-1/2 fields, $\tilde{q}_i$ referred to as ghost quarks, with the same masses as the valence quarks, q_{Vi}. The quark fields become

$$Q = (q_{V1}, \ldots, q_{VN_V}, q_{S1}, \ldots, q_{SN}, \tilde{q_{V}}1, \ldots, \tilde{q}_{VN_V}) \tag{5.10}$$

and the masses

$$M = (m_{V1}, \ldots, m_{VN_V}, m_{S1}, \ldots, m_{SN}, m_{V1}, \ldots, m_{VN_V}). \tag{5.11}$$

The QCD action becomes

$$\bar{Q}(\not{D} + M)Q = \sum_{i=1}^{N_V} \bar{q}_{Vi}(\not{D} + m_{Vi})q_{Vi} + \sum_{k=1}^{N_V} \tilde{q}^{\dagger}_{Vk}(\not{D} + m_{Vk})\tilde{q}_{Vk} \tag{5.12}$$
$$+ \sum_{j=1}^{N} \bar{q}_{Sj}(\not{D} + m_{Sj})q_{Sj}$$

and the measure

$$D\bar{Q}DQ = \prod_{i=1}^{N_V} D\bar{q}_{Vi}Dq_{Vi}D\tilde{q}^{\dagger}_{Vi}D\tilde{q}_{vi} \prod_{j=1}^{N} D\bar{q}_{Sj}Dq_{Sj}, \tag{5.13}$$

where N_V is the number of valence quark flavors, N is the number of sea quark flavors, and q_{Sj} are the sea quarks.

The partially quenched generating functional is identical to that of QCD

$$Z_{PQ} = \int DUD\bar{Q}DQe^{-S_{PQ}} \tag{5.14}$$
$$= \int DUe^{-S_{gauge}} \prod_{i=1}^{N_V} \left(\frac{\det(\not{D} + m_{Vi})}{\det(\not{D} + m_{Vi})} \right) \prod_{j=1}^{N} \det(\not{D} + m_{Sj}) = Z_{QCD},$$

as are PQ correlation functions. The additional quark fields are carried over when constructing the χPT. The PQ χPT has a $SU(N_V + N|N_V)$ invariance, where $SU(M|N)$ refers to a graded Lie algebra. Graded Lie algebras differ from standard Lie algebras in that they have commuting and anticommuting elements [37].

5.1.2 Heavy-Light Meson Chiral Perturbation Theory ($HM\chi PT$)

In the infinite mass limit the heavy b quark field can be treated as a static color source. It has a $SU(2)$ spin invariance and the form [29]

$$H_a^Q = \frac{1+\not{v}}{2}(P_{a,\mu}^{*Q}\gamma^\mu - P_a^Q\gamma_5) \tag{5.15}$$

where P_a^{*Q} and P_a^Q annihilate a heavy-light vector and pseudoscalar meson of heavy quark flavor Q and light quark flavor a. The heavy meson momentum is of the form

$$p_\mu = Mv_\mu + k_\mu \tag{5.16}$$

where M is the pseudoscalar meson mass, v_μ the meson velocity, and $k_\mu \ll M$ the "residual" momentum. The general motivation behind a heavy quark effective theory (HQET) is that the heavy quark's mass and velocity are essentially non-dynamical, and all the dynamical information of a process is contained in fluctuations about this mass. Additional interactions can then arise by expanding the lagrangian or operators in powers of $1/M$.

The heavy-light fields transform under a $SU(2)$ spin and $SU(3)$ (or $SU(N_V + N|N_V)$ for PPQCD) light flavor rotation, S and U as

$$H_a^Q \to SH_b^Q U_{ba}^\dagger. \tag{5.17}$$

The leading order lagrangian constructed from these fields and the meson fields is

$$\begin{aligned}\mathcal{L}_{HM\chi PT} = -i\mathrm{tr}_D(\bar{H}_a^Q v_\mu \partial^\mu H_a^Q) + \frac{i}{2}\mathrm{tr}_D(\bar{H}_a^Q v_\mu \xi^\dagger\partial^\mu\xi + \xi\partial^\mu\xi^\dagger]_{ab}H_b^Q) \\ + \frac{i}{2}g\mathrm{tr}_D(\bar{H}_a^Q\gamma_\mu\gamma_5[\xi^\dagger\partial^\mu\xi - \xi\partial^\mu\xi^\dagger]_{ab}H_b^Q) \\ + B_{\eta'}\frac{i}{2}\gamma\mathrm{tr}_D(\bar{H}_a^Q H_a^Q\gamma_\mu\gamma_5)(s)tr[\xi^\dagger\partial^\mu\xi - \xi\partial^\mu\xi^\dagger],\end{aligned} \tag{5.18}$$

where $B_{\eta'} = 0, 1$ for full QCD, PQQCD [12]. $\xi = \sqrt{\Sigma}$ and tr_D is a trace over dirac indices only. $(s)tr$ is the super trace, a version of the trace operation appropriate for graded Lie algebras [37]. The new light field transforms under flavor rotations as

$$\xi \to U_L\xi U^\dagger = U\xi U_R^\dagger. \tag{5.19}$$

The low energy constant, g, is the coupling between a heavy-light pseudoscalar meson, vector meson, and pion in the EFT.

5.2 Rooted Staggered χral Perturbation Theory ($rS\chi PT$)

$rS\chi PT$ is used for processes that contain staggered quarks, in our case Asqtad quarks. The leading order taste changing interactions which occur in Asqtad quarks are incorporated into $rS\chi PT$. The errors then arise as powers of pseudoscalar meson masses, momenta, and the lattice spacing, a. The incorporation of the lattice spacing allows the leading order taste violating effects to be removed. $rS\chi PT$ is a specialized subject

and the derivation and details of it are beyond the scope of this report. Similarly the details of the calculation of the $rS\chi PT$ expression, which was derived by [23], for $\langle \bar{B}_q | Q_q^1 | B_q \rangle$ are not described. A description of the theory is discussed in the following section. Much of the following material is presented in more detail in Refs. [4] and [6].

Symanzik Theory

The construction of any χPT based on lattice QCD actions is similar. The staggered action and its discretization errors will be the focus of this discussion. First the Symanzik action is constructed for QCD to the order in a desired

$$\mathcal{L}^{Sym} = \mathcal{L}_4^{Sym} + a^2 \mathcal{L}_6^{Sym} + \mathcal{O}(a^4). \tag{5.20}$$

In the case of staggered fermions $\mathcal{L}_6^{Sym}$ is composed of four-quark operators, and $\mathcal{L}_4$ is the continuum limit of the staggered action with n staggered quarks, 4 tastes for each flavor, and a heavy quark

$$\mathcal{L}_4^{Sym} = \sum_{i=1}^{n} \bar{q}_j (\not{D} + m_j) + \bar{Q}(v \cdot D) Q + \mathcal{L}_{gauge}, \tag{5.21}$$

where v is the heavy quark velocity. In this case the chiral symmetry, assuming $m_j \to 0$, is $SU(4n)_L \times SU(4n)_R$. $\mathcal{L}_6^{Sym}$ contains 16 operators composed of 5 different spin and taste structures, where the two bilinears in a single four-quark operator contain the same spin and taste structure. The 5 possible dirac or taste structures are $S = 1, V = \gamma_\mu, T = \sigma_{\mu\nu}, A = \gamma_5\gamma_\mu, P = \gamma_5$. 10 of the operators are invariant under separate Euclidean and taste rotations such as

$$[T \times A] \equiv \sum_{\mu<\nu} \sum_{\lambda} \bar{q}_i (\sigma_{\mu\nu} \times \xi_{\lambda 5}) q_i \bar{q}_j (\sigma_{\nu\mu} \times \xi_{5\lambda}) q_j \tag{5.22}$$

and 6 of the operators are invariant only under simultaneous Euclidean and taste rotations such as

$$\begin{aligned} &[T_\mu \times A_\mu] \equiv \\ &\sum_{\mu} \sum_{\mu \neq \nu} \left\{ \bar{q}_i (\sigma_{\mu\nu} \times \xi_{\mu 5}) q_i \bar{q}_j (\sigma_{\nu\mu} \times \xi_{5\mu}) q_j - \bar{q}_i (\sigma_{\mu\nu 5} \times \xi_{\mu 5}) q_i \bar{q}_j (\sigma_{5\nu\mu} \times \xi_{5\mu}) q_j \right\}, \end{aligned} \tag{5.23}$$

where i and j are flavor indices. $[X \times Y]$ indicates matrix X in dirac space and matrix Y in taste space.

Chiral Theory

The chiral theory is then constructed by including all possible operators composed of the HQET and χPT fields that are chirally symmetric, with mass and a^2 factors promoted to spurion fields. There are three four-vectors in the chiral theory: ∂_μ, v_μ, and γ_μ. The power counting works as $p_\pi^2 \sim m_\pi^2 \sim m_q \sim a^2 \ll \Lambda_\chi$. Each ∂_μ in an operator brings a power of p_π and each taste matrix a power of a.

The overall form of the leading order (LO) lagrangian is

$$\mathcal{L}_{LO} = \mathcal{L}_{LO,cont}^{pions} + \mathcal{L}_{LO,a^2}^{pions} + \mathcal{L}_1, \tag{5.24}$$

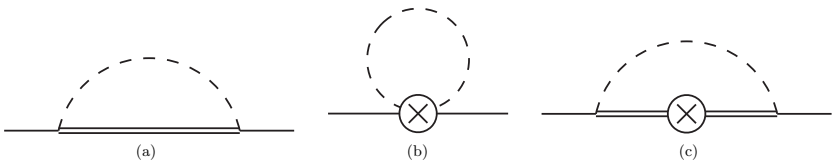

Figure 5.1: Diagrams contributing to the one-loop B mixing chiral expression. Dashed lines are pion propagators, solid lines B meson fields, and double lines B^* meson propagators. The operator is represented as a $\otimes$. (a) is the wave-function renormalization $\mathcal{W}$, (b) the tadpole contribution $\mathcal{T}$, and (c) the sunset diagram $\mathcal{Q}$ [12].

where $\mathcal{L}^{pions}_{LO,cont}$ is Eq. (5.7), $\mathcal{L}_1$ is Eq. (5.18), and $\mathcal{L}^{pions}_{LO,a^2}$ contains the taste changing interactions of the pion fields.

Eq. (5.24) is all that is needed for the calculation of one-loop diagrams. There are however analytic terms in the next-to-leading order NLO (one-loop) chiral expression which are generated by the NLO sector of the lagrangian. These terms arise from inserting spurions for the light-quark mass term and taste volating terms in the heavy-light operators. While the list of such operator is extremely long and their form complicated their effect is simple, and in the case of B mixing they involve just adding the following terms to the chiral expression [23]

$$NLO_{analytic} = L_v m_v + L_s(m_u + m_d + m_s) + L_a a^2. \tag{5.25}$$

L_v, L_s, L_a are unknown LEC's, m_v and m_u, m_d, m_s, are the valence and sea quark masses, and a^2 is the lattice spacing.

This entire procedure must also be done for the quantity (matrix element) being calculated itself: constructing the Symanzik improved operator, building the chiral expression for it, and performing the one-loop integrals using the LO χPT.

An additional detail, the reason the χPT is referred to as rooted, is that anywhere there appears sea quark loops in the calculation we must divide by 4 to reduce the theory from 4+4+4 to 1+1+1. This corresponds to the step in the full theory where the square root or fourth root of the determinate is taken to remove the extra tastes.

5.3 The Chiral Expression for $\langle \bar{B}^0_q | Q^1_q | B^0_q \rangle$

Using the methods described above a chiral expression for the B mixing matrix element was constructed by Jack Laiho and Ruth van der Water [23]. They adapted results from a paper by Detmold and Lin [12], which calculated the expression for the partially quenched continuum case, to the staggered theory. The exact expression can be found in Appendix B.

The diagrams contributing to the NLO expression are shown in Fig. 5.1. The $rS\chi PT$ expression has the following form at NLO [23],

$$\begin{aligned} &\left\langle \bar{B}_q | Q^1_q | B_q \right\rangle_{QCD} = \frac{8}{3} m^2_{B_q} f^2_{B_q} B_q = m_{B_q} \left\langle \bar{B}_q | Q^q_1 | B_q \right\rangle_{HQET} = \\ &m_{B_q} \beta \left[1 + (\mathcal{Q}_q + \mathcal{W}_q + \mathcal{T}_q) + L_v m_q + L_s(2m_L + m_h) + L_a a^2 \right], \end{aligned} \tag{5.26}$$

where β, f, L_v, L_s, and L_a are low energy constants to be determined from fitting to the lattice data. m_q, m_L, and m_h denote the light valence, light sea, and strange sea quarks respectively. The light sea quarks are treated as degenerate, where the isospin average is used, $m_L = \frac{m_u+m_d}{2}$. For staggered quarks the taste-nonsinglet pseudoscalar meson masses are split

$$M^2_{ij,\xi} = \mu(m_i + m_j) + a^2\Delta_\xi, \tag{5.27}$$

where m_i, m_j are quark masses and the sixteen meson masses are labeled by their taste representation, $\xi = P, A, T, V, I$. The parameters $f \sim f_\pi \approx 130MeV$, μ, and Δ_ξ's are determined from lattice calculations for pions and kaons [5]. $g^2_{B*B\pi}$ is constrained by the CLEO measurement, $g^2_{D*D\pi} = 0.35 \pm 0.14$, which from heavy quark symmetry implies $g^2_{B*B\pi} \approx g^2_{D*D\pi}$. In the actual fits all dimensionful parameters are made dimensionless by multiplication of appropriate powers of r_1 as explained in Chapter 6.

The chiral logs, $\mathcal{X}_q = \mathcal{T}_q$, $\mathcal{W}_q$, $\mathcal{Q}_q$, due to the tadpole, wavefunction renormalization, and sunset diagrams respectively, each have a similar structure,

$$\mathcal{W}_q = -\frac{3g^2_{B*B\pi}}{16\pi^2 f^2}\left\{\frac{1}{16}\left[\sum_{\Xi=I,P,4V,4A,6T}\bar{h}^q_\Xi\right] + \frac{1}{3}h^q_I + a^2(\delta'_V h^q_V + \delta'_A h^q_A)\right\}, \tag{5.28}$$

$$\mathcal{T}_q = -\frac{1}{16\pi^2 f^2}\left\{\frac{1}{16}\left[\sum_{\Xi=I,P,4V,4A,6T}\bar{h}^q_\Xi + \bar{I}_\Xi\right] + \frac{2}{3}h^q_I + a^2(\delta'_V h^q_V + \delta'_A h^q_A)\right\},$$

$$\mathcal{Q}_q = \frac{3g^2_{B*B\pi}}{16\pi^2 f^2}\left\{\frac{1}{16}\left[\sum_{\Xi=I,P,4V,4A,6T}\bar{I}^q_\Xi\right] + \frac{1}{3}h^q_I\right\}.$$

I, P, V, A, and T refer to the taste multiplet from which the meson masses appearing in the logs are from. Their complete form is given in Appendix B. In the continuum limit $\bar{h}_\Xi$, $\bar{I}_\Xi$, and h_I combine to form the continuum perturbation theory, and the taste violating terms h_V and h_A are set to 0. The prior values and widths for δ'_V and δ'_A are also determined from lattice calculations for pions and kaons. Next-to-next-to-leading order ($NNLO$) analytic terms are also included in our fits, with priors and constraints estimated from chiral perturbation theory.

When extrapolating to the physical results we set $\Delta_\xi = \delta'_{A,V} = a = 0$, $m_L \to (m_u + m_d)/2$, and $m_h \to m_s$. We then obtain $\langle\bar{B}^0_d|Q^1_d|B^0_d\rangle$ and $\langle\bar{B}^0_s|Q^1_s|B^0\rangle$ by setting $m_q \to m_d$ or m_s.

The ratio ξ can be extracted by first determining $f_{B_s}\sqrt{B_{B_s}}$ and $f_{B_d}\sqrt{B_{B_d}}$, then forming the ratio. However, the leading discretization errors and some of the statistical errors can be removed by forming the ratio first and then performing the chiral fits. The fits have been done both ways as described in Chapter 6.

Eq. (5.26) is similar to the leptonic heavy-light decay constant expression presented in Ref. [4], which is currently used by the Fermilab Lattice and MILC collaborations in the chiral fits to f_{D^+}, f_{D_s}, f_B and f_{B_s}. In particular, the wave function renormalization, W_q, should just be twice its value in the decay constant expression. The tadpole diagram terms, T_q, are similar to the corresponding terms in the decay constants. The sunset diagram term, Q_q, has no analogue in the decay constant case, but is composed of functions present in the wavefunction renormalization and tadpole diagrams. This similarity is worth noting because it allowed us to check the long and complicated functions composing Eq. (5.26) against the decay constant expression,

which we have previously independently coded and used to successfully reproduce the Fermilab Lattice and MILC collaborations' results.

There is an independent χPT for the bag parameters B_{B_q}. The chiral behavior of B_{B_q} is milder than for Q_q^1, and the χPT simpler [23]

$$B_{B_q} = \frac{3}{8}\kappa\left[1 - \mathcal{X}_q\right] \tag{5.29}$$

where

$$\mathcal{X}_q = \frac{(1 - 3g_\pi^2)}{16\pi^2 f_\pi^2}\left\{\left[\frac{1}{16}\sum_{\Xi=I,P,4V,4A,6T}\bar{I}_\Xi^q\right] + h_I^q\right\}. \tag{5.30}$$

Although the bag parameter is not by itself a phenomenologically interesting quantity it is useful to have as a consistency check, where f_B and f_{B_s} results can be combined with the bag parameter results, and final values for the mixing parameters compared.

$NNLO$ Analytic Terms

An additional consideration is that NLO χPT is questionably valid when the strange quark is included. It would be desirable to include $NNLO$ contributions to test the validity of the NLO expression. The effort needed to calculate the $NNLO$ logs is prohibitive, and in fact there is an argument that just including the $NNLO$ analytic terms may be adequate to incorporate the strange quark. The NNLO contributions from the u and d quarks are known to be negligible, as they should be since χPT works very well at these low energies. The masses of mesons composed of s quarks are large enough that the logs containing them are approximately analytic. Thus just including the $NNLO$ analytic terms should approximate the full NNLO expression to a high degree.

Chapter 6

Chiral Fits

In this chapter the chiral fits to our data for $\langle \bar{B}_q | Q_q^1 | B_q \rangle$, using the expression defined in Chapter 5, Eq. 5.26, are presented. The parametrization of the chiral expression we use in the fits is first discussed. This is followed by a description of the general fitting procedure. Variations of the fit Ansatz are then considered and the method for determining the preferred fit discussed. Finally the systematic errors that arise in our fitting procedure are discussed and estimated. Preliminary chiral fit results for B_{B_d} and B_{B_s} are also presented.

The plots, extrapolations/interpolations, and results presented in this section for β_d and β_s are not final. The important perturbative matching coefficients have not been incorporated into the fits because their results are not finalized. This could change the values for β_d and β_s by up to 5%. The effect of the matching will only shift the values of the matrix elements, and thus all methods presented here will be valid for the "final" analysis. The values for ξ are not expected to change more than 1%, and results for this quantity can be considered finalized as presented.

6.1 Parametrization of the Chiral Expression

Determining the Lattice Scale: r_1

Fitting to lattice correlation functions can extract masses and other dimensionful quantities in units of the lattice spacing. To convert these quantities to their physical values the lattice spacing a must be determined from some other dimensionful quantity who's value is known. The quantity we use is r_1 defined as

$$r_1^2 \frac{d}{dr_1} V(r_1) = 1.0, \tag{6.1}$$

where $V(r_1)$ is the static quark potential. The values for r_1/a on every MILC ensemble used in our calculation has been measured and are presented in Ref. [5] and listed in Table 6.1. The physical value for r_1 determined from continuum extrapolations is $r_1^{phys} = 0.318(7)$. In our chiral fits all parameters are first converted to units of r_1 by multiplying by the appropriate r_1/a, giving extrapolated results for β_d and β_s in units of r_1^{phys}. The scale, r_1^{phys}, has a 2.2% uncertainty which must be accounted for in the systematic error analysis.

Taste Violating Terms

Ratios of taste violating terms are used as input into the fits rather than the lattice spacing. The dominant taste violations are expected to be $\mathcal{O}(a^2\alpha_s^2)$ because the

$\mathcal{O}(a^2\alpha_s)$ effects are suppressed in Asqtad quarks. The ratio on the fine lattice is

$$A^2_{0.09} \equiv \frac{(\alpha_S^2 a^2)_{fine}}{(\alpha_S^2 a^2)_{coarse}} \sim 0.35 \tag{6.2}$$

and on the medium coarse is

$$A^2_{0.15} \equiv \frac{(\alpha_S^2 a^2)_{medium\,course}}{(\alpha_S^2 a^2)_{coarse}} \sim 1.607. \tag{6.3}$$

The coarse lattice taste violating parameters are normalized to 1, $A^2_{0.12} = 1$.

Pion and Quark Mass Parametrization

In our fits the analytic terms in the chiral expression are written in terms of the pseudo-scalar pion masses

$$r_1^2 m_{ij}^2 = r_1^2 \mu(m_i + m_j). \tag{6.4}$$

(For notational convenience factors of r_1 will be suppressed in further expressions, and can be deduced by dimensional considerations). The purpose of the above parametrization is to better absorb shifts in the chiral scale Λ_χ, in other words to lessen the fit results' dependence on the chiral scale. A shift in the chiral scale, $\Lambda_\chi \to \tilde{\Lambda}_\chi$, causes the logs to transform as

$$m_{ij}^2 \log(m_{ij}^2/\Lambda_\chi^2) \to m_{ij}^2 \log(m_{ij}^2/\Lambda_\chi^2) - m_{ij}^2 \log(\tilde{\Lambda}_\chi^2/\Lambda_\chi), \tag{6.5}$$

with factors of the pion masses multiplying the terms introduced by the shift. The LECs in front of the corresponding analytic terms, in the above case $L_{ij} m_{ij}^2$, shift their values to accommodate this change, and if the analytic terms are directly proportional to the terms arising from the shift this "absorption" of scale is more direct. Of course Eq. (6.5) is a simplification because there is the additive shifts due to taste splittings, $a^2\Delta_\Xi$, in the non-pseudo-scalar taste mesons that would also be in the new terms. Ideally a parametrization such as in Ref. [4] which accounts for the a^2, taste violating terms would be used; however, we have attempted this and it is not possible in the chiral expression for $\langle \bar{B}_q | Q_q^1 | B_q \rangle$. In particular the LEC $g_{BB^*\pi}$ is mixed into the shift dependent terms, reducing the stability and increasing the errors in the fits.

Final Parametrization of the Chiral Expressions

The NLO expression for β_q, with the same parametrization as what is used in the fits is

$$\begin{aligned} \beta_q &= \sqrt{\frac{3}{8}\langle \bar{B}_q | Q_q^1 | B_q \rangle / m_{B_q}} = \\ &\beta \left[1 + \frac{1}{2}(\mathcal{Q}_q + \mathcal{W}_q + \mathcal{T}_q) + L_v m_{qq}^2 + L_s(2m_{LL}^2 + m_{hh}^2) + L_a A_a^2 \right], \end{aligned} \tag{6.6}$$

where the 7 $NNLO$ analytic terms

$$\begin{aligned} &Q_1 m_{qq}^4,\ Q_2(2m_{LL}^2 + m_{hh}^2)^2,\ Q_3 m_{qq}^2(2m_{LL}^2 + m_{hh}^2), \\ &Q_4(2m_{LL}^4 + m_{hh}^4),\ P_1 A_a^2 m_{qq}^2,\ P_2 A_a^2(2m_{LL}^2 + m_{hh}^2),\ P_3 A_a^4 \end{aligned} \tag{6.7}$$

$a(fm)$	Volume	m_L/m_h	N_{confs}	am_q	r_1/a
0.15	$16^3 \times 48$	0.2	631	0.0048, 0.007, 0.0097, 0.0194, 0.29,0.0484	2.133878
0.15	$16^3 \times 48$	0.4	631	0.0048, 0.007, 0.0097, 0.0194, 0.29,0.0484	2.128982
0.15	$16^3 \times 48$	0.6	440	0.0048, 0.007, 0.0097, 0.0194, 0.29,0.0484	2.126103
0.12	$24^3 \times 64$	0.1	529	0.005, 0.007, 0.01, 0.02, 0.03, 0.0415	2.645042
0.12	$20^3 \times 64$	0.14	833	0.005, 0.007, 0.01, 0.02, 0.03, 0.0415	2.634559
0.12	$20^3 \times 64$	0.2	592	0.005, 0.007, 0.01, 0.02, 0.03, 0.0415	2.619101
0.12	$20^3 \times 64$	0.4	460	0.005, 0.007, 0.01, 0.02, 0.03, 0.0415	2.650860
0.09	$28^3 \times 96$	0.2	557	0.0031, 0.0044, 0.062, 0.0124, 0.0272, 0.031	3.701264
0.09	$28^3 \times 96$	0.4	534	0.0031, 0.0042, 0.062, 0.0124, 0.0272, 0.031	3.721383

Table 6.1: Ensembles on which two and three-point functions were calculated. Three different lattice spacings were used, with 6 different light valence quark masses on each.

are included/excluded as indicated for a particular fit. Q_{1-4} and P_{1-3} are the LECs for the $NNLO$ terms. The NLO expression for B_{B_q} is

$$B_{B_q} = \frac{3}{8}\kappa\left[1 - \mathcal{X}_q\right] \tag{6.8}$$

with the $NNLO$ analytic terms

$$L_v m_{qq}^2 + L_s(2m_{LL}^2 + m_{hh}^2) + L_a A_a^2. \tag{6.9}$$

The NLO expression for B_{B_q} has only two fit parameters, β and g_π, and thus fits to it are extremely straightforward. In fact the continuum ratio $\sqrt{B_{B_s}/B_{B_d}}$ is completely determined at NLO for a given value of g_π. The ratio varies weakly with the poorly known parameter g_π, and so evaluating it using a conservative range of values for g_π, combined with the ratio f_{B_s}/f_B, provides a first guess at ξ.

It is also useful to consider the ratio of chiral expressions β_s/β_q, where m_s is the strange quark mass on a particular ensemble

$$\xi' = \frac{\beta_s}{\beta_q} = 1 + \frac{1}{2}(\mathcal{Q}_s + \mathcal{W}_s + \mathcal{T}_s - \mathcal{Q}_q - \mathcal{W}_q - \mathcal{T}_q) + L_v(m_{ss}^2 - m_{qq}^2). \tag{6.10}$$

Many of the fit parameters in ξ' are canceled, improving the stability of the fits. Also, there are discretization errors of $\mathcal{O}(\alpha_s\Lambda_{\rm QCD}/M, (\Lambda_{\rm QCD}/M)^2)$ from the heavy-quark action which are not included in the chiral perturbation theory which partially cancel in the ratio.

The fits are performed on the ensembles and valence masses listed in Table 6.1.

6.2 Chiral Fitting Procedure, Priors and Inputs

We first create bootstrap measurements of $\beta_q = \sqrt{\frac{3}{8}\langle\bar{B}_q|Q_1^q|B_q\rangle/m_{B_q}} = f_{B_q}\sqrt{m_{B_q}B_{B_q}}$ for each sea and valence quark mass combination from the two and three-point correlator fits. The bootstrap data is then fit to the chiral expression. We use Peter Lepage's Bayesian `python` χ^2 minimization routine, just as in the correlator fits. All bootstrap measurements from the same sea quark ensemble have the same random number seed, ensuring that the bootstrap measurements for different valence quarks

within an ensemble are based on the same configurations, and therefore are properly correlated. The fits are simultaneously performed to all included ensembles. It was seen that 300 bootstrap samples was sufficient to obtain a Gaussian distribution in the bootstrap ensembles. In the following fits 500 bootstrap samples were used. The same fit methods as were described for the correlators is used in these fits.

The input and fit parameters are set as in Table 6.2. The prior widths are based on a simple power counting argument, where the NLO analytic terms should be of similar magnitude to the NLO logs, which are $\sim s \equiv \frac{m_\pi^2}{8\pi^2 f_\pi^2}$, and the $NNLO$ terms that magnitude squared. The parameters were determined in Refs. [5] and priors and prior widths by discussions with [39]. f_π is determined from experiment.

Fit parameters	Prior Value	Prior Width
β	1	1
g_π^2	0.35	0.14
Medium Coarse		
$r_1^2a^2\delta'_V$	-0.0495×1.607	0.023×1.607
$r_1^2a^2\delta'_A$	-0.2965×1.607	0.0095×1.607
Coarse		
$r_1^2a^2\delta'_V$	-0.0495	0.023
$r_1^2a^2\delta'_A$	-0.2965	0.0095
Fine		
$r_1^2a^2\delta'_V$	-0.0495×0.35	0.023×0.35
$r_1^2a^2\delta'_A$	-0.2965×0.35	0.0095×0.35
L_v	0	s
L_s	0	s
L_a	0	s
Q_{1-4}	0	s^2
P_{1-3}	0	s^2
Input parameters	Value	
$f_\pi r_1$	0.2106	
$\Lambda_\chi r_1$	1.6-2.6	
Medium Coarse		
μr_1	6.432069	
Coarse		
μr_1	6.234000	
Fine		
μr_1	6.381592	
Taste Splittings	Value	
Medium Coarse		
$r_1^2a^2\Delta_P$	0	
$r_1^2a^2\Delta_V$	0.3505897	
$r_1^2a^2\Delta_T$	0.5551778	
$r_1^2a^2\Delta_A$	0.7213114	
$r_1^2a^2\Delta_I$	0.8965017	
Coarse		
$r_1^2a^2\Delta_P$	0	
$r_1^2a^2\Delta_V$	0.4391099	
$r_1^2a^2\Delta_T$	0.3268607	
$r_1^2a^2\Delta_A$	0.2052872	
$r_1^2a^2\Delta_I$	0.5369975	
Fine		
$r_1^2a^2\Delta_P$	0	
$r_1^2a^2\Delta_V$	0.152371	
$r_1^2a^2\Delta_T$	0.115382	
$r_1^2a^2\Delta_A$	0.0706188	
$r_1^2a^2\Delta_I$	0.206207	

Table 6.2: Fit parameters' priors and input parameters. The parameters were determined in Refs. [5] and priors and prior widths by discussions with [39]. f_π is determined from experimental values. $s = \frac{1}{8\pi^2(f_\pi r_1)^2} = 0.285$

6.3 Chiral Fits and Extrapolations

In this section the chiral fits to Eq. (6.6), including various $NNLO$ terms are explored and discussed. Some general characteristics of the lattice data are:

- The statistical errors of the data tend to decrease with increasing valence and sea quark mass
- The statistical errors tend to increase with lattice spacing
- The sea quark mass dependence is much more mild than the valence quark mass dependence
- The lattice spacing and sea quark mass dependence in the ratio $\xi' = \beta_s/\beta_q$ and B_{B_q} is mild as expected from the χPT.

There are also general characteristics of the chiral fits that are worth noting:

- Good χ^2 are obtained at NLO. $SU(3)$ χPT is not expected to work well at NLO, suggesting that the statistical errors of the data are large enough that the usefulness of χ^2 as a "goodness of fit" measure may not be adequate. Therefore the determination of the proper fit Ansatz is not trivial, and a variety of fits must be tried. The quality of the fits are judged by how well they follow the lattice data, and whether they give physically reasonable results.
- The medium coarse data appears to have discretization errors that are too large to be used in the final analysis. The reasons we believe this are described in the following section.
- The most phenomenologically crucial parameter, ξ', can be determined two ways. The first is by extrapolating to β_d and β_s separately, and then forming the ratio, $\xi' = \beta_s/\beta_d$. An alternative method is to first form the ratio β_s/β_q from each lattice data point of valence quark mass m_q. The ratios are then fit to the simpler chiral expression in Eq. (6.10), and the extrapolation performed. We refer to the former method as the indirect method, and the latter as the direct method.

6.3.1 Medium Coarse Data: Too Coarse?

This section will describe why the medium coarse data is not used for the final analysis. Similar considerations have been made in the Fermilab Lattice and MILC collaborations' determination of f_B and f_{B_s}.

The medium coarse data has large statistical errors compared to the coarse or fine data. The coarse and fine data have statistical errors ranging from $2-5\%$, while the medium coarse data's statistical errors range from around $5-10\%$, and up to 20% in some cases! The largest of the errors are due to what we refer to as outliers. These are data points that lie far beyond the physically reasonable range of values. They are typically due to the first excited state mass and or amplitude getting switched with the ground state mass or amplitude in the correlator fits. Through careful choice of correlator priors and fit parametrization the number of 5σ outliers in the lattice data, which containts $500(samples/valence) \times 6(valence/ensemble) \times 9(ensembles) = 27000 samples$ has been reduced to 26, and the number of 10σ outliers to 13. Almost all of the 10σ outliers are from within the medium coarse ensemble data. Outliers are

clearly bad for the fits because the assumption of an approximate gaussian distribution to the data is no longer valid, and the fitter does not have to be close to the central value of the data points to obtain a good χ^2. That said, removing the outliers has no firm statistical basis and we choose not to remove any in this analysis but rather drop the medium coarse ensembles.

The increase in errors with lattice spacing is due to the rapidly declining signal with t_1, t_2 and t in the three- and two-point correlators. Because the same time slice on different lattices correspond to different physical times, the correlator decays and loses information more rapidly per timeslice as the lattices become coarser. This results in having less statistical power in the correlator fits, and in the medium coarse case the data is noisy enough to allow many outliers into the bootstrap ensembles.

In addition to the medium coarse data being much noisier than the coarse and fine lattices, it seems to have discretization errors that are too large. The errors are formally $\mathcal{O}(a^2, a\alpha_s)$, (or $\mathcal{O}((\Lambda_{\rm QCD}/M)^2, \alpha_s\Lambda_{\rm QCD}/M)$ in the language of the Fermilab interpretation), but α_s is likely not small enough for perturbation theory to work well, meaning the power suppression is less reliable.

To see this effect consider the chiral fit and extrapolation in Fig. 6.1, where the sea quark mass plane is shown and all $NNLO$ analytic terms are included. It can be seen that the fit lines follow the data reasonably well. What is strange is that the medium coarse data is closer to the fine data than the coarse data. What's even more disconcerting is that the medium coarse fit line is closer to the continuum extrapolation than either the coarse or fine in the extrapolation to β_d. This suggests counterintuitively that the discretization errors in medium coarse data are smaller than the less coarse ensembles. For the above reasons we leave out the medium coarse ensembles in the chiral fits presented in the rest of this chapter and used in our final analysis.

6.3.2 Fits and Extrapolations: Choosing an Anszatz

All fit results for β_d, β_s, and ξ' are listed in Table 6.3. The fit variations and extrapolations are plotted in Figs. 6.2-6.13. The plots are shown in either the sea mass plane or valence mass plane. The data along a fit curve in the sea mass plane are just the uncorrelated data points, which helps judge the quality of the fit. In the valence mass plots all data are shown, and data along a fit curve are from the same ensemble and thus correlated.

In the sea mass plots data are plotted versus the pseudoscalar pion mass composed of the light sea quarks, $m_\pi = \mu(m_L + m_L)$. The different line and point colors correspond to the lattice spacings used in the fit. The circles are full QCD points, where $m_q = m_L$, and the solid curves through them of the same color are the fit curves. An extrapolation of the solid curves gives the solid red curve and β_d. The $\times$s are the data where $m_q = m_s$ at the same points as the full QCD points, where m_s is an ensemble's s quark mass, and the dashed curves through them are the fits. An extrapolation/interpolation of the dashed curves gives the dashed red curve and β_s. The diamonds are there as reference only: they are the data points plotted at the s valence quark mass and give a sense of the data's mild sea mass dependence.

In the valence mass plots data are plotted versus the pseudoscalar pion mass composed of the light valence quark. The circles in these plots correspond to the coarse lattice data, and the squares to the fine lattice data, with different ensembles

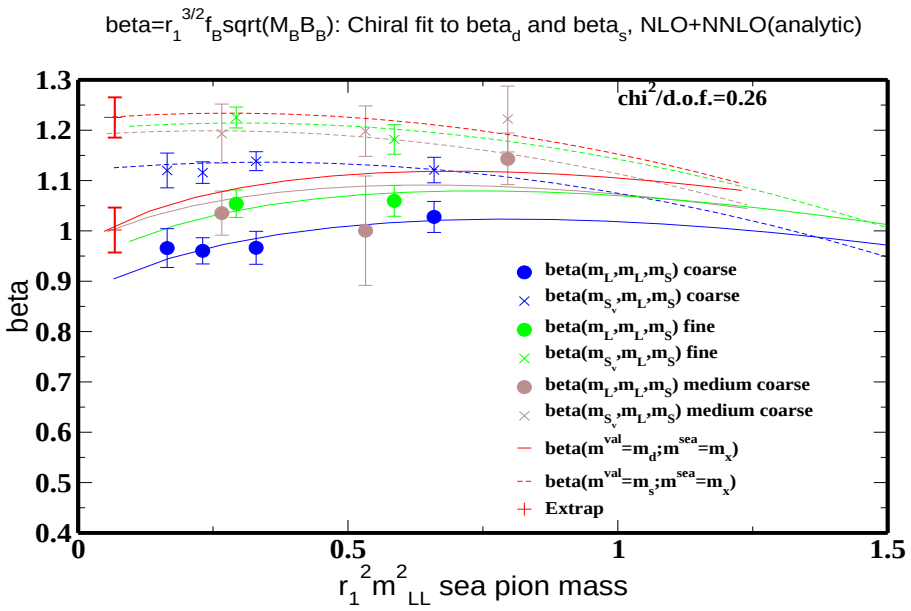

Figure 6.1: . Fit to all ensembles and extrapolation using all NNLO analytic terms. The plots is presented in the sea mass plane, where data is plotted versus the pseudo-scalar pion mass composed of the light sea quarks, $m_\pi = \mu(m_L + m_L)$. The 3 different line and point colors correspond to the 3 lattice spacings used in the fit. The circles are full QCD points, where $m_q = m_L$, and the solid lines through them of the same color are the fit lines. An extrapolation in of the solid lines give β_d. The $\times$s are the data where $m_q = m_s$ at the same points as the full QCD points, where m_s is an ensembles s quark mass, and the dashed lines through them are the fits. An extrapolation in the dashed lines gives β_s.

and their fit lines distinguished by their color. The extrapolation/interpolation curve is shown in red. It can be seen in these plots that the extrapolation curve is steeper than the fit curves. This is due to the taste violations present in the logarithms of the staggered chiral expression, which are removed in the extrapolation.

As mentioned in the introduction we obtain fits with good χ^2s at NLO as shown in Fig. 6.2-6.5. The fit to β_d and β_s follows the data quite well, and the extrapolations look physically reasonable. The only exception is the fit to the light masses of the 0124/031 ensemble as can be seen in Fig. 6.3. The direct fit to ξ' also follows the data well in the sea quark mass plane, Fig. 6.4, and has the same χ^2 as the fits to β_d and β_s. The same direct fit shown in the valence mass plane, Fig. 6.5, misses a lot of the data points in the 020/050 and 0124/031 ensembles. The χ^2 is evidently not a great measure of the quality of the fit. This behavior is seen in the chiral fits of the Fermilab Lattice and MILC collaborations to other quantities involving the b quark and is due to the large statistical errors in the correlators.

With behavior such as this, our only option is to choose our preferred fit by eye. While not a quantitative procedure, as long as we are honest about the size of the difference in the various fit Ansatzs and take the ranges of values produced by the various Ansatzs, we should obtain a good estimate of the total systematic error due to the Ansatz. This error is hopelessly entangled with the light quark discretization effects

and so the two errors are lumped together and referred to as chiral fit systematics. We compare the quality of the NLO fits to variations of the $NNLO$ fits to determine a central value and systematic error due to the fit Ansatz.

Figs. 6.6-6.9 show the same plots as Figs. 6.2-6.5, but with all $NNLO$ analytic terms included in the fit. If we assume the very low χ^2s have any meaning, the $NNLO$ fits have a significantly lower χ^2. Indeed visual inspection suggests these fits follow the data better, as is especially obvious in the ξ' fits in Figs. 6.8-6.9. The chiral extrapolation for ξ' is also milder in the $NNLO$ case, in accordance with the chiral expression's predictions.

All combinations of Ansatz have been tried in this analysis, and all have good χ^2 and follow the data at least as well as the NLO fits. In light of this, choosing to include or exclude particular $NNLO$ terms, formerly of the same order, for the preferred fit introduces a degree of arbitrariness into the extrapolation results. Therefore we choose the Ansatz where all $NNLO$ terms are included to obtain our central values. The fit with only a Q_3 $NNLO$ term, the valence mass sea mass cross term, provides a lower limit on the range of fit results. Plots of these fits are shown in Figs. 6.10-6.13. The NLO fits provides an upper limit on the results.

The preferred fit and most extreme fit results are listed in Table 6.3. The systematic error due to the Ansatz variation is listed in the last row of Table 6.3. Evidently the determination of β_s is extremely insensitive to the fit Ansatz, and the variation in ξ' over fit Ansatz is due to the variation in β_d.

In Fig. 6.14 the preliminary $NNLO$ chiral fit and extrapolation for B_{B_d} and B_{B_s} is shown. The results for the bag parameters are shown in Table 6.4. They are insensitive to any change in the fit Ansatz.

Ansatz	$\chi^2/d.o.f.$	ξ' Direct	ξ' Indirect	β_d	β_s
$NNLO$	0.25	1.212(41)	1.215(38)	1.006(41)	1.222(34)
NLO	0.43	1.251(10)	1.250(13)	0.982(29)	1.227(30)
Q_3	0.23	1.175(20)	1.181(33)	1.031(38)	1.218(30)
Chiral fit systematics error		3.1%	2.8%	2.5%	0.4%

Table 6.3: Direct fit results, coarse and fine ensembles only. Errors in parentheses are 68% bootstrap confidence intervals. The fit Ansatz in red, where all NNLO terms have been include, is used as the central value fit. The NLO and $NLO + Q_3$ Ansatz give the most extreme values for the mixing parameters and are used to determined the chiral fit systematics.

	$\chi^2/d.o.f.$	B_{B_s}/B_{B_d}	B_{B_d}	B_{B_s}
$NNLO$	0.20	1.021(26)	0.881(22)	0.899(20)

Table 6.4: Direct fit results, coarse and fine ensembles only for the bag parameters.

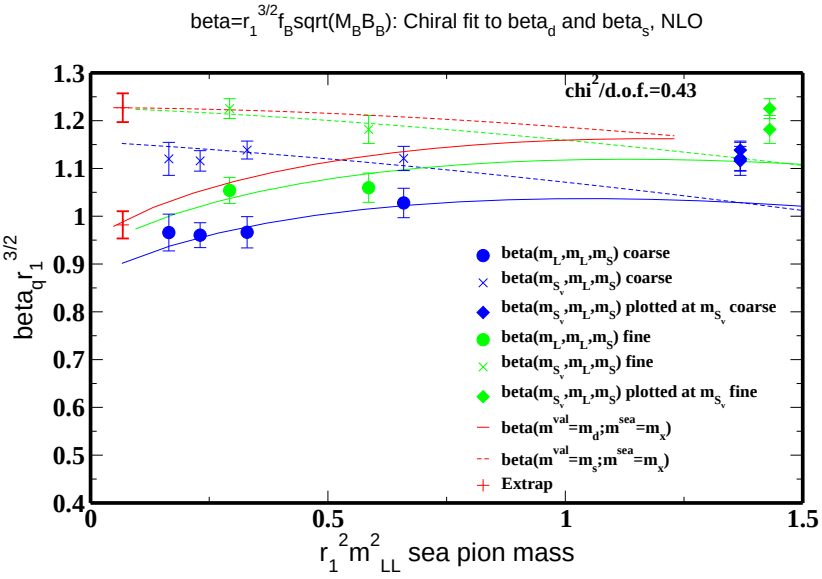

Figure 6.2: *NLO* fit plotted in sea quark mass plane. The fit lines follow the data well. The data points in the upper right corner are for reference only and are not being fit to.

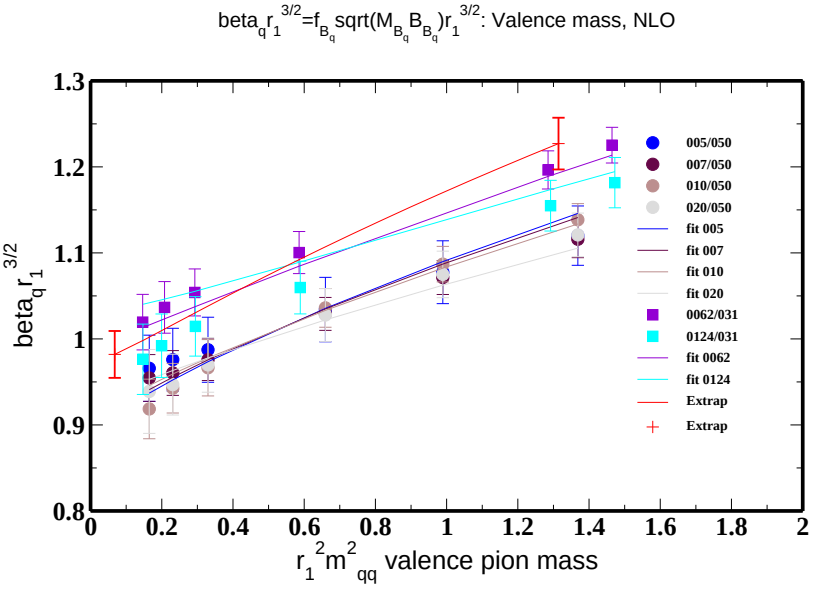

Figure 6.3: *NLO* fit, plotted in valence pion mass plane, defined the same as the sea pion mass in Fig. 6.1 but with $m_L \to m_q$. All mass points are shown.

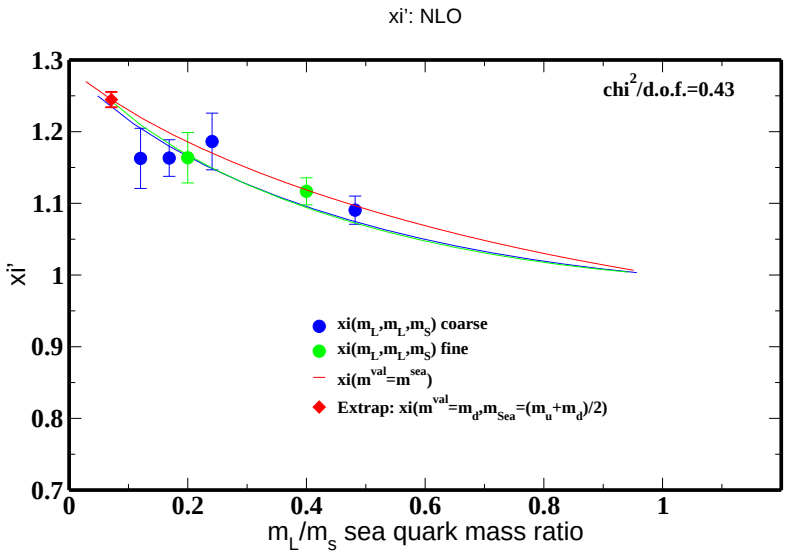

Figure 6.4: *NLO* fit plotted in sea quark mass plane. The fit lines follow the data well.

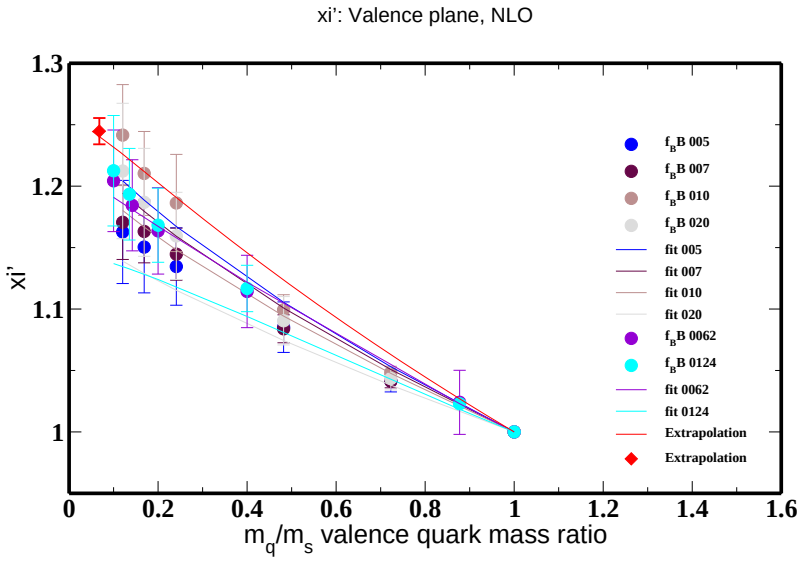

Figure 6.5: *NLO* fit, plotted in valence mass plane. All mass points shown.

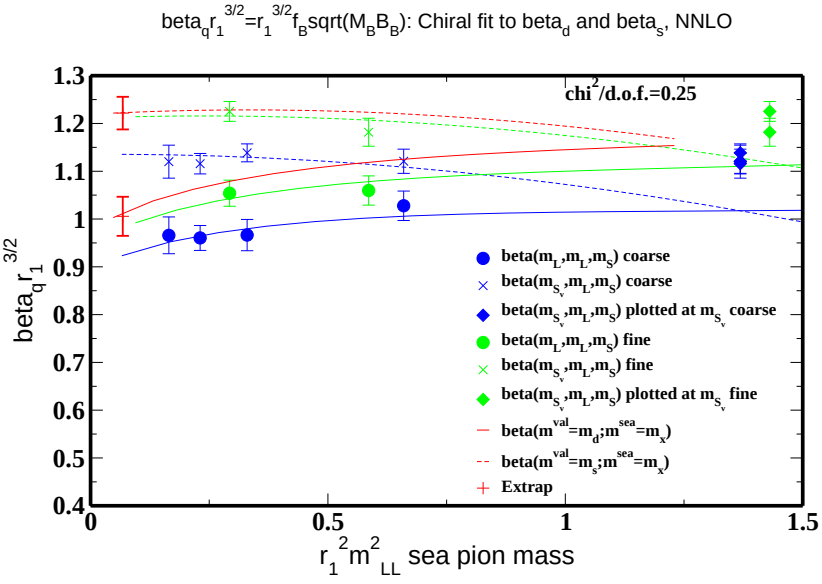

Figure 6.6: *NNLO* fit plotted in sea quark mass plane. The fit lines follow the data well.

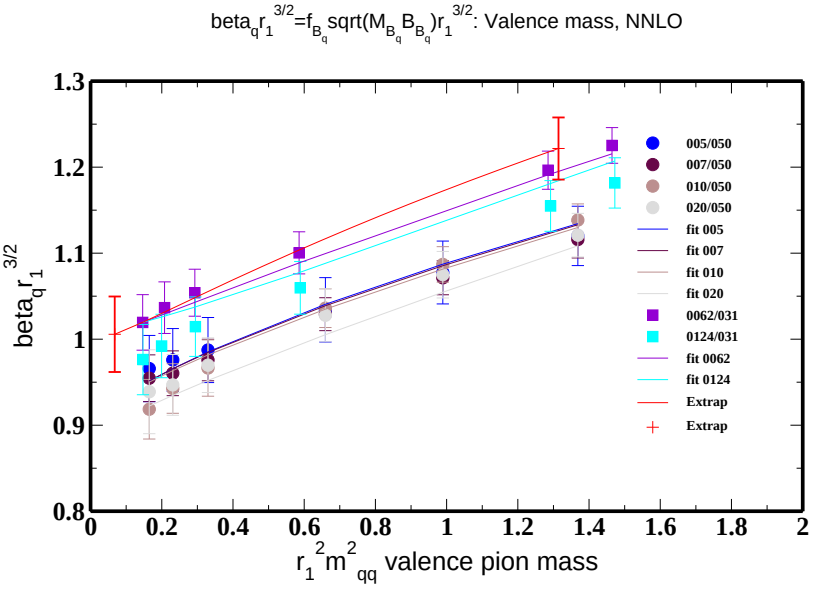

Figure 6.7: *NNLO* fit, plotted in valence mass plane. All mass points shown.

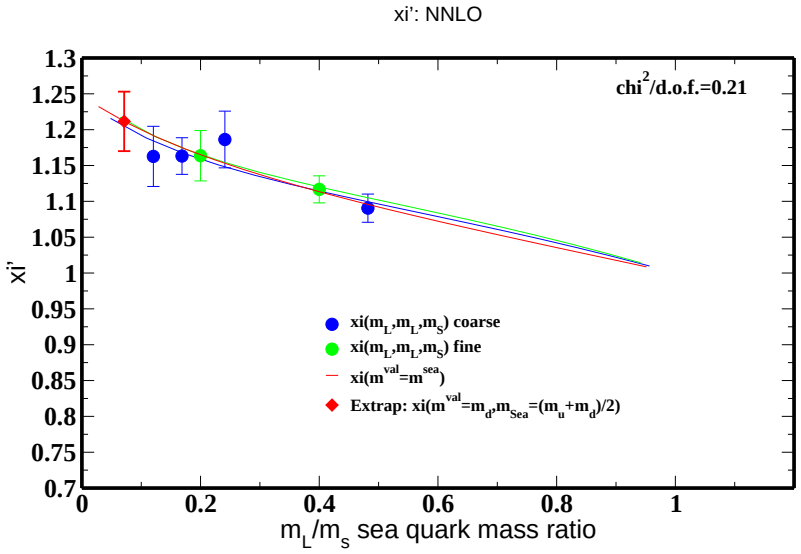

Figure 6.8: *NNLO* fit plotted in sea quark mass plane. The fit lines follow the data well.

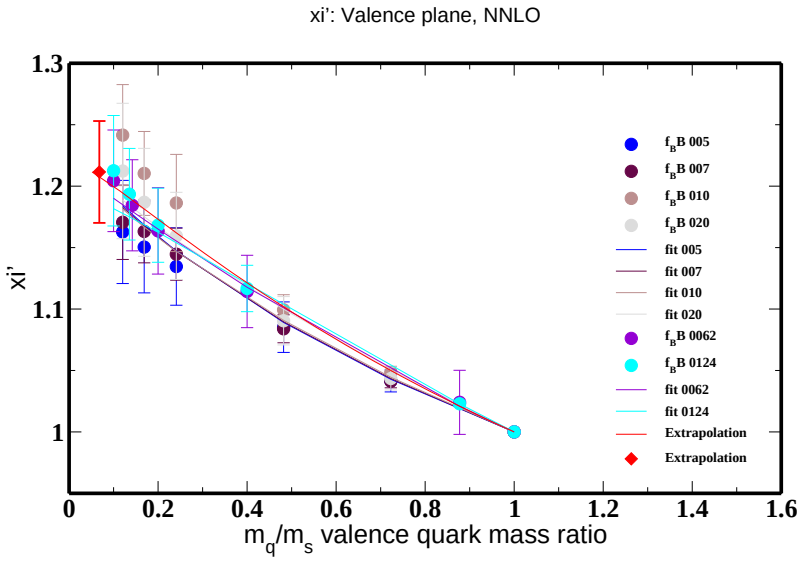

Figure 6.9: *NNLO* fit, plotted in valence mass plane. All mass points shown.

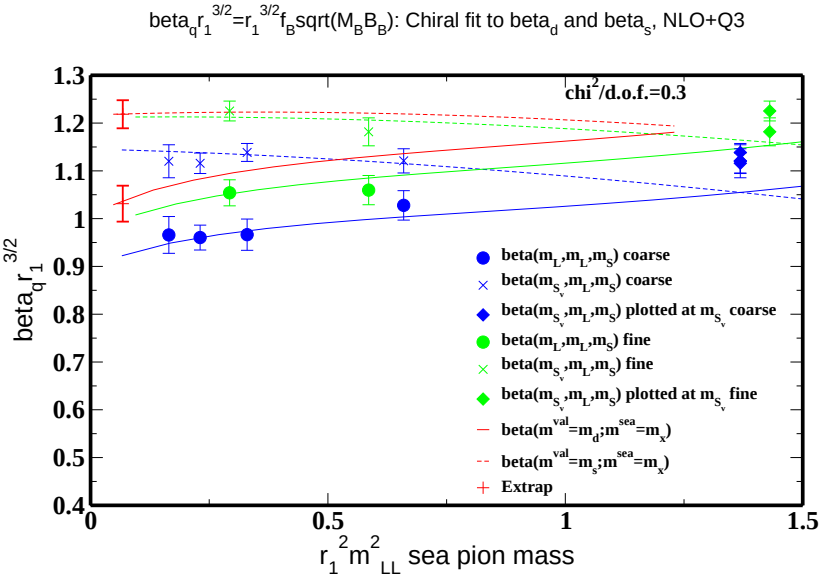

Figure 6.10: $NLO + Q_3$ fit plotted in sea quark mass plane. The fit lines follow the data well.

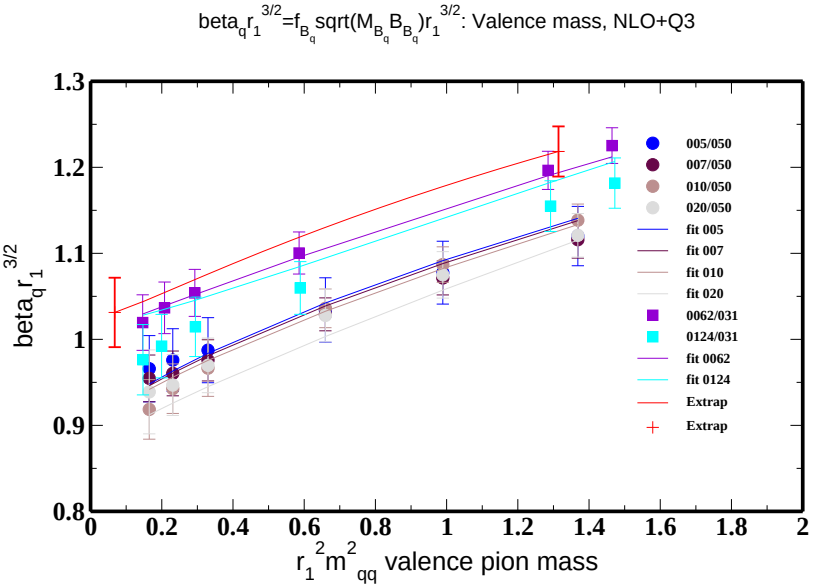

Figure 6.11: $NLO + Q_3$ fit, plotted in valence mass plane. All mass points shown.

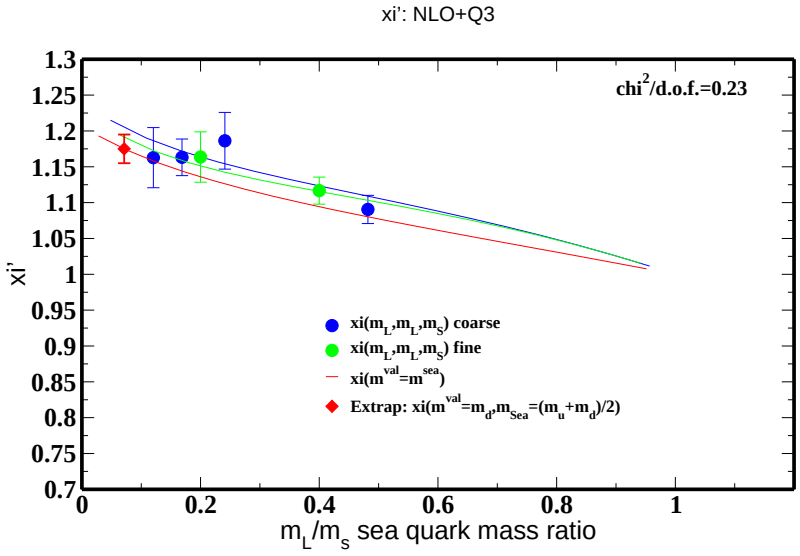

Figure 6.12: $NLO + Q_3$ fit plotted in sea quark mass plane. The fit lines follow the data well.

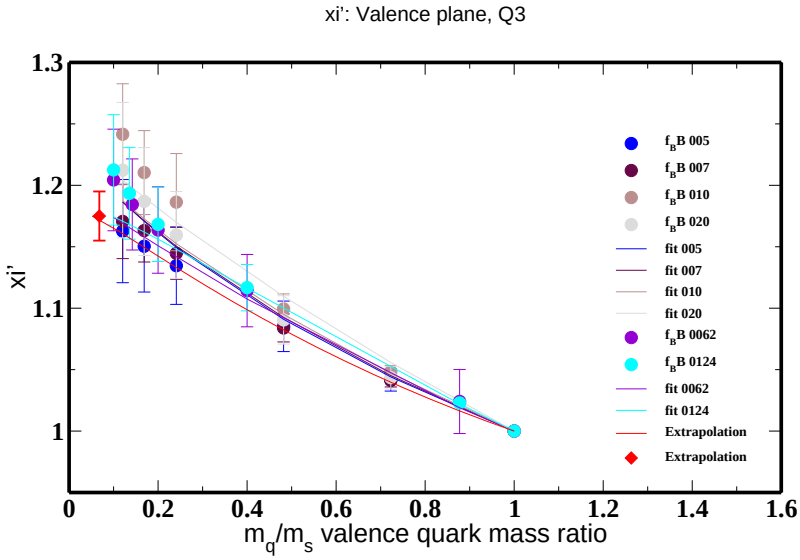

Figure 6.13: $NLO + Q_3$ fit, plotted in valence mass plane. All mass points shown.

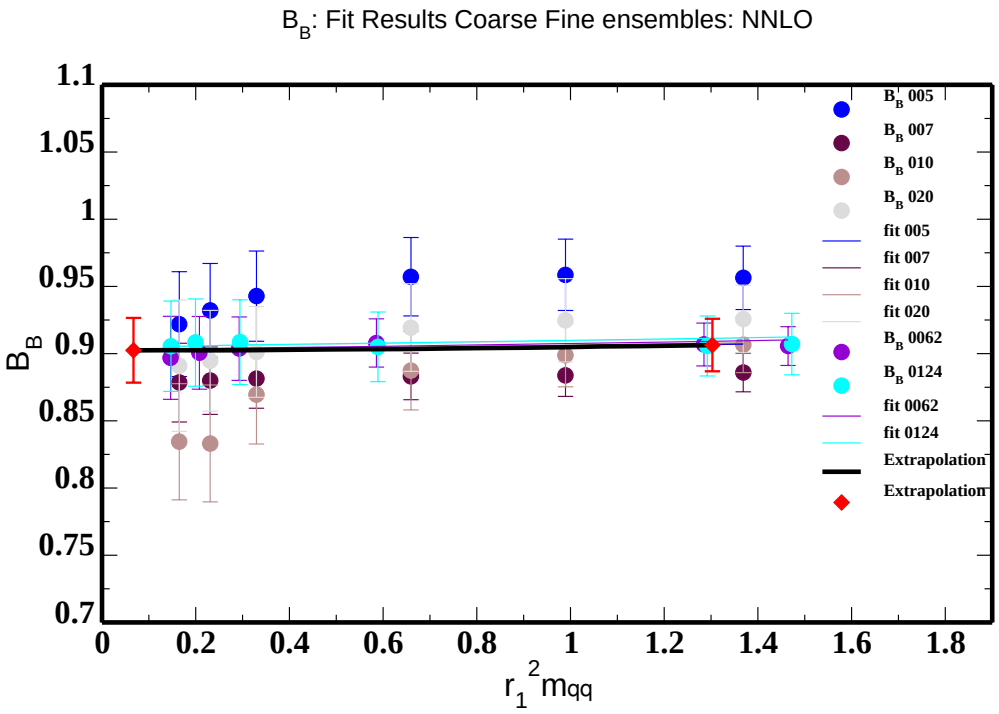

Figure 6.14: $NNLO$ fit to B_{B_q}.

6.4 Fiducial Point Method

The fiducial point method was introduced by Jack Laiho in the calculation of $B \to D^*$ form factors and is not used in our final analysis of the mixing parameters. We attempted to use this method, however the statistical errors in our current data set are too large for its successful implementation. It is presented here for completeness: in the near future the statistics of our data will be greatly increased and these techniques might become a viable alternative to the direct fits or provide a more robust way to estimate systematic errors.

Although the leading order light discretization effects are removed using r$S\chi$PT it does not account for heavy quark discretization effects. In order to reduce these it is useful to form the ratio

$$R_{fid}(m_x, m_L, m_s, a) = \frac{Q_1(m_x, m_L, m_h, a)}{Q_1(m_x^{fid}, m_L^{fid}, m_h^{fid}, a)} \tag{6.11}$$

where m_x is the light valence quark mass, m_L is the isospin averaged light sea quark mass, and m_h is the sea s quark mass. In the above ratio the heavy quark discretization terms are largely canceled. To recover the Q_1^{phys}, the physical value for the operator, the lattice spacing is set to 0 in R_{fid}, and R_{fid} is multiplied by the fiducial point $Q_1(m_x^{fid}, m_L^{fid}, m_s^{fid}, a^{fid})$. The discretization errors will then scale with the lattice spacing at the fiducial point. It is useful to use a fiducial mass at about $m_s/2$. In this region the mass is large enough that a very fine lattice could be used without running into finite size effects. It is also not so large that NLO $S\chi$PT is no longer effective. In our exploratory fits we used the finest ensemble available for the fiducial point, with a lattice spacing of $a = 0.09$ fm.

In an effort to disentangle systematic errors due to sea quark discretization effects and valence quark discretization effects it is useful to factor R_{fid} into two parts

$$\begin{aligned} R_{fid}(m_x, m_L, m_h, a) &= R_{sea}(m_x^{fid}, m_L, m_h, a) \\ &\times R_{val}(m_x, m_L^{fid}, m_h^{fid}, a) \end{aligned} \tag{6.12}$$

$$R_{sea}(m_L, m_h, a) = \frac{Q_1(m_x^{fid}, m_L, m_h, a)}{Q_1(m_x^{fid}, m_L^{fid}, m_h^{fid}, a)} \tag{6.13}$$

$$R_{val}(m_x, m_L, m_h, a) = \frac{Q_1(m_x, m_L, m_h, a)}{Q_1(m_x^{fid}, m_L, m_h, a)}, \tag{6.14}$$

where R_{sea} contains most of the sea quark dependence, and R_{val} contains most of the valence quark dependence. R_{sea} should be close to 1 because of the mild sea quark dependence. R_{val} will have a stronger dependence on the valence mass and so less trivial chiral behaviour, however because it is a ratio some of the statistical errors will cancel.

Chapter 7

Systematic Error Analysis

In this Chapter the sources of systematic error in the calculation of $\langle \bar{B}|Q_q^1|B\rangle$ are identified and conservatively estimated. At the end of the Chapter the errors are tabulated and added in quadrature to arrive at a total systematic error.

7.1 Inputs into the Analysis

Heavy-quark Mass Uncertainty

The mixing parameters depend on the b quark mass used in our simulations, where the hopping parameter κ_b is tuned so that the kinetic mass, M_2, agrees with experiment. The Fermilab action's dispersion relation is [15]

$$E(\vec{p}) = M_1 + \frac{\vec{p}^2}{M_2} + b_1\vec{p}^4 + b_2\sum_{j=1}^{3}|p_j|^4 + \mathcal{O}(\vec{p}^6), \tag{7.1}$$

where κ_b enters into the definitions of M_1 and M_2. Two-point functions for the pseudoscalar and vector mesons are calculated at several momenta, and the pole mass, $E(\vec{p})$, for each particle and at each momentum extracted. The dispersion relation is then fit to and M_2 is determined, and the spin average of the results is taken. The κ_b is then adjusted until M_2 agrees with the spin-averaged B_s meson mass.

The value obtained through this procedure is used as the central value for κ_b, with statistical and fitting errors of 3.7% on the fine ensembles. There are also discretization errors in κ_b which are determined by estimating discretization effects in the Fermilab action's heavy-quark potential, with an estimated size of 2.4%. Adding the errors in quadrature gives a total systematic error in κ_b of 4.4%.

The uncertainty in the mixing parameters due to the uncertainty in κ_b is

$$\sigma_{\langle O\rangle} = \frac{\Delta\langle O\rangle}{\Delta\kappa_b}\sigma_{\kappa_b}, \tag{7.2}$$

where $\langle O\rangle$ is one of the mixing parameters, $f_{B_q}\sqrt{B_{B_q}}$ or B_{B_q}.

To determine $\frac{\Delta\langle O\rangle}{\Delta\kappa_b}$ we calculate the parameters at three different κ values, $\kappa = 0.074, 0.086, 0.093$, on the l2064f21b676m020m050 coarse ensemble for a single valence mass, $m = 0.0415$, and times source, $t = 0$. There was no statistically significant change in central value over the various kappa's. We consider this result preliminary, but suggestive that the uncertainty due to κ_b is very small. For the purpose of this report we use the percentage uncertainty found in the f_B, f_{B_s} analysis. It is likely a very conservative estimate given our observed insensitivity to κ_b.

Quantity	a=0.0 fm
$am_s \times 10^2$	2.82(0)(4)(11)
$a\frac{(m_u+m_d)}{2} \times 10^3$	1.034(4)(11)(42)
$am_d \times 10^3$	1.46(1)(2)(6)

Table 7.1: Latest determination of the "physical" light-quark masses used in the chiral extrapolations. These values were determined by the MILC collaboration [39]. The error in the first parentheses indicates statistical error, the second chiral extrapolation systematics, the third scale uncertainty.

Light-quark Mass Uncertainty

The physical values of the light quark masses used for the extrapolations to β_d and β_s are determined by the MILC collaboration. They are determined by making the charged pions and kaons take on their physical values. They are listed in Table 7.1 Errors due to the light quark mass uncertainty are estimated by adding the above errors in quadrature, then individually varying each quark mass within this uncertainty and performing the preferred chiral fit and extrapolation. The central values arrived at using each mass variation are compared to the fit which used the central values for the masses, and their differences are added in quadrature. This gives a total systematic error of 0.7%, 0.5%, and 0.3% for ξ, β_d, and β_s respectively

Uncertainty in the Scale r_1

The value of r_1 determined in Ref. [5] is $r_1 = 0.318(7)$. To estimate the error due to the scale uncertainty r_1 is varied within $0.311 - 0.325$ and all parameters that depend on the physical r_1 are appropriately adjusted. The uncertainty in scale gives a total systematic error of 0.2%, 3.1%, and 3.0% for ξ, β_d, and β_s respectively

Uncertainty in g_π

The heavy-quark parameter that couples B, B^*, π interaction is poorly known. It is a fit parameter in our analysis, with a central value of $g_\pi^2 = 0.35$ and width of $\sigma_{g_\pi^2} = 0.14$. This width covers all ranges of determinations of g_π, but to estimate its effects in the fits we both vary the central value of g_π with in its prior widths and double the prior width. Our fits are very insensitive to this parameter.

7.2 Higher Order Effects in the Perturbative Matching

Perhaps the most straightforward and conservative way to estimate the effects of the missing higher order terms in the perturbative matching is by multiplying the one-loop coefficients by $\alpha_s^2 = \alpha_V^2(2/a)$. This naive estimate, using preliminary results for the coefficients, gives an error of $\sim 4\%$ in β_d and β_s. We could also look at the size of the shift from the tree-level values for the matrix elements to the one-loop values after the matching coefficients are finalized. Preliminary matching results suggest ξ will not shift more than 0.5%.

7.3 Discretization Errors

Chiral Extrapolation Systematics and Light Quark Discretization

The errors due to fit Ansatz and light-quark discretization effects cannot be disentangled. Every fit Ansatz necessarily treats the discretization errors differently, and $NNLO$ logs are not included in the chiral expression so there is no way to be sure most $NNLO$ effects are accounted for. The $NNLO$ effects are estimated by the process used in the previous Chapter 5, where the range of fits generated by considering every Ansatz is used as the sytematic error. These errors were estimated to be 2.8%, 2.5%, and 0.4% for ξ, β_d, and β_s respectively.

Heavy-quark Discretization Effects

These effects can be estimated by power counting. In the matrix elements these effects begin at $\mathcal{O}(\alpha_s\Lambda_{\rm QCD}/M, (\Lambda_{\rm QCD}/M)^2)$. Assuming values of $\alpha_s = 0.3$, $\Lambda_{\rm QCD} = 500$ MeV and $M = 4.2$ GeV we have $\alpha_s\Lambda_{\rm QCD}/M = 0.036$ and $(\Lambda_{\rm QCD}/M)^2 = 0.014$ giving a total error of 3.5% in β_d and β_s. These errors largely cancel in ξ, where they appear at $\mathcal{O}(\alpha_s\Lambda_{\rm QCD}/aMm_s)$. In our calculations $\alpha_s\Lambda_{\rm QCD}/aMm_s < 0.2\%$.

7.4 Finite Volume Corrections

The chiral expression used in our fits for $\langle\bar{B}|Q_q^1|B\rangle$ treated the integrals as infinite when evaluating them, when in fact they should be treated as sums over discrete momenta, $q_n = 2\pi n/L, \quad n = (n_t, n_x, n_y, n_z)$, where L is the length of a side of the lattice and n is a vector of integers. The error introduced by this approximation, although small, should be estimated in a complete calculation of $\langle\bar{B}|Q_q^1|B\rangle$

Following the prescription for calculating finite volume corrections described in Refs. [6][4] we treat the time direction as infinite and treat only the spatial directions as finite. This is a reasonable approximation on the MILC lattices, where the length in the time direction is $\sim 3\times$ the spatial lengths. We replace integrals in the chiral expression such as

$$\mathcal{I} = \int \frac{d^4q}{(2\pi)^4}\frac{1}{(q^2+m^2)} = \frac{1}{16\pi^2}m^2\ln(m^2/\Lambda_\chi^2) \tag{7.3}$$

with finite sums over the spatial momentum

$$\mathcal{I} \to \mathcal{I}^{(L)} = \frac{1}{L^3}\sum_{\vec{n}}\int\frac{dq_0}{2\pi}\frac{1}{q_0^2+(\vec{q}_n)^2+m^2}. \tag{7.4}$$

The differences between the finite volume sums and infinite volume integrals that contribute in the expression for $\langle\bar{B}|Q_q^1|B\rangle$ are sums over Bessel functions. For example, in the above case

$$\mathcal{I}^{(L)} - \mathcal{I} = \frac{m^2}{16\pi^2}\delta_1(mL), \quad \delta_1(mL) = \frac{4}{mL}\sum_{\vec{n}\neq 0}\frac{(K_1(|\vec{n}|mL)}{|\vec{n}|}. \tag{7.5}$$

In fact the necessary substitutions for our chiral expression are given explicitly

in Ref. [4], where for terms without a factor of g_π^2 multiplying them we make the substitutions

$$m^2 \ln(m^2/\Lambda_\chi^2) \to m^2 \ln(m^2/\Lambda_\chi^2) + m^2 \delta_1(mL) \tag{7.6}$$

$$-\frac{\partial}{\partial m^2} m^2 \ln(m^2/\Lambda_\chi^2) \to -\frac{\partial}{\partial m^2} m^2 \ln(m^2/\Lambda_\chi^2) + \delta_3(mL), \tag{7.7}$$

where

$$\delta_3(mL) = 2 \sum_{\vec{n}} K_0(|\vec{n}|mL). \tag{7.8}$$

For terms with a factor of g_π^2 multiplying them we make the substitutions

$$m^2 \ln(m^2/\Lambda_\chi^2) \to m^2 \ln(m^2/\Lambda_\chi^2) + \frac{m^2}{3}(\delta_1(mL) - 2\delta_3(mL) \tag{7.9}$$

$$-\frac{\partial}{\partial m^2} m^2 \ln(m^2/\Lambda_\chi^2) \to \tag{7.10}$$

$$-\frac{\partial}{\partial m^2} m^2 \ln(m^2/\Lambda_\chi^2) + \delta_3(mL) - \frac{2}{3}\delta_5(mL),$$

where

$$\delta_5(mL) = mL \sum_{\vec{n}} |\vec{n}| K_1(|\vec{n}|mL). \tag{7.11}$$

The different forms of the corrections are directly due to the forms of the integrals involved, specifically terms without a factor of g_π^2 come from integrals that do not involve the B^* meson propagator: the tadpole corrections. Those that do have a factor of g_π^2 are from the wave-function renormalization and sunset diagrams.

For the purposes of this report's error estimation the corrections to the infinite volume expressions are simply calculated, setting $a \to 0$ and using the physical sea and valence quark masses. Of course the corrections could be added to the chiral expressions that are fit to, and the fitting performed to the corrected expression. This additional step of fitting would be straightforward to perform and provide an even better estimate, but because the finite volume errors are so much less than the other systematic errors the additional effort isn't worthwhile at this point.

The finite volume corrections turn out to be negligible, $< 0.1\%$, in the mixing parameters on the lattices we are working on.

7.5 Final Error Budget

The final error budget for the B mixing calculation is listed in Table 7.2 with the largest errors highlighted in red.

Parameter	ξ'	$\beta_d r_1^{3/2}$	$\beta_s r_1^{3/2}$
Central Value	1.215	1.006	1.222
Source of Uncertainty		% Error	
Statistical	3.1	4	2.7
Higher Order Matching	~ 0.5	~ 4	~ 4
Heavy Quark Discretization	0.2	3.5	3.5
Chiral extrap. errors			
Light Quark Discretization + Ansatz	2.8	2.5	0.4
scale uncertainty (r_1)	0.2	3.1	3.0
$g_{BB^*\pi}$	0.3	0.6	0.3
input parameters: $\hat{m}$,m_d,m_s	0.7	0.5	0.3
finite volume	< 0.1	< 0.1	< 0.1
estimated from FNAL-MILC f_B			
κ_b	< 0.1	1.1	1.1
Total Systematic	2.96	6.78	6.23
Total % Error	4.29	7.87	6.79

Table 7.2: The total systematic error budget for the B mixing matrix element calculation. The uncertainty due to κ_b is negligible in our preliminary estimates, and the uncertainty found in the Fermilab Lattice MILC collaborations' calculation of f_B and f_{B_s} is used as a conservative estimate.

Chapter 8

Summary of Results and Outlook

8.1 Summary of Results

We list the results for the B mixing parameters without matching included in Table 8.1. The error we present includes all systematic and statistical errors added in quadrature. The values for $f_B\sqrt{B_B}$ and $f_{B_s}\sqrt{B_{B_s}}$ are expected to shift down by $\sim 5\%$ after matching. The value for ξ is expected to change by $< 0.1\%$ and the results presented for it can be considered final.

Parameter	Central Value (uncertainty)
ξ	1.205(52)
$f_B\sqrt{B_B}$ GeV	0.213(17)
$f_{B_s}\sqrt{B_{B_s}}$ GeV	0.257(17)
B_B	0.88(2)
B_{B_s}	0.90(2)
B_{B_s}/B_B	1.02(1)

Table 8.1: Results for the B mixing parameters without matching coefficients. The results for the bag parameters are preliminary, all systematic errors have not been included.

The determination of $|V_{td}/V_{ts}|$ using this report's calculation of ξ and experimental measurements is listed in Table 8.2. It is not useful to extract the V_{td} and V_{ts} separately without the perturbative matching included.

$\lvert\frac{V_{td}}{V_{ts}}\rvert$	$0.2053 \pm 0.0007(\text{exp.}) \pm 0.0089(\text{theory})$

Table 8.2: The determination of $|V_{td}/V_{ts}|$ using this report's calculation of ξ.

It may be noted that the uncertainty in this report's determination of the CKM matrix element ratio has not improved on its previous determinations. It is important to appreciate that this is a complete calculation though, all systematic errors are accounted for, whereas the previous determinations relied on a quenched calculation that had uncontrolled errors. Thus the central values and uncertainty in this determination of the CKM matrix elements can be used with no restrictions in Unitarity Triangle analyses.

8.2 Outlook

Aside from the obvious step of incorporating the perturbative matching coefficients, there are many straightforward ways to increase the precision of this calculation, many of which are currently underway. In particular,

- The correlator statistics will be greatly increased.

  ◊ The number of configurations within each MILC ensemble has been extended, $N_{conf} \sim 600 \rightarrow \sim 2000$.

  ◊ It was discovered that averaging the correlators over even more time sources improves the statistics of the correlator. These additional time sources will be combined with a new method of randomizing the spatial origin of each correlator, which has been shown to greatly reduce correlations between quantities calculated on the same ensemble, and so effectively increase the statistics.

  ◊ The increase in statistical power is expected to reduce the statistical errors in the correlator fits from $3-5\% \rightarrow 1-2\%$. With smaller correlator errors the chiral fits will have smaller statistical errors and be more stable with varying Ansatz.

- ◊ MILC ensembles at a lattice spacing of $a = 0.06$ fm have been created. Using these in the calculation will increase the range of lattice spacings and reduce the discretization errors. In addition the perturbative errors, which scale with α_s, will be smaller on these lattices.

The methods and code developed by the author can be used with very little modification to incorporate these planned improvements, and a far more precise determination of the CKM matrix elements should be possible in the near future.

Appendix A

A.1 Code

An attempt is made to give examples of the correlator construction codes and correlator fit codes here.

A.1.1 Correlator Construction Code

The following excerpt of code from the file `3-pt.cpp` is used to construct the open-meson propagator and tie together the three- and two-point functions needed for the calculation of the mixing parameters. It is a `C++` based code, using classes from the FermiQCD toolkit.

```
#include <iostream>
#include <sstream>
#include <fermiqcd.h>
#include <JNS_io.hpp>
#include "./clover_gen/rotation.h"

////////Functions and Definitions//////////////////////////
class open_indices {
public:
  mdp_complex c[4][4][3][3];
};

void C3_construct_TxT(mdp_field<open_indices>& open_prop,Matrix G1,Matrix \\
G2,mdp_array<Complex,2> &Cor) {

  int nt=open_prop.lattice().size(0);
  site x1d(open_prop.lattice());
  mdp_array<Complex,1>  C1(nt), C2(nt), C3(nt), C4(nt);
  mdp_array<Complex,2>  C_3(nt,nt);

  for(int a=0;a<4;a++)
    for(int i=0;i<3;i++)
      for(int j=0;j<3;j++)
for(int c=0;c<4;c++) {
```

```
  for(int b=0;b<4;b++) {
    forallsites(x1d) {
      C1(x1d(0))+=open_prop(x1d).c[a][b][i][j]*G1(b,a);
      C2(x1d(0))+=open_prop(x1d).c[c][b][j][i]*G2(b,c);
      C3(x1d(0))+=open_prop(x1d).c[a][b][i][i]*G1(b,c);
      C4(x1d(0))+=open_prop(x1d).c[c][b][j][j]*G2(b,a);
    }
  }
  mpi.add(C1.address(),C1.size());
  mpi.add(C2.address(),C2.size());
  mpi.add(C3.address(),C3.size());
  mpi.add(C4.address(),C4.size());

  for(int tx=0;tx<nt;tx++)
    for(int ty=0;ty<nt;ty++)
      C_3(tx,ty)+=(C1(ty)*C2(tx)+C1(tx)*C2(ty)-C3(tx)*C4(ty) \\
      -C3(ty)*C4(tx))/2;



  for (int tx=0;tx<nt;tx++)
    C1(tx)=C2(tx)=C3(tx)=C4(tx)=0;

}

  for(int tx=0;tx<nt;tx++)
    for(int ty=0;ty<nt;ty++)
      Cor(tx,ty)=C_3(tx,ty);
}

void C3_construct(mdp_field<open_indices>& open_prop,Matrix G1, \\
Matrix G2,mdp_array<Complex,2> &Cor) {

  int nt=open_prop.lattice().size(0);
  site x1d(open_prop.lattice());
  mdp_array<Complex,1>  C1(nt), C2(nt), C3(nt), C4(nt);
  mdp_array<Complex,2>  C_3(nt,nt);

  for(int a=0;a<4;a++)
    for(int i=0;i<3;i++)
      for(int j=0;j<3;j++)
for(int c=0;c<4;c++) {

  for(int b=0;b<4;b++) {
    forallsites(x1d) {
      C1(x1d(0))+=open_prop(x1d).c[a][b][i][i]*G1(b,a);
      C2(x1d(0))+=open_prop(x1d).c[c][b][j][j]*G2(b,c);
      C3(x1d(0))+=open_prop(x1d).c[a][b][i][j]*G1(b,c);
```

```
      C4(x1d(0))+=open_prop(x1d).c[c][b][j][i]*G2(b,a);
    }
  }
  mpi.add(C1.address(),C1.size());
  mpi.add(C2.address(),C2.size());
  mpi.add(C3.address(),C3.size());
  mpi.add(C4.address(),C4.size());

  for(int tx=0;tx<nt;tx++)
    for(int ty=0;ty<nt;ty++)
      C_3(tx,ty)+=(C1(ty)*C2(tx)+C1(tx)*C2(ty)-C3(tx)*C4(ty) \\
      -C3(ty)*C4(tx))/2;


  for (int tx=0;tx<nt;tx++)
    C1(tx)=C2(tx)=C3(tx)=C4(tx)=0;

}

  for(int tx=0;tx<nt;tx++)
    for(int ty=0;ty<nt;ty++)
      Cor(tx,ty)=C_3(tx,ty);
}

void print_C(mdp_array<Complex,2> &C, FILE* fp) {
  int nt=C.size(0);
    for(int tx=0;tx<nt;tx++)
      for(int ty=0;ty<nt;ty++) {
// printf("%i, %i %e  %e\n",tx,ty,real(C(tx,ty)),imag(C(tx,ty)));
fprintf(fp,"%i, %i %e  %e\n",tx,ty,real(C(tx,ty)),imag(C(tx,ty)));
      }
}

//For staggered->naive propagator conversion
Matrix OmegaMatrix(site x) {
  Matrix M(4,4);
  M=1;
  if(x(3)%2==1) M=Gamma[3]*M;
  if(x(2)%2==1) M=Gamma[2]*M;
  if(x(1)%2==1) M=Gamma[1]*M;
  if(x(0)%2==1) M=Gamma[0]*M;
  return M;
}

////////////////////////////////////////////////////
//////////////////////////
//////////////////Program Body//////////////////////
```

```
//////////////////////////////////////////////////
//////////////////////

int main(int argc, char **argv) {
  mpi.open_wormholes(argc,argv);

  //Lattice Parameters
  char* info=argv[1];
  //Meson prop to load
  string meson_prop_in=argv[2];
  //Meson prop to create and/or name to save data under
  char output_filename[1024];
  sprintf(output_filename,"%s_open",argv[3]);
  char* meson_prop_out=output_filename;

  //Set up lattice
  int nc=3;
  int L[4];
  L[0]=(int) val(prompt(info,"T","64"));
  L[1]=(int) val(prompt(info,"X","20"));
  L[2]=(int) val(prompt(info,"Y","20"));
  L[3]=(int) val(prompt(info,"Z","20"));
  int nt=L[0];

  int tsource=(int) val(prompt(info,"TSOURCE","0"));
  define_base_matrices("FERMILAB");
  generic_lattice mylattice(4,L,default_partitioning0,
    torus_topology,0,3,false);
  site x(mylattice);

  //Create 1d lattice and fields
  int L1[1];
  L1[0]=(int) val(prompt(info,"T","64"));
  generic_lattice mylattice1d(1,L1,default_partitioning0, \\
  torus_topology,0,3,false);
  mdp_site x1d(mylattice1d);
  mdp_field<open_indices> open_prop(mylattice1d);

  if (meson_prop_in=="NONE") {
    //Gauge configuration to load
    char* gauge_filename=argv[4];
    //Staggered Prop to load
    string staggered_prop=argv[5];
    char staggered_propagator [FILENAME_MAX];
    strncpy(staggered_propagator,staggered_prop.c_str(),FILENAME_MAX);
    //Wilson Prop to load
    string wilson_prop=argv[6];
```

```
char wilson_propagator [FILENAME_MAX];
strncpy(wilson_propagator,wilson_prop.c_str(),FILENAME_MAX);

string sink=argv[7];

coefficients wilson_quark; // Wilson-type heavy quark coefficents

//Clover Params
wilson_quark["kappa_s"]= val(prompt(info,"KAPPA_S","0.086")); \\
//b quark kappa
///////Rotation Coefficient d1///////////
mdp_real kappa_crit=val(prompt(info,"KAPPA_CRIT",".1"));
mdp_real u0=val(prompt(info,"u0",".8"));

mdp_real m_h,M_h,d1;
m_h=1/(2*wilson_quark["kappa_s"]*u0)-1/(2*kappa_crit*u0);
M_h=pow(2/(m_h*(2+m_h))+1/(1+m_h),-1);
d1=((1+m_h)/(m_h*(2+m_h))-1/(2*M_h))/u0;

wilson_quark["d1"]=d1;

JNS_IOstate io_gauge_state;
io_gauge_state.doClose=false;
JNS_IOstate io_wilson_state;
io_wilson_state.doClose=false;
JNS_IOstate io_staggered_state;
io_staggered_state.doClose=false;

//////////////////////////////////////////////////////
////////Staggered to Naive/////////////
//////////////////////////////////////////////////////
gauge_field U(mylattice,nc);
JNS_read<gl3_links<float> > (U,gauge_filename,0, \\
mylattice.size(1)*mylattice.size(2));

mdp_matrix_field chi(mylattice,nc,nc);
fermi_propagator S_l(mylattice,nc);

//Create Omega Matrix for staggered to naive conversion
mdp_matrix_field Omega(mylattice,4,4);
forallsites(x) Omega(x)=OmegaMatrix(x);

JNS_read<io_gl3_matrix<float> > (chi,staggered_propagator,0, \\
mylattice.size(1)*mylattice.size(2));

//Convert to Naive prop
for(int i=0;i<nc;i++) {
```

```
      for(int j=0;j<nc;j++)
for(int a=0;a<4;a++)
  for(int b=0;b<4;b++)
    forallsites(x) {
    S_l(x,b,a,j,i)=Omega(x,b,a)*chi(x,i,j);
  }
    }
    Omega.deallocate_field();
    chi.deallocate_field();

    ////Load Wilson Prop////
    fermi_field psi(mylattice,nc);
    fermi_propagator S_h(mylattice,nc);

    for (int a=0;a<4;a++)
      for (int i =0;i<3;i++) {

JNS_read<Wilson_sc_quark<float> >  \\
(psi,wilson_propagator,3*a+i,mylattice.size(1)*mylattice.size(2));

//Rotate if a delta sink
if (sink=="d") {
  mdp<<"Rotating delta sink"<<endl;
  rotation(psi,U,wilson_quark);
}
else if (sink=="1S") {
  mdp<<"Don't Rotate sink, it is 1S smeared"<<endl;
}

forallsites(x)
  for (int b=0;b<4;b++)
    for (int j=0;j<3;j++)
      S_h(x,b,a,j,i)=psi(x,b,j);

      }

    ////////////////////////////////////////////
    ///////Open Prop Creation////////
    ////////////////////////////////////////////


    //Initialize open meson prop variable
    forallsites(x1d)
      for(int a=0; a<4; a++)
for(int b=0; b<4; b++)
  for(int i=0; i<3; i++)
    for(int j=0; j<3; j++) {
```

```
      open_prop(x1d).c[a][b][i][j]=0;

    }
    //Create open meson prop
    int d;
    forallsites(x) {
      x1d.set(x(0));
      for(int i=0;i<nc;i++)
for(int j=0;j<nc;j++)
  for(int k=0;k<nc;k++)
    for(int a=0;a<4;a++)
      for(int b=0;b<4;b++)
for(int c=0;c<4;c++) {
  d=Gamma5_idx[b];
  open_prop(x1d).c[d][a][i][k]+=Gamma5_val[b]* \\
  conj(S_h(x,c,b,j,i))*S_l(x,c,a,j,k);
}
    }
    mdp << "Saving open meson prop" <<endl;
    open_prop.save(meson_prop_out);
  }
  else {

    mdp<< "Loading open meson prop" <<endl;
    open_prop.load(meson_prop_in);
  }

 char outfile[1024];
 sprintf(outfile,"%s.3pt",meson_prop_out);
 FILE *fp=fopen(outfile,"w");
 ////////////////////////////////////////////////////
 /////////Correlator Calculations//////////////
 ////////////////////////////////////////////////////
 mdp_array<Complex,1> C_2(nt);
 mdp_array<Complex,1> R(nt);
//Initialize 2-pt function
 for(int t=0;t<nt;t++) {
   C_2(t)=0;
   R(t)=0;
 }
 Matrix A_4=Gamma[0]*Gamma5;
 //Create 2-pt function
 forallsites(x1d) {
   for(int i=0;i<nc;i++)
     for(int a=0;a<4;a++)
       for(int b=0;b<4;b++) {
 C_2(x1d(0))+=A_4(b,a)*open_prop(x1d).c[a][b][i][i];
```

```
R(x1d(0))+=Gamma5(b,a)*open_prop(x1d).c[a][b][i][i];
      }
}
mpi.add(C_2.address(),C_2.size());
mpi.add(R.address(),R.size());
if(ME==0) {

  mdp<< "A4xGamma5"<<endl;
  fprintf(fp,"%s","A4xGamma5\n");
  for (int t=0;t<nt;t++) {
    mdp << t << ": " << C_2(t) <<endl;
    fprintf(fp,"%i, %e  %e\n",t,real(C_2(t)),imag(C_2(t)));
  }

  mdp<<"Gamma5xGamma5"<<endl;
  fprintf(fp,"%s","Gamma5xGamma5\n");
  for (int t=0;t<nt;t++) {
    mdp<<t<<": "<<R(t)<<endl;
    fprintf(fp,"%i, %e  %e\n",t,real(R(t)),imag(R(t)));
  }
}
////////////////////////////////////////////////

//3-pt Function
////////////////////////////////////////////////

Matrix G1,G2;
Matrix PL,PR;
PL=(1-Gamma5)/2;
PR=(1+Gamma5)/2;
mdp_array<Complex,2> A(nt,nt),B(nt,nt),C(nt,nt),D(nt,nt), \\
E(nt,nt),F(nt,nt),Sum(nt,nt);
////////////////////////////////////////////////////////
mdp<<"PLxPL"<<endl;
if(ME==0) fprintf(fp,"%s","PLxPL\n");
C3_construct(open_prop,PL,PL,C);
if(ME==0) print_C(C,fp);

mdp<<"PLxPL_TxT"<<endl;
if(ME==0) fprintf(fp,"%s","PLxPL_TxT\n");
C3_construct_TxT(open_prop,PL,PL,C);
if(ME==0) print_C(C,fp);

mdp<<"Gamma[mu]*PLxGamma[mu]*PL" <<endl;
if(ME==0) fprintf(fp,"%s","Gamma[mu]*PLxGamma[mu]*PL\n");
C3_construct(open_prop,Gamma[0]*PL,Gamma[0]*PL,A);
C3_construct(open_prop,Gamma[1]*PL,Gamma[1]*PL,B);
```

```
 C3_construct(open_prop,Gamma[2]*PL,Gamma[2]*PL,C);
 C3_construct(open_prop,Gamma[3]*PL,Gamma[3]*PL,D);

 for(int tx=0;tx<nt;tx++)
   for(int ty=0;ty<nt;ty++)
     Sum(tx,ty)=A(tx,ty)+B(tx,ty)+C(tx,ty)+D(tx,ty);

 if(ME==0) print_C(Sum,fp);

 fclose(fp);
 ////////////////////////////////////////////////////////
 mdp<< "Configuration Completed" <<endl;


 mpi.close_wormholes();
}
```

A.1.2 Correlator Fit Code

This excerpt of code extracts a heavy-light, four-quark operator matrix element, as defined in the text from simultaneous fits to 2 two-point functions and one 3-point function. It is in the `Python` file `fitfbB-3corr_boot.py` It uses bootstrapping to estimate the statistical errors of the fit parameters. The parametrization of the fit function may be of particular relevance to future calculations.

```
 #!/usr/bin/env python
import sys, string
sys.path.append('/home/rtevans/fitter/fit_modules/')
sys.path.append('/home/rtevans/fitter/')
import scipy
import string,os
import math;m=math
import RandomArray; RA = RandomArray
import LinearAlgebra; LA = LinearAlgebra
from fit import *
from time import time
import prior
import Matrix
import lsqfit
import random
N=Numeric

bag='B'
# Mass of valence quark
mass=(sys.argv[8])
# Number of States in 2pt and 3pt fit, nstates2pt>=nstates
nstates2pt=int(sys.argv[1])
nstates=int(sys.argv[4])
```

```
# 2pts
tmin=int(sys.argv[2])
tmax=int(sys.argv[3])
# 3pt
#sinks
t1min=int(sys.argv[5])
t1max=int(sys.argv[6])
#sources
t2min=int(sys.argv[5])
t2max=int(sys.argv[6])

lattice=sys.argv[9]

print 'nstates2pt=',nstates2pt
print 'nstates=',nstates
print '2pt:',tmin,'-',tmax
print '3pt:',t1min,'-',t1max,'x',t2min,'-',t2max


def f(x,p):
    n=nstates
    n2pt=nstates2pt
    Zs0=N.exp(p[0:2])
    Zs=p[2:n2pt]

    Z=N.exp(p[n2pt:2*n2pt])
    O0=N.exp(p[3*n2pt])
    O=p[3*n2pt+1:3*n2pt+n]
    Op=p[3*n2pt+n:3*n2pt+2*n]
    M=3*n2pt+2*n

    E=p[M]
    Ep=E+N.exp(p[M+1])
    # P5_P5
    function=.5*Z[0]*Zs0[0]*N.exp(-E*x)
    function2=.5*Z[0]*Z[0]*N.exp(-E*x)
    k=(-(-1)**x)
    function=function+0.5*Zs0[1]*Z[1]*N.exp(-Ep*x)*k
    function2=function2+0.5*Z[1]*Z[1]*N.exp(-Ep*x)*k

    for i in range (2,n2pt-2):
        if i%2==0:
            E=E+N.exp(p[i+M])
            function=function+.5*Z[i]*Zs[i-2]*N.exp(-E*x)
        if i%2==1:
            Ep=Ep+N.exp(p[i+M])
            function=function+.5*Z[i]*Zs[i-2]*N.exp(-Ep*x)*k
```

```
E=p[M]
Ep=E+N.exp(p[M+1])
k=(-(-1)**x)
for i in range (2,n2pt):
    if i%2==0:
        E=E+N.exp(p[i+M])
        function2=function2+.5*Z[i]*Z[i]*N.exp(-E*x)
    if i%2==1:
        Ep=Ep+N.exp(p[i+M])
        function2=function2+.5*Z[i]*Z[i]*N.exp(-Ep*x)*k

function=ValDer.concat(function,function2)

# O
k1=(-(-1)**x1)
for T in x2:
    temp=0
    k2=(-(-1)**T)
    for i in range (0,n):
        if i==0: Ei=p[M]
        elif i==1: Epi=Ei+N.exp(p[M+1])
        else:
            if i%2==0: Ei=Ei+N.exp(p[i+M])
            if i%2==1: Epi=Epi+N.exp(p[i+M])
        for j in range (0,n):
            if j==0: Ej=p[M]
            elif j==1: Epj=Ej+N.exp(p[M+1])
            else:
                if j%2==0: Ej=Ej+N.exp(p[j+M])
                if j%2==1: Epj=Epj+N.exp(p[j+M])
            if i==j:
                if i==0: Om=OO*Zs0[0]**2
                else: Om=O[i-1]

            else: Om=Op[i]*Op[j]
            if i%2==0 and j%2==0:
                temp=temp-0.25*Om*N.exp(-Ei*x1-Ej*T)
            elif i%2==0 and j%2==1:
                temp=temp-0.25*Om*N.exp(-Ei*x1-Epj*T)*(k2)
            elif i%2==1 and j%2==0:
                temp=temp-0.25*Om*N.exp(-Epi*x1-Ej*T)*(k1)
            elif i%2==1 and j%2==1:
                temp=temp-0.25*Om*N.exp(-Epi*x1-Epj*T)*(k1*k2)

    function=ValDer.concat(function,temp)
return function/sigma
```

```
print lattice
# Load Data Arrays
kappa='-k0.086'
file=open('/home/rtevans/fitter/kappa_data/'+lattice+ \\
'P5xP5_d_1S'+kappa+'-m'+mass+'-ave.dat')
c=N.pickle.Unpickler(file)
c2=c.load()
file.flush()

file=open('/home/rtevans/fitter/kappa_data/'+lattice+ \\
'P5xP5_d_d'+kappa+'-m'+mass+'-ave.dat')
c=N.pickle.Unpickler(file)
c3=c.load()
file.flush()

if bag=='BS': file=open('/home/rtevans/fitter/data/'+lattice \\
+'PLxPL_d_1S-m'+mass+'-ave.dat')
if bag=='B': file=open('/home/rtevans/fitter/kappa_data/ \\
'+lattice+'Gamma[mu]PLxGamma[mu]PL_d_1S'+kappa+'-m'+mass+'-ave.dat')

c=N.pickle.Unpickler(file)
O4=c.load()
file.close



###Block data by bs
bs=4
samples=int(len(O4)/bs)
y0=N.zeros([samples,tmax-tmin],N.Float)
y1=N.zeros([samples,tmax-tmin],N.Float)
y2=N.zeros([samples,tmax-tmin],N.Float)
z=N.zeros([samples,(t1max-t1min),(t2max-t2min)],N.Float)

c2p=c2[:,::-1]
c3p=c3[:,::-1]

O4=O4[:,1:len(O4[1]),1:len(O4[2])]
Oprime=N.zeros([samples,len(O4[1]),len(O4[2])],N.Float)
for j in range(0,samples*bs,bs):
    for b in range (0,bs):
        y0[j/bs]+=(c2[j+b,tmin:tmax]+c2p[j+b,(tmin-1):(tmax-1)])/(2*bs)
        y2[j/bs]+=(c3[j+b,tmin:tmax]+c3p[j+b,(tmin-1):(tmax-1)])/(2*bs)
        Oprime[j/bs]+=(O4[j+b,:,:]+O4[j+b,::-1,::-1])/(2.0*bs)
Oprime=Oprime[:,::-1,:]
if bag=='BS': Oprime=-Oprime
x=N.arange(tmin,tmax)
x1=N.arange(t1min,t1max)
```

```
x2=N.arange(t2min,t2max)
dt=len(x)
dt1=len(x1)
dt2=len(x2)
print 'samples=',len(Oprime)
z[:,0:dt1,0:dt2]=Oprime[:,(t2min-1):(t2max-1),(t1min-1):(t1max-1)]
z=N.reshape(z,(len(z),dt1*dt2))

y=N.concatenate((y0,y2,z),1)
ave=sum(y)/len(y)
start=time()

# Set up bootstrap
set_num=int(sys.argv[7])
B=N.zeros([set_num],N.Float)
fbB=N.zeros([set_num],N.Float)
M=N.zeros([set_num],N.Float)

y_s=N.zeros([set_num,len(y),len(y[1])],N.Float)

# Fit criteria
svd=1e-7
maxit=5000
rel=1.e-4
# Set seed to keep bootstraps for difference m_l correlated
Os=N.zeros([set_num,len(y[1])],N.Float)
random.seed(2)
for set in range (0,set_num):
    for j in range (0,len(z)):
        r=random.randint(0,len(z)-1)
        y_s[set,j]=y[r]
    Os[set]=sum(y_s[set])/len(y_s[0])

for set in range (0,set_num):
    print 'set=',set
    if set==0:
        cov=0
        for j in range (0,len(y)):
            cov+=(N.outerproduct(y[j],y[j])-\\
            N.outerproduct(ave,ave))/(len(y)**2)
        Os[0]=ave
    else:
        cov=0
        for j in range (0,len(y_s[1])):
            cov+=(N.outerproduct(y_s[set,j],y_s[set,j])- \\
            N.outerproduct(Os[set],Os[set]))/(len(y_s[1])**2)
```

```
    sigma=N.diagonal(cov)**0.5
    #sigma=N.ones([len(cov)],N.Float)
    covsc=N.zeros([len(cov),len(cov)],N.Float)
    for i in range (0,len(cov)):
        for j in range (0,len(cov)):
            covsc[i][j]=cov[i][j]/(sigma[i]*sigma[j])

    Os[set]=Os[set]/sigma

    # Priors
    if set==0: p0,pp,dp=prior.Bb_1S_priors(nstates2pt,nstates,0)
    else: k0,pp,dp=prior.Bb_1S_priors(nstates2pt,nstates,1)

    #p0[3*nstates2pt+2*nstates]=1.95
    #pp[3*nstates2pt+2*nstates]=1.95
    #p0[3*nstates2pt+2*nstates+1]=2.25
    #pp[3*nstates2pt+2*nstates+1]=2.25

    fitter=lsqfit.LSQFit(data=(x,Os[set],covsc),fcn=f,p0=p0,\\
    prior=lsqfit.GPrior(p0=pp,dp=dp),svdcut=svd,reltol=rel,maxit=maxit)

    fit=fitter()
    print fit
    if set==0: p0=fit.p

    if bag=='B':
        O=3.0*N.exp(fit.p[3*nstates2pt])
        dO=O*fit.dp[3*nstates2pt]
    if bag=='BS':
        O=(24./5.)*N.exp(fit.p[3*nstates2pt])
        dO=O*fit.dp[3*nstates2pt]
    m=fit.p[3*nstates2pt+2*nstates]
    fbB[set]=N.sqrt(abs(O))
    M[set]=m
    if bag=='B':
        print 'fbB ',fbB[set],'+/-',0.5*dO*O**(-0.5)
    if bag=='BS':
        print 'fbBS ',fbB[set],'+/-',0.5*dO*O**(-0.5)

if bag=='B':
    f=open('fbBk'+kappa+'_'+lattice+'_'+mass+'.dat','w')
    p=Numeric.pickle.Pickler(f)
    p.dump(fbB)
    f.close()

if bag=='BS':
    f=open('fbBS_'+lattice+'_'+mass+'.dat','w')
```

```
    p=Numeric.pickle.Pickler(f)
    p.dump(fbB)
    f.close()


fbB=N.sort(fbB)
M=N.sort(M)

fbB_med=fbB[set_num/2]
M_med=M[set_num/2]

fbB_ci_up=fbB[set_num/2+int(.682*set_num/2)]-fbB_med
fbB_ci_low=fbB_med-fbB[set_num/2-int(.682*set_num/2)]

M_ci_up=M[set_num/2+int(.682*set_num/2)]-M_med
M_ci_low=M_med-M[set_num/2-int(.682*set_num/2)]


print 'mass=',mass
print '# of sets=',set_num
print 'time for bootstrap=',time()-start,'s'
if bag=='B':
    print 'fb sqrt(B)=',fbB_med,'+',fbB_ci_up,'-',fbB_ci_low
if bag=='BS':
    print 'fb sqrt(BS)=',fbB_med,'+',fbB_ci_up,'-',fbB_ci_low
print 'M=',M_med,'+',M_ci_up,'-',M_ci_low
```

Appendix B

B.1 Chiral Expressions for $\langle \bar{B}_q | Q_q^1 | B_q \rangle$ and B_{B_q}

The exact form for the rooted staggered chiral perturbation theory is shown here. As stated in the text it was derived by [23]

The chiral expression has the following general form at NLO

$$\begin{aligned} &\left\langle \bar{B}_q | Q_q^1 | B_q \right\rangle_{QCD} = \frac{8}{3} m_{B_q}^2 f_{B_q}^2 B_q = m_{B_q} \left\langle \bar{B}_q | Q_1^q | B_q \right\rangle_{HQET} = \\ &m_{B_q} \beta \left[1 + (\mathcal{Q}_q + \mathcal{W}_q + \mathcal{T}_q) + L_v m_q + L_s (2m_L + m_h) + L_a a^2 \right]. \end{aligned} \tag{B.1}$$

We first define the following terms, valid in the infinite volume limit, [4]

$$\begin{aligned} h(m^2) &= m^2 \log(m^2/\Lambda_\chi^2) \\ \tilde{h}(m^2) &= -\log(m^2/\Lambda_\chi^2) - 1. \end{aligned} \tag{B.2}$$

The chiral logs in the are given by the wave function renormalization,

$$\begin{aligned} \mathcal{W}_q = \frac{-3 g_\pi^2}{16\pi^2 f^2} \Bigg\{ &\frac{1}{16} \sum_{\substack{j=qu,qd,qs \\ \Xi=I,P,4V,4A,6T}} h(m_{j\Xi}^2) + \frac{1}{3} \Big[R_{X_I}^{[2,2]}(\{M_{X_I}^{(5)}\};\{\mu_I\}) \tilde{h}(m_{X_I}^2) \\ - \sum_{j \in \{M_I^{(5)}\}} &D^{[2,2]}(\{M_{X_I}^{(5)}\};\{\mu_I\}) h(m_j^2) \Big] + a^2 \delta_V' \Big[R_{X_V}^{[3,2]}(\{M_{X_V}^{(7)}\};\{\mu_V\}) \tilde{h}(m_{X_V}^2) \\ &- \sum_{j \in \{M_V^{(7)}\}} D_{j,X_V}^{[3,2]}(\{M_{X_V}^{(7)}\};\{\mu_V\}) h(m_j^2) \Big] + (V \to A) \Bigg\}, \end{aligned} \tag{B.3}$$

tadpole diagram,

$$\begin{aligned} \mathcal{T}_q = \frac{-1}{16\pi^2 f^2} \Bigg\{ &\frac{1}{16} \sum_{\substack{j=qu,qd,qs \\ \Xi=I,P,4V,4A,6T}} h(m_{j\Xi}^2) + \frac{1}{16} \sum_{\Xi=I,P,4V,4A,6T} h(m_{qq\Xi}) \\ &+ \frac{2}{3} \left[R_{X_I}^{[2,2]}(\{M_{X_I}^{(5)}\};\{\mu_I\}) \tilde{h}(m_{X_I}^2) - \sum_{j \in \{M_I^{(5)}\}} D^{[2,2]}(\{M_{X_I}^{(5)}\};\{\mu_I\}) h(m_j^2) \right] \\ &+ a^2 \delta_V' \left[R_{X_V}^{[3,2]}(\{M_{X_V}^{(7)}\};\{\mu_V\}) \tilde{h}(m_{X_V}^2) - \sum_{j \in \{M_V^{(7)}\}} D_{j,X_V}^{[3,2]}(\{M_{X_V}^{(7)}\};\{\mu_V\}) h(m_j^2) \right] \\ &+ (V \to A) \Bigg\}, \end{aligned} \tag{B.4}$$

and sunset diagram

$$\mathcal{Q}_q = \frac{3g_\pi^2}{16\pi^2 f^2}\left\{\frac{1}{16}\sum_{\Xi=I,P,4V,4A,6T} h(m_{qq\Xi}) + \frac{1}{3}\left[R_{X_I}^{[2,2]}(\{M_{X_I}^{(5)}\};\{\mu_I\})\tilde{h}(m_{X_I}^2)\right.\right. \tag{B.5}$$
$$\left.\left. - \sum_{j\in\{M_I^{(5)}\}} D^{[2,2]}(\{M_{X_I}^{(5)}\};\{\mu_I\})h(m_j^2)\right]\right\}.$$

The definitions of the residues, $R^{[i,j]}$ and $D^{[i,j]}$, are

$$\begin{aligned} R_j^{[n,k]}(\{m\};\{\mu\}) &\equiv \frac{\prod_{a=1}^{k}(\mu_a^2 - m_j^2)}{\prod_{i\neq j}(m_i^2 - m_j^2)}, \\ D_{j,l}^{[n,k]}(\{m\};\{\mu\}) &\equiv -\frac{d}{dm_l^2}R_j^{[n,k]}(\{m\};\{\mu\}). \end{aligned} \tag{B.6}$$

and the mass combinations

$$\begin{aligned} \{M_X^{(5)}\} &\equiv \{m_\eta, m_X\}, \\ \{M_X^{[7]}\} &\equiv \{m_\eta, m_{\eta'}, m_X\}, \\ \{\mu\} &\equiv \{m_U, m_S\}. \end{aligned} \tag{B.7}$$

The relations between the mass combinations are

$$\begin{aligned} m_{\pi_V}^2 &= m_{U_V}^2 = m_{D_V}^2, \\ m_{\eta_V}^2 &= \frac{1}{2}\left(m_{U_V}^2 + m_{S_V}^2 + \frac{3}{4}a^2\delta_V' - Z\right), \\ m_{\eta_V'}^2 &= \frac{1}{2}\left(m_{U_V}^2 + m_{S_V}^2 + \frac{3}{4}a^2\delta_V' + Z\right), \\ Z &\equiv \sqrt{(m_{S_V}^2 - m_{U_V}^2)^2 - \frac{a^2\delta_V'}{2}(m_{S_V}^2 - m_{U_V}^2) + \frac{9(a^2\delta_V')^2}{16}}). \end{aligned} \tag{B.8}$$

B_{B_q} has a much simpler chiral expression

$$B_{B_q} = \frac{3}{8}\kappa\left[1 - \mathcal{X}_q\right] \tag{B.9}$$

where

$$\mathcal{X}_q = \frac{(1-3g_\pi^2)}{16\pi^2 f_\pi^2}\left\{\left[\frac{1}{16}\sum_{\Xi=I,P,4V,4A,6T} h(m_{qq\Xi})\right]\right. \tag{B.10}$$
$$\left. + \frac{1}{3}\left[R_{X_I}^{[2,2]}(\{M_{X_I}^{(5)}\};\{\mu_I\})\tilde{h}(m_{X_I}^2) - \sum_{j\in\{M_I^{(5)}\}} D^{[2,2]}(\{M_{X_I}^{(5)}\};\{\mu_I\})h(m_j^2)\right]\right\}.$$

References

[1] M. Alford, W. Dimm, G. P. Lepage, G. Hockney, and P. B. Mackenzie. Lattice qcd on small computers. *Physics Letters B*, 361:87, 1995.

[2] K. Anikeev, D. Atwood, F. Azfar, S. Bailey, C. W. Bauer, W. Bell, G. Bodwin, E. Braaten, G. Burdman, J. N. Butler, K. Byrum, N. Cason, A. Cerri, H. W. K. Cheung, A. Dighe, S. Donati, R. K. Ellis, A. Falk, G. Feild, S. Fleming, I. Furic, S. Gardner, Y. Grossman, G. Gutierrez, W. Hao, B. W. Harris, J. Hewett, G. Hiller, R. Jesik, M. Jones, P. A. Kasper, A. El-Khadra, M. Kirk, V. V. Kiselev, J. Kroll, A. S. Kronfeld, R. Kutschke, V. E. Kuznetsov, E. Laenen, Jungil Lee, A. K. Leibovich, J. D. Lewis, Z. Ligeti, A. K. Likhoded, H. E. Logan, M. Luke, A. Maciel, G. Majumder, P. Maksimovic, M. Martin, S. Menary, P. Nason, U. Nierste, Y. Nir, L. Nogach, E. Norrbin, C. Oleari, V. Papadimitriou, M. Paulini, C. Paus, M. Petteni, R. Poling, M. Procario, G. Punzi, H. Quinn, A. Rakitine, G. Ridolfi, K. Shestermanov, G. Signorelli, J. P. Silva, T. Skwarnicki, A. Smith, B. Speakman, K. Stenson, F. Stichelbaut, S. Stone, K. Sumorok, M. Tanaka, W. Taylor, W. Trischuk, J. Tseng, R. Van Kooten, A. Vasiliev, M. Voloshin, J. C. Wang, A. B. Wicklund, F. Wurthwein, N. Xuan, J. Yarba, K. Yip, and A. Zieminski. B physics at the tevatron: Run ii and beyond, 2002.

[3] JLQCD Collaboration: S. Aoki, M. Fukugita, S. Hashimoto, K.-I. Ishikawa, N. Ishizuka, Y. Iwasaki, K. Kanaya, T. Kaneko, Y. Kuramashi, M. Okawa, T. Onogi, N. Tsutsui, A. Ukawa, N. Yamada, and T. Yoshie. B-bbar mixing in unquenched lattice qcd. *Physical Review Letters*, 91:212001, 2003.

[4] C. Aubin and C. Bernard. Staggered chiral perturbation theory for heavy-light mesons. *Physical Review D*, 73:014515, 2006.

[5] MILC Collaboration: C. Aubin, C. Bernard, C. DeTar, Steven Gottlieb, E. B. Gregory, U. M. Heller, J. E. Hetrick, J. Osborn, R. Sugar, and D. Toussaint. Light pseudoscalar decay constants, quark masses, and low energy constants from three-flavor lattice qcd. *Physical Review D*, 70:114501, 2004.

[6] C. Bernard. Chiral logs in the presence of staggered flavor symmetry breaking. *Physical Review D*, 65:054031, 2002.

[7] Claude Bernard, Tom Burch, Thomas A. DeGrand, Saumen Datta, Carleton DeTar, Steven Gottlieb, Urs M. Heller, Kostas Orginos, Robert Sugar, and Doug Toussaint. The qcd spectrum with three quark flavors. *Physical Review D*, 64:054506, 2001.

[8] S. M. Bilenky. Cp-violation and unitarity triangle test of the standard model, 2007.

[9] UTfit Collaboration: M. Bona, M. Ciuchini, E. Franco, V. Lubicz, G. Martinelli, F. Parodi, M. Pierini, P. Roudeau, C. Schiavi, L. Silvestrini, A. Stocchi, and V. Vagnoni. The unitarity triangle fit in the standard model and hadronic parameters from lattice qcd: A reappraisal after the measurements of delta m_s and br(b to tau nu). *JHEP*, 0610:081, 2006.

[10] Stefano Capitani. Lattice perturbation theory. *Physics Reports*, 382:113, 2003.

[11] CDF Collaboration. Measurement of the bs-bsbar oscillation frequency. *AIP CONF.PROC.*, 870:116, 2006.

[12] William Detmold and C. J. David Lin. Matrix elements of the complete set of delta b = 2 and
delta c = 2 operators in heavy meson chiral perturbation theory, 2006.

[13] Massimo Di Pierro. Fermiqcd: A tool kit for parallel lattice qcd applications. *Nuclear Physics B - Proceedings Supplements*, 106:1034, 2002.

[14] J. F. Donoghue, E. Golowich, and Barry R. Holstein. Dynamics of the standard model. *Camb. Monogr. Part. Phys. Nucl. Phys. Cosmol.*, 2:1–540, 1992.

[15] Aida X. El-Khadra, Andreas S. Kronfeld, and Paul B. Mackenzie. Massive fermions in lattice gauge theory. *Physical Review D*, 55:3933, 1997.

[16] Elvira Gamiz. Private communication.

[17] Elvira Gamiz, Junko Shigemitsu, and Howard Trottier. Four fermion operator matching with nrqcd heavy and asqtad light quarks, 2008.

[18] Alan Gray, Matthew Wingate, Christine T. H. Davies, Emel Gulez, G. Peter Lepage, Quentin Mason, Matthew Nobes, and Junko Shigemitsu. The b meson decay constant from unquenched lattice qcd. *Physical Review Letters*, 95:212001, 2005.

[19] Emel Gulez, Junko Shigemitsu, and Matthew Wingate. One-loop matching of the heavy-light a_0 and v_0 currents with nrqcd heavy and improved naive light quarks. *Physical Review D*, 69:074501, 2004.

[20] Junpei Harada, Shoji Hashimoto, Ken-Ichi Ishikawa, Andreas S. Kronfeld, Tetsuya Onogi, and Norikazu Yamada. Application of heavy-quark effective theory to lattice qcd: Ii. radiative corrections to heavy-light currents. *ERRATUM-IBID.D*, 71:019903, 2005.

[21] S. Hashimoto et al. Renormalization of the Delta(B) = 2 four-quark operators in lattice NRQCD. *Phys. Rev.*, D62:114502, 2000.

[22] John B. Kogut and Leonard Susskind. Hamiltonian Formulation of Wilson's Lattice Gauge Theories. *Phys. Rev.*, D11:395, 1975.

[23] Jack Laiho and Ruth van der Water. Private communication.

[24] G. P. Lepage et al. Constrained curve fitting. *Nucl. Phys. Proc. Suppl.*, 106:12–20, 2002.

[25] G. P. Lepage and P. B. Mackenzie. On the viability of lattice perturbation theory. *Physical Review D*, 48:2250, 1993.

[26] G. P. Lepage, L. Magnea, C. Nakhleh, U. Magnea, and K. Hornbostel. Improved nonrelativistic qcd for heavy quark physics. *Physical Review D*, 46:4052, 1992.

[27] G. Peter Lepage. Flavor-symmetry restoration and symanzik improvement for staggered quarks. *Physical Review D*, 59:074502, 1999.

[28] M. Lüscher and P. Weisz. Computation of the action for on-shell improved lattice gauge theories at weak coupling. *Physics Letters B*, 158:250–254, August 1985.

[29] Aneesh V. Manohar and Mark B. Wise. Heavy quark physics. *Camb. Monogr. Part. Phys. Nucl. Phys. Cosmol.*, 10:1–191, 2000.

[30] Quentin John Mason. High-precision lattice QCD: Perturbations in a non- perturbative world. UMI-31-14569.

[31] Bartholomeus P. G. Mertens, Andreas S. Kronfeld, and Aida X. El-Khadra. The self-energy of massive lattice fermions. *Physical Review D*, 58:034505, 1998.

[32] A. Morel. CHIRAL LOGARITHMS IN QUENCHED QCD. *J. Phys. (France)*, 48:1111–1119, 1987.

[33] Holger Bech Nielsen and M. Ninomiya. Absence of Neutrinos on a Lattice. 1. Proof by Homotopy Theory. *Nucl. Phys.*, B185:20, 1981.

[34] Matthew A. Nobes. Automated lattice perturbation theory for improved quark and gluon actions. UMI-NR-03173.

[35] A. Pich. Effective field theory, 1998.

[36] William H. Press, William T. Vetterling, Saul A. Teukolsky, and Brian P. Flannery. *Numerical Recipes in C++: the art of scientific computing*. 2002.

[37] Stephen R. Sharpe. Applications of chiral perturbation theory to lattice qcd, 2006.

[38] B. Sheikholeslami and R. Wohlert. Improved continuum limit lattice action for QCD with wilson fermions. *Nuclear Physics B*, 259:572–596, September 1985.

[39] Jim Simone and Claude Bernard. Private communication.

[40] K. Symanzik. Continuum limit and improved action in lattice theories . (II). O(N) non-linear sigma model in perturbation theory. *Nuclear Physics B*, 226:205–227, September 1983.

[41] Kenneth G. Wilson. Confinement of quarks. *Phys. Rev. D*, 10(8):2445–2459, Oct 1974.

[42] Matthew Wingate, Junko Shigemitsu, Christine T. H. Davies, G. Peter Lepage, and Howard D. Trottier. Heavy-light mesons with staggered light quarks. *Physical Review D*, 67:054505, 2003.

[43] W.-M. Yao, C. Amsler, D. Asner, R.M. Barnett, J. Beringer, P.R. Burchat, C.D. Carone, C. Caso, O. Dahl, G. D'Ambrosio, A. DeGouvea, M. Doser, S. Eidelman, J.L. Feng, T. Gherghetta, M. Goodman, C. Grab, D.E. Groom, A. Gurtu, K. Hagiwara, K.G. Hayes, J.J. Hernández-Rey, K. Hikasa, H. Jawahery, C. Kolda, Kwon Y., M.L. Mangano, A.V. Manohar, A. Masoni, R. Miquel, K. Mönig, H. Murayama, K. Nakamura, S. Navas, K.A. Olive, L. Pape, C. Patrignani, A. Piepke, G. Punzi, G. Raffelt, J.G. Smith, M. Tanabashi, J. Terning, N.A. Törnqvist, T.G. Trippe, P. Vogel, T. Watari, C.G. Wohl, R.L. Workman, P.A. Zyla, B. Armstrong, G. Harper, V.S. Lugovsky, P. Schaffner, M. Artuso, K.S. Babu, H.R. Band, E. Barberio, M. Battaglia, H. Bichsel, O. Biebel, P. Bloch, E. Blucher, R.N. Cahn, D. Casper, A. Cattai, A. Ceccucci, D. Chakraborty, R.S. Chivukula, G. Cowan, T. Damour, T. DeGrand, K. Desler, M.A. Dobbs, M. Drees, A. Edwards, D.A. Edwards, V.D. Elvira, J. Erler, V.V. Ezhela, W. Fetscher, B.D. Fields, B. Foster, D. Froidevaux, T.K. Gaisser, L. Garren, H.-J. Gerber, G. Gerbier, L. Gibbons, F.J. Gilman, G.F. Giudice, A.V. Gritsan, M. Grünewald, H.E. Haber, C. Hagmann, I. Hinchliffe, A. Höcker, P. Igo-Kemenes, J.D. Jackson, K.F. Johnson, D. Karlen, B. Kayser, D. Kirkby, S.R. Klein, K. Kleinknecht, I.G. Knowles, R.V. Kowalewski, P. Kreitz, B. Krusche, Yu.V. Kuyanov, O. Lahav, P. Langacker, A. Liddle, Z. Ligeti, T.M. Liss, L. Littenberg, L. Liu, K.S. Lugovsky, S.B. Lugovsky, T. Mannel, D.M. Manley, W.J. Marciano, A.D. Martin, D. Milstead, M. Narain, P. Nason, Y. Nir, J.A. Peacock, S.A. Prell, A. Quadt, S. Raby, B.N. Ratcliff, E.A. Razuvaev, B. Renk, P. Richardson, S. Roesler, G. Rolandi, M.T. Ronan, L.J. Rosenberg, C.T. Sachrajda, S. Sarkar, M. Schmitt, O. Schneider, D. Scott, T. Sjöstrand, G.F. Smoot, P. Sokolsky, S. Spanier, H. Spieler, A. Stahl, T. Stanev, R.E. Streitmatter, T. Sumiyoshi, N.P. Tkachenko, G.H. Trilling, G. Valencia, K. van Bibber, M.G. Vincter, D.R. Ward, B.R. Webber, J.D. Wells, M. Whalley, L. Wolfenstein, J. Womersley, C.L. Woody, A. Yamamoto, O.V. Zenin, J. Zhang, and R.-Y. Zhu. Review of Particle Physics. *Journal of Physics G*, 33:1+, 2006.

Author's Biography

Richard Evans was born on December 19th, 1979 in York, PA. He attended high school at Hershey High School and in 1998 enrolled in Johns Hopkins University. There he pursued a variety of majors but chose to obtain a B.A. in Physics. He graduated college in 2002 and in the summer of 2002 worked at Johnson Space Center in Houston on a Presidential Early Career Scholarship. There he performed statistical analysis on an experimental high frequency sensitive ECG. In the fall of 2002 he began graduate school at University of Illinois in the Department of Physics, where he completed his M.S. in physics in 2004. He then began studying Lattice QCD. After he completes his Ph.D. Richard Evans will begin work as a post doctoral researcher at the University of Regensburg.